HYBRID CONTROL

FOR AEROSPACE SYSTEMS

Mirko Brentari

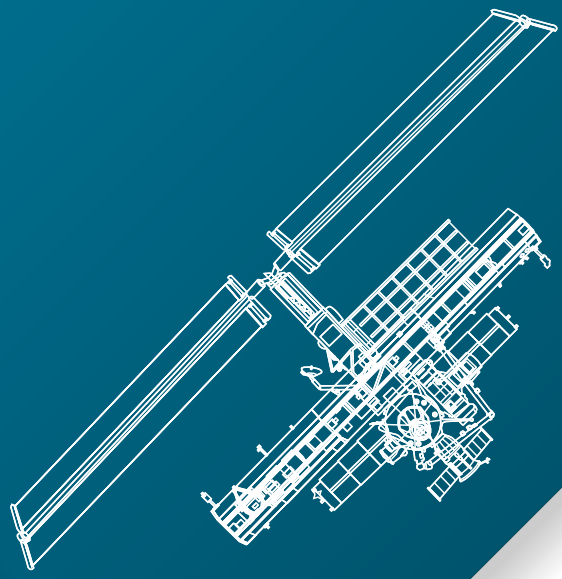

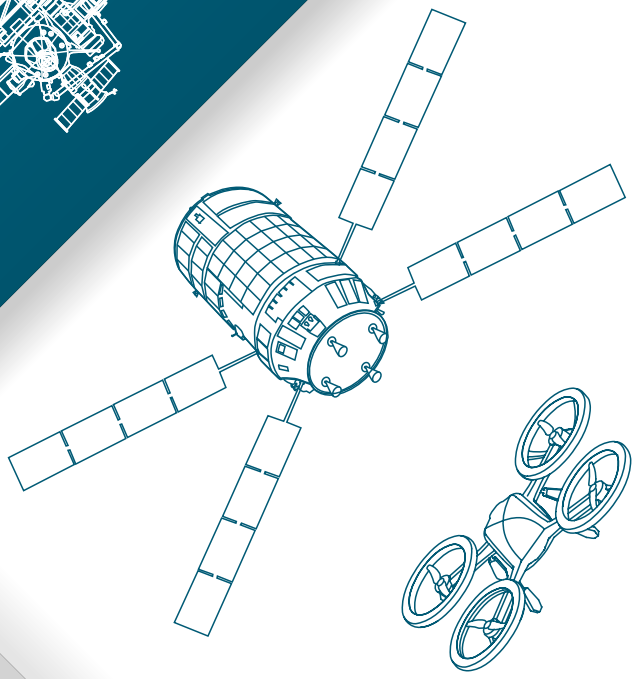

UNIVERSITY
OF TRENTO - Italy

DEPARTMENT OF INDUSTRIAL ENGINEERING

Doctoral School in Materials, Mechatronics and Systems Engineering

University of Trento – Department of Industrial Engineering
Mirko Brentari: *Hybrid control for aerospace systems*, 2018

HYBRID CONTROL FOR AEROSPACE SYSTEMS

MIRKO BRENTARI

University of Trento
Department of Industrial Engineering
March 2019

Approved by

Luca Zaccarian, `Supervisor 1`
Department of Industrial Engineering & Laboratoire d'analyse et d'architecture des systèmes
University of Trento, Italy & Centre National de la Recherche Scientifique, France

Paolo Bosetti, `Supervisor 2`
Department of Industrial Engineering
University of Trento, Italy

Referees

Sophie Tarbouriech
Laboratoire d'analyse et d'architecture des systèmes
Centre National de la Recherche Scientifique, France

Giulia Giordano
Delft Center for Systems and Control
Delft University of Technology, The Netherlands

ABSTRACT

Hybrid dynamical systems are dynamical systems in which continuous and discrete evolutions coexist and interact. Their twofold nature makes them particularly powerful for both describing and synthesizing complex dynamical behaviors. In this work we exploit this capability for designing innovative control and estimation algorithms that cope with challenges in aerospace applications. In particular, *(i)* we propose different impulsive control strategies for the problem of close-range rendezvous between two spacecrafts in elliptic orbits; *(ii)* we design a robust time-sub-optimal controller for a class of linear systems emerging in aerospace applications where the control input is limited in magnitude; *(iii)* we synthesize an observer to estimate the speed of rotary systems providing angular measurements that evolve on the unit circle. To this end, we make use of a recent formalism tailored to hybrid dynamical systems for both modeling and proving desirable properties of the proposed algorithms, which are as well confirmed by simulative and experimental validations.

SOMMARIO

I sistemi dinamici ibridi sono sistemi dinamici nei quali evoluzioni a tempo continuo ed a tempo discreto coesistono ed interagiscono. La loro duplice natura li rende uno strumento particolarmente potente sia per descrivere sia per progettare comportamenti dinamici complessi. In questo lavoro si sfrutta questa loro potenzialità per progettare algoritmi di controllo e stima per affrontare problemi che emergono in applicazioni aerospaziali. Nello specifico, *(i)* si propongono diverse strategie di controllo impulsivo per il problema del *close-range* rendezvous tra due veicoli spaziali in orbita ellittica; *(ii)* si progetta un controllore robusto a tempo quasi minimo per una famiglia di sistemi lineari con ingresso limitato in ampiezza che emergono in applicazioni aerospaziali; *(iii)* si sintetizza un osservatore per la stima della velocità di un sistema rotante che fornisce misure angolari che evolvono sul cerchio unitario. A questo scopo, si fa uso di un recente formalismo ibrido sia per modellare sia per dimostrare proprietà desiderabili degli algoritmi proposti, le quali sono anche validate tramite strumenti simulativi e sperimentali.

CONTENTS

LIST OF FIGURES

LIST OF TABLES

1 INTRODUCTION

1.1 GENERAL INTRODUCTION

Recently, hybrid dynamical systems have gained increasing interest and popularity in the control community due to their ability to cover with a single mathematical tool both continuous and discrete dynamics, which can be intertwined. The coexistence of both continuous and discrete dynamics in a comprehensive modeling and synthesis framework allows to design with ease complex dynamical behaviors, such as hysteresis mechanisms, impulsive controls, non-smooth dynamics, linear temporal logic, hybrid automata, et cetera. The availability of such a tool has indeed unlocked the possibility of designing innovative solutions with enhanced performance for longstanding problems in control practice. Among the many engineering and technological fields in which hybrid dynamical systems have brought about innovative solutions, control of aerospace systems is one of the areas that have benefited the most from them. As a first example, consider the problem of controlling the attitude of a satellite in the earth orbit and servicing, e.g., for telecommunication, science, defense, or weather forecasting. This problem corresponds to controlling the attitude of a rigid body in the 3D rotation group called $SO(3)$. It is well known that there does not exist a continuous state-feedback algorithm able to globally stabilizing any equilibrium point in $SO(3)$ [15] due to topological obstructions. This topic has been the subject of many studies, and represents a challenge both from the viewpoint of modeling ($SO(3)$ parametrization) and control (e.g., the "unwinding phenomenon" [15, Sec. 3]). A recent remarkable work [71] proposed a hybrid controller capable of overcoming this structural limit, introducing a feedback algorithm capable of globally stabilize any equilibrium point of $SO(3)$ by exploiting the twofold nature of hybrid dynamical systems at the small cost of introducing a hysteresis band around the desired attitude. Other examples are the novel trends in spacecraft applications benefiting from hybrid systems approaches. For instance, the invited session "A Spacecraft Benchmark Problem for Analysis & Control of Hybrid Systems" at the 2016 IEEE Conference on Decision and Control considered the application of hybrid tools to rendezvous, docking, and estimation problems, see for example [53], [69], and [62]. Regarding estimation algorithms, the community proposed in the last years hybrid solutions to enhance the performance of classical estimation schemes, consider for example [8] and [32]. More specifically for aerospace, estimation on the 3D rotation space $SO(3)$ has particularly benefited from hybrid systems [13] [14]. As for vertical-take-off-and-landing unmanned-aerial-vehicles, hybrid systems led to developing interesting algorithms for trajectory tracking, for example [73]. Many of the above cited studies make use of the modern and exhaustive hybrid dynamical system framework presented in [45].

In that valuable work, Rafal Goebel, Ricardo G. Sanfelice, and Andrew R. Teel introduce a new formalism for hybrid systems, together with a set of analysis tools for establishing different versions of stability properties with an intrinsic degree of robustness in-the-small.

This thesis adopts this formalism as well, and fits within the above described recent trend, facing control engineering problems in aerospace applications where the hybrid formalism [45] can indeed provide significant advantages.

In the first part of this manuscript, we focus on the problem of satellite rendezvous between two spacecraft in elliptic orbits. Using a linearized model of the relative dynamics, we first propose a periodic similarity transformation based on Floquet-Lyapunov theory [18, Sec. 1.2], leading to a set of coordinates under which the free motion is linear time-invariant. Then the impulsive control of satellite rendezvous corresponds naturally to the discrete-time part of a hybrid dynamical system, and we show that the arising elegant representation enables designing hybrid impulsive control laws with different trade-offs between computational complexity and fuel consumption. The hybrid formalism allows us to prove suitable stability properties induced by the proposed controllers as well.

The second part addresses the stabilization of a class of linear systems in the presence of input saturation, which is intrinsic in every control problem involving electromechanical actuators. The considered class of linear systems shares the common feature to be polynomially unstable, which represents a frequent situation in aerospace applications, and take into account dynamical processes with up to three poles at the origin. From the late 60's with the work of Fuller [42], it is well known that no saturated linear controller is able to globally stabilize a system with 3 poles at the origin, leaving the door open for modern approaches to solve this problem, see for example [99]. We cope with this problem exploiting hybrid dynamical systems to design a discontinuous hysteretic feedback, which adopts a robust time-optimal like solution.

The third part of this manuscript focuses on the synthesis of a hybrid velocity estimation algorithm for rotational systems when only noisy position measurements evolving on the unit circle $\mathbb{S}_1$ are available. There exist many sensors that supply angular measurements evolving in $\mathbb{S}_1$, such as rotary displacement potentiometer sensors, rotary displacement capacitive sensors, and Hall-effect based encoders. The considered problem is relevant when estimating the rotational velocity of a propeller in the case of a propeller-actuated experimental setup. The peculiarity of measurements evolving in $\mathbb{S}_1$ is that they exhibit unpredictable jumps, since the angular parametrization of $\mathbb{S}_1$ evolves in a compact set $[-\pi\ \pi]$. One more time we exploit the hybrid dynamical systems formalism for coping with discontinuous behaviors.

More specific introductions to the considered problem will be given at the beginning of each of the three parts of this manuscript.

The three parts composing this work are organized as follows. The first part consists of two chapters. In Chapter 2 we specifically introduce and illustrate the derivation of a convenient model for the problem of close-range rendezvous between two spacecraft in elliptic orbits, while Chapter 3 focuses on the controller design. The second part contains three chapters. In Chapter 4 we

introduce the problem of controlling a class of saturated linear system and we design an innovative robust time sub-optimal (RTSO) controller. In Chapter 5 we derive an accurate Benchmark model of the Quanser's 3 DOF Helicopter, which is used in Chapter 6 as validation tool of the RTSO controller in a real-world application together with another experimental setup. Finally, the third part of this manuscript is dedicated to the design of the above mentioned estimation algorithm for rotational processes evolving on the unit circle.

1.2 SCIENTIFIC PRODUCTION

The research activity carried out as a Ph.D. candidate has resulted in the following publications, based on which this thesis is built:

IN PREPARATION OR UNDER REVIEW

[22] M. Brentari, P. Bosetti, I. Queinnec, and L. Zaccarian. "Benchmark model of Quanser's 3 DOF Helicopter." Under review in the IEEE/ASME Transactions on Mechatronics. 2018. URL: https://hal.laas.fr/hal-01711135

JOURNAL

[24] M. Brentari, S. Urbina, D. Arzelier, C. Louembet, and L. Zaccarian. "A hybrid control framework for impulsive control of satellite rendezvous." In: *IEEE Transactions on Control Systems Technology* 99 (2018), pp. 1–15

[23] M. Brentari, P. Bosetti, and L. Zaccarian. "A class of hybrid velocity observers for angular measurements with jumps." In: *IEEE Control Systems Letters* 2.4 (2018), pp. 617–622

PEER-REVIEWED CONFERENCE

[20] M. Brentari, D. Arzelier, C. Louembet, L.S. Urbina, and L. Zaccarian. "A hybrid control framework for impulsive control of satellite rendezvous." In: *American Control Conference (ACC)*. Boston (MA), USA, 2016

[21] M. Brentari, P. Bosetti, R. Goebel, and L. Zaccarian. "Robust time-sub-optimal control of the saturated double integrator applied to attitude stabilization." In: *IEEE Conference on Decision and Control (CDC)*. Melbourne (Australia), 2017, pp. 5487–5492

The material of the above publications is included in the three parts of this thesis, together with some original unpublished work, as follows

PART I : [24], [20]
PART II : [21], [22]
PART III : [23]

1.3 NOTATION

In this dissertation, the following notation will be used.

- For $x_1 \in \mathbb{R}^{\alpha_1}, \ldots, x_n \in \mathbb{R}^{\alpha_n}$, we represent with $(x_1, \ldots, x_n)$ the column-stacking operation $[x_1^\top, \ldots, x_n^\top]^\top$.
- With $\mathbb{B}_r(a)$ we refer to the n-dimensional closed ball of radius r centered at a, that is $\mathbb{B}_r(a) := \{x \in \mathbb{R}^n \mid |x - a| \leq r\}$.
- I_n is the identity matrix of dimension n. When the subscript n is omitted, an identity matrix with a suitable dimension is considered.
- $\overline{\mathcal{S}}$ denotes the closure of a set $\mathcal{S}$.

1.4 A BRIEF INTRODUCTION TO THE HYBRID DYNAMICAL SYSTEMS FRAMEWORK

In this section, the reader will be briefly introduced to the hybrid dynamical systems framework [45], which is the main tool used in this manuscript to cope with hybrid dynamics. We report here a brief introduction on the modeling and analysis tools that will be used along the manuscript, based on an extract of [44, 45, 94].

The general model of a hybrid dynamical system can be represented as

$$\mathcal{H} : \begin{cases} \dot{x} \in F(x) , & x \in \mathcal{C} \\ x^+ \in G(x) , & x \in \mathcal{D} , \end{cases} \tag{1.1}$$

in which we refer to

- the set $\mathcal{C} \subset \mathbb{R}^n$ as "the flow set",
- the set-valued mapping [1] $F : \mathbb{R}^n \rightrightarrows \mathbb{R}^n$ as "the flow map",
- the set $\mathcal{D} \subset \mathbb{R}^n$ as "the jump set",
- the set-valued mapping $G : \mathbb{R}^n \rightrightarrows \mathbb{R}^n$ as "the jump map".

In $\mathcal{H}$, $\dot{x}$ indicates the continuous-time derivative of the state x, while x^+ indicates the value of x after a discrete time update. The collection of the elements $\mathcal{C}$, F, $\mathcal{D}$, and G is called the data of hybrid system $\mathcal{H}$. For the sake of conciseness, we will refer to these data of the hybrid system $\mathcal{H}$ as $\mathcal{H} = (\mathcal{C}, F, \mathcal{D}, G)$. A simpler and less general version of system $\mathcal{H}$ in (1.1) is obtained by replacing the set-valued mappings F and G with standard differential and difference equations involving functions $f : \mathbb{R}^n \to \mathbb{R}^n$ and $g : \mathbb{R}^n \to \mathbb{R}^n$:

$$\mathcal{H} : \begin{cases} \dot{x} = f(x) , & x \in \mathcal{C} \\ x^+ = g(x) , & x \in \mathcal{D} \end{cases} \tag{1.2}$$

A pictorial representation of hybrid system $\mathcal{H}$ in equation (1.2) is given in Figure 1.1. Intuitively, the state $x \in \mathbb{R}^n$ of hybrid system $\mathcal{H}$ can evolve continuously, i.e., it can "flow", according to the differential inclusion $\dot{x} \in F(x)$ or the differential equation $\dot{x} = f(x)$ when $x \in \mathcal{C}$; it can also evolve discretely, i.e., it can "jump", according to the difference inclusion $x^+ \in G(x)$ or the difference equation $x^+ = g(x)$ when $x \in \mathcal{D}$. It intuitively follows that state x can evolve in many different ways according to hybrid system $\mathcal{H}$. The possibility of having multiple solutions is due to the presence of set-valued mappings in (1.1) and to the fact that the intersection between the flow set and the jump set $\mathcal{C} \cap \mathcal{D}$ can be non empty, and in this intersection there is no prescribed evolution, but both flowing and jumping are possible.

When working with hybrid dynamical systems of the presented framework, it is typical to ask for some regularity conditions of the hybrid data $(\mathcal{C}, F, \mathcal{D}, G)$ in order to guarantee the well-posedness of the system. These conditions are denoted as "hybrid basic conditions" or "hybrid basic assumptions". We need to introduce as well the concept of domain of a set-valued mapping as follow.

1 For a definition of set-valued mapping the reader can refer to [45, Sec. 2.1].

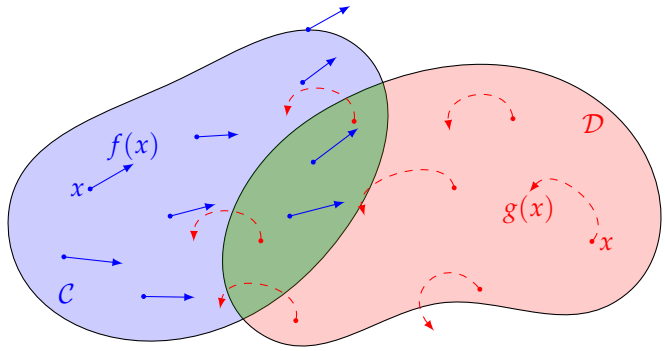

Figure 1.1: Data appearing in hybrid system $\mathcal{H}$ in equation (1.2). The flow set $\mathcal{C}$ is depicted in light blue, while the jump set $\mathcal{D}$ is in light red. For some x's, the flow map is represented by blue arrows, while the jump map corresponds to dashed red arcs.

Definition 1.1 (Domain of a set-valued mapping [45, Def. 2.1])**.** *Given a set-valued mapping $M : \mathbb{R}^m \rightrightarrows \mathbb{R}^n$, the domain of M is the set*

$$\operatorname{dom} M = \{x \in \mathbb{R}^m \mid M(x) \neq \emptyset\} \tag{1.3}$$

Assumption 1.1 (Hybrid basic conditions [45, Ass. 6.5])**.** *With "hybrid basic conditions" we refer to the three following requirements on the data $(\mathcal{C}, F, \mathcal{D}, G)$ of $\mathcal{H}$ in (1.1):*

1. *$\mathcal{C}$ and $\mathcal{D}$ are closed subsets of $\mathbb{R}^n$;*
2. *$F\colon \mathbb{R}^n \rightrightarrows \mathbb{R}^n$ is outer semicontinuous and locally bounded [2] relative to $\mathcal{C}$, $\mathcal{C} \subset \operatorname{dom} F$, and $F(x)$ is convex for every $x \in \mathcal{C}$;*
3. *$G\colon \mathbb{R}^n \rightrightarrows \mathbb{R}^n$ is outer semicontinuous and locally bounded relative to $\mathcal{D}$, $\mathcal{D} \subset \operatorname{dom} G$.*

Outer semicontinuity in the above assumption is equivalent to the following property.

Lemma 1.1 (Outer semicontinuity and closed graph [45, Lem. 5.10])**.** *A set-valued mapping $M\colon \mathbb{R}^n \rightrightarrows \mathbb{R}^n$ is outer semicontinuous if and only if its graph $\operatorname{gph} M := \{(x, y) \in \mathbb{R}^n \times \mathbb{R}^n | y \in M(x)\}$ is closed. More generally, given a set $\mathcal{S} \subset \mathbb{R}^m$, a set valued mapping $M\colon \mathbb{R}^n \rightrightarrows \mathbb{R}^n$ is outer semicontinuous relative to $\mathcal{S}$ if and only if the set $\{(x, y) \in \mathbb{R}^n \times \mathbb{R}^n | x \in \mathcal{S}, y \in M(x)\}$ is closed.*

In the following chapters, all the data of all the designed hybrid systems satisfy these hybrid basic conditions. These conditions do not represent the minimum necessary requirements for obtaining a reasonably good behavior of a hybrid dynamical system (see for a reference the "nominal well-posedness"

2 Local boundedness of F implies that the image of any bounded set is itself bounded.

and "well-posedness" in [45, Chap. 6]), but, differently from less restrictive properties, they have the advantage to be easy enough to be checked, therefore representing a good modeling principle with which it is reasonable to comply.

A first context where the hybrid basic conditions are useful is the definition of solutions given below, which is simpler than the one in [45, Chap. 2] although equivalent under these conditions. Before defining the concept of solution of a hybrid system, it is fundamental to introduce the concept of "hybrid time domain". Given the twofold nature of a hybrid system, the classical notion of time needs to be extended, because, neither the concept of continuous time $t \in \mathbb{R}_{\geq 0}$ nor the one of discrete time $j \in \mathbb{Z}_{\geq 0}$ can suitably parametrize the solution of a hybrid system. We therefore report here the definition of "hybrid time domain" given in [45].

Definition 1.2 (Hybrid time domain [45, Def. 2.3])**.** *A subset E of $\mathbb{R}_{\geq 0} \times \mathbb{Z}_{\geq 0}$ is a compact hybrid time domain if*

$$E = \bigcup_{j=0}^{J-1} [t_j, t_{j+1}] \times \{j\} \tag{1.4}$$

for some finite sequence of times $0 = t_0 \leq t_1 \leq \cdots \leq t_J$. E is a hybrid time domain if for all $(T, J) \in E$, $E \cap ([0, T] \times \{0, 1, \ldots, J\})$ is a compact hybrid time domain.

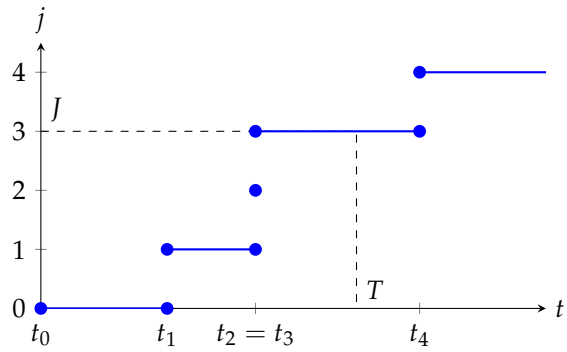

Figure 1.2: A hybrid time domain E.

Figure 1.2 gives a graphical representation of a hybrid time domain. Moreover, we can define the operations $\sup_t$ and $\sup_j$ on a hybrid time domain E as:

$$\sup_t E := \sup\{t \in \mathbb{R}_{\geq 0} \,|\, \exists\, j \in \mathbb{Z}_{\geq 0} \text{ such that } (t, j) \in E\}\,, \tag{1.5a}$$

$$\sup_j E := \sup\{j \in \mathbb{Z}_{\geq 0} \,|\, \exists\, t \in \mathbb{R}_{\geq 0} \text{ such that } (t, j) \in E\}\,, \tag{1.5b}$$

which return, respectively, the supremum value of the continuous time t and the discrete time j on the hybrid time domain E.

We now introduce the concept of solution of a hybrid system based on the concept of hybrid time domain given in Definition 1.2. To this end, we introduce the concept of "hybrid arc", i.e., of a candidate solution.

Definition 1.3 (Hybrid arc [45, Def. 2.4] and domain). *A function $\phi : E \to \mathbb{R}^n$ is a hybrid arc if E is a hybrid time domain and if for each $j \in \mathbb{Z}_{\geq 0}$, the function $t \mapsto \phi(t, j)$ is locally absolutely continuous on the nonempty interval $I^j = \{t : (t, j) \in E\}$. Moreover, the hybrid time domain of a hybrid arc is denoted by* $\operatorname{dom} \phi$.

We can now define what a solution to the hybrid dynamical system (1.1) is. As mentioned before, the following definition simplifies [45, Def. 2.6] by exploiting the fact that we assume the hybrid basic conditions.

Definition 1.4 (Solution to a hybrid system under the hybrid basic conditions [45, Sec. 6.2.1]). *A hybrid arc ϕ is a solution to the hybrid dynamical system $\mathcal{H} = (\mathcal{C}, F, \mathcal{D}, G)$ in (1.1) satisfying the hybrid basic conditions if*

1. $\phi(0, 0) \in \mathcal{C} \cup \mathcal{D}$;
2. *for all $j \in \mathbb{Z}_{\geq 0}$ such that $I^j := \{t : (t, j) \in \operatorname{dom} \phi\}$ has a nonempty interior,*

$$\phi(t, j) \in \mathcal{C} \text{ , for almost all } t \in I^j, \tag{1.6a}$$

$$\dot{\phi}(t, j) \in F(\phi(t, j)) \text{ , for almost all } t \in I^j ; \tag{1.6b}$$

3. *for all $(t, j) \in \operatorname{dom} \phi$ such that $(t, j + 1) \in \operatorname{dom} \phi$,*

$$\phi(t, j) \in \mathcal{D} , \tag{1.6c}$$

$$\phi(t, j + 1) \in G(\phi(t, j)). \tag{1.6d}$$

From this definition it follows that, when $\phi(t, j) \in \mathcal{C} \cap \mathcal{D}$, the solution $\phi(t, j)$ is forced neither to flow nor to jump. The definition asks that if the solution flows, it does it according to the flow map as in (1.6b), and if it jumps, it does it according to the jump map as in (1.6d).

There exist solutions with different peculiarities, but some of them are of particular importance and deserve to be defined precisely as follows.

Definition 1.5 (Types of solutions [45, Def. 2.5, Def. 2.7]). *A solution ϕ to a hybrid system $\mathcal{H} = (\mathcal{C}, F, \mathcal{D}, G)$ is*

- *nontrivial if* $\operatorname{dom} \phi$ *contains at least two points;*
- *complete if* $\operatorname{dom} \phi$ *is unbounded, that is,* $\sup_t \operatorname{dom} \phi + \sup_j \operatorname{dom} \phi = +\infty$*;*
- *Zeno if it is complete and* $\sup_t \operatorname{dom} \phi < +\infty$
- *maximal if there does not exist another solution ψ to $\mathcal{H}$ such that* $\operatorname{dom} \phi$ *is a proper subset of* $\operatorname{dom} \psi$ *and $\phi(t, j) = \psi(t, j)$ for all $(t, j) \in \operatorname{dom} \phi$.*

We introduce now briefly some concepts about the stability of hybrid systems that will be used later in the manuscript. When working with hybrid dynamical systems, one is often interested in studying the stability properties of a set rather than a single equilibrium point, as motivated in [44, p. 58]. This is true as well in what we develop in the subsequent chapters. In order to properly analyze the behavior of solutions with respect to sets, we define the concept of distance to a closed set.

Definition 1.6 (Distance to a closed set [45, Def. 3.5])**.** *Given a vector $x \in \mathbb{R}^n$ and a closed set $\mathcal{A} \subset \mathbb{R}^n$, the distance of x to $\mathcal{A}$ is defined as*

$$|x|_{\mathcal{A}} := \inf_{y \in \mathcal{A}} |x - y|. \tag{1.7}$$

In the case of compact sets, as the ones considered in the following, the inf in (1.7) can be replaced by the min.

We can then introduce the concept of asymptotic stability of a compact set for a hybrid dynamical system.

Definition 1.7 (Asymptotic stability of a compact set [44, p. 49])**.** *For $\mathcal{H} = (\mathcal{C}, F, \mathcal{D}, G)$ in (1.1), a compact set $\mathcal{A} \subset \mathbb{R}^n$ is*

STABLE *if for each scalar $\epsilon > 0$ there exists a scalar $\delta > 0$ such that $|\phi(0,0)|_{\mathcal{A}} \leq \delta$ implies $|\phi(t,j)|_{\mathcal{A}} \leq \epsilon$ for all solutions ϕ to $\mathcal{H}$ and all $(t,j) \in \operatorname{dom}\phi$,*

ATTRACTIVE *if there exists a neighborhood of $\mathcal{A}$ from which each solution ϕ to $\mathcal{H}$ is bounded and complete solutions converge to $\mathcal{A}$, that is, $|\phi(t,j)|_{\mathcal{A}} \to 0$ as $t + j \to \infty$ with $(t,j) \in \operatorname{dom}\phi$,*

ASYMPTOTICALLY STABLE *if it is stable and attractive,*

GLOBALLY ASYMPTOTICALLY STABLE *if it is stable, attractive, and the largest neighborhood of $\mathcal{A}$ for which $\mathcal{A}$ is attractive can be taken as $\mathbb{R}^n$.*

Establishing if a compact set is (globally) asymptotically stable for a hybrid system $\mathcal{H}$ is not a trivial task. In order to give formal stability certificates in this manuscript we follow an indirect approach based on Lyapunov methods which allow establishing stability properties without computing solutions. Standard Lyapunov tools in the hybrid context [45, Sec. 3.2, Thm. 3.18, Def. 7.29] require to find a candidate Lyapunov function that is continuously differentiable in a neighborhood of the flow set $\mathcal{C}$, and which is bounded by a pair of class-$\mathcal{K}_\infty$ functions of the distance to the attractor (i.e., continuous functions that are zero at zero, strictly increasing and unbounded). Moreover, in order to establish global asymptotic stability of a closed set, classical Lyapunov tools require the candidate Lyapunov function to strictly decrease along solutions both while flowing and while jumping. Although all these conditions play a role in order to establish global asymptotic stability, finding a function that fulfills all these conditions is usually challenging. Relaxed versions of classical Lyapunov theorems have been therefore developed, which have the advantage to impose milder conditions, therefore easier to be satisfied. We report here the result presented in [94], which relaxes the requirement of strict decrease along solutions with a non-increase requirement by imposing instead an invariance type of argument, and take into consideration non-smooth Lyapunov functions.

Definition 1.8 (Non-smooth Lyapunov function candidate)**.** *A function $V : \operatorname{dom} V \to \mathbb{R}$ is said to be a non-smooth Lyapunov function candidate for a hybrid system $\mathcal{H} = (\mathcal{C}, F, \mathcal{D}, G)$ if*

1. *$(\mathcal{C} \cup \mathcal{D}) \subset \operatorname{dom} V$ and V is continuous in $\mathcal{C} \cup \mathcal{D}$ and locally Lipschitz [3] in a neighborhood of $\mathcal{C}$,*

3 According to [30], a function is said to be locally Lipschitz near a point if there exists a neighborhood of that point where the function is Lipschitz.

2. *V is positive definite with respect to $\mathcal{A}$ in $\mathcal{C} \cup \mathcal{D}$ (i.e., $V(x) = 0$ for all $x \in \mathcal{A}$ and $V(x) > 0$ for all $x \in (\mathcal{C} \cup \mathcal{D}) \setminus \mathcal{A}$), and radially unbounded relative to $\mathcal{C} \cup \mathcal{D}$ (i.e., $V(x) \to \infty$ as $|x|_{\mathcal{A}} \to \infty$ for all $x \in \mathcal{C} \cup \mathcal{D}$).*

Obviously, if V is continuously differentiable in a neighborhood of $\mathcal{C}$, it is still a non-smooth Lyapunov function candidate.

Theorem 1.1 (A relaxed non-smooth Lyapunov-like theorem [94, Thm. 1])**.** *Consider a compact set $\mathcal{A}$ and a hybrid system $\mathcal{H} = (\mathcal{C}, F, \mathcal{D}, G)$ satisfying Assumption 1.1 and $G(\mathcal{A} \cap \mathcal{D}) \subset \mathcal{A}$. Assume that there exists a non-smooth Lyapunov function candidate V such that*

$$\dot{V}(x) := \max_{v \in \partial V(x),\, f \in F(x)} \langle v, f \rangle \leq 0, \quad \forall\, x \in \mathcal{C} \setminus \mathcal{A} \tag{1.8a}$$

$$\Delta V(x) := \max_{g \in G(x) \cap (\mathcal{C} \cup \mathcal{D})} V(g) - V(x) \leq 0, \quad \forall\, x \in \mathcal{D} \setminus \mathcal{A} \tag{1.8b}$$

where $\partial V(x)$ is the Clarke generalized gradient of V at x (also called Clarke subdifferential, as defined in [30, Sec. 2.1]). Assume also that no complete solution keeps V constant and nonzero, namely no complete solution ϕ exists satisfying $V(\phi(t, j)) = V(\phi(0, 0)) \neq 0$, for all $(t, j) \in \operatorname{dom} \phi$. Then set $\mathcal{A}$ is globally asymptotically stable (GAS) for $\mathcal{H}$.

This theorem represents a powerful tool for proving GAS of a compact set $\mathcal{A}$ for a hybrid system $\mathcal{H}$ satisfying the hybrid basic conditions. If the Lyapunov function candidate V is continuously differentiable in a neighborhood of $\mathcal{C}$, we can simplify Theorem 1.1 in the following corollary.

Corollary 1.1 (A relaxed smooth Lyapunov-like theorem)**.** *Consider a compact set $\mathcal{A}$ and a hybrid system $\mathcal{H} = (\mathcal{C}, F, \mathcal{D}, G)$ satisfying Assumption 1.1 and $G(\mathcal{A} \cap \mathcal{D}) \subset \mathcal{A}$. Assume that there exists a non-smooth Lyapunov function candidate V that is additionally continuously differentiable in a neighborhood of $\mathcal{C}$, such that*

$$\dot{V}(x) := \max_{f \in F(x)} \langle \nabla V(x), f \rangle \leq 0, \quad \forall\, x \in \mathcal{C} \setminus \mathcal{A} \tag{1.9a}$$

$$\Delta V(x) := \max_{g \in G(x) \cap (\mathcal{C} \cup \mathcal{D})} V(g) - V(x) \leq 0, \quad \forall\, x \in \mathcal{D} \setminus \mathcal{A} \tag{1.9b}$$

where $\nabla V(x)$ is the gradient of V at x. Assume also that no complete solution keeps V constant and nonzero, namely no complete solution ϕ exists satisfying $V(\phi(t, j)) = V(\phi(0, 0)) \neq 0$, for all $(t, j) \in \operatorname{dom} \phi$. Then set $\mathcal{A}$ is globally asymptotically stable (GAS) for $\mathcal{H}$.

Theorem 1.1 and its smooth version in Corollary 1.1 are the tools that will be used the most in the following chapters for giving formal certificates of global asymptotic stability of compact attractors.

We conclude here the brief introduction to the hybrid dynamical system framework of [45]. The reader is referred to [44, 45] for a description of more advanced concepts that have been omitted here for the sake of conciseness and because their are not used in this thesis.

Other

Part I

SATELLITE RENDEZVOUS

2 INTRODUCING AND MODELING THE CLOSE RANGE RENDEZVOUS

In this chapter we first introduce the problem of the rendezvous between spacecraft in elliptic orbits for then illustrating the derivation of a convenient representation of the relative dynamics between the follower spacecraft F and the leader spacecraft L in the phase of proximity operations. The proposed model has deep roots in the existing literature, making use of the well known Tschauner-Hempel (TH) equations [101] and the Yamanaka-Ankersen solution [104], but it also introduces a novel change of coordinate to simplify the relative dynamics. This chapter is based on the published work [24] and its preliminary version [20].

2.1 AN INTRODUCTION TO THE RENDEZVOUS PROBLEM

Considering the increasing need for satellites servicing in space, the capability of operating an active spacecraft, the *follower* denoted by F, in close proximity of a satellite, the *leader* denoted by L, will be crucial for fulfilling complex safe space missions objectives comprising inspection, repairing, refueling, or monitoring [38]. The whole relative spacecraft maneuvering process composes what is known as the rendezvous and proximity operations, which mainly consists in getting the follower from one orbit to a box near the leader (close range rendezvous) [66], [33] and then in beginning the proximity operations required by the mission objectives. When dealing with the preliminary planning phase of space missions, it is customary to approximate actual finite-thrust powered phases of finite duration by impulsive maneuvers. The impulsive approximation for the thrust means that instantaneous velocity jumps are applied to the chaser when firing, whereas its position is continuous. This assumption, made in this work, has proved to be very useful in reducing the complexity of guidance and control design and has been widely used in the literature dedicated to rendezvous (see [38], [34], [33] and references therein).

In this work, we are mainly interested in the proximity maneuver for which it is highly recommended to design safe impulsive maneuvers guiding the follower, from one point to a specified tolerance region in the proximity of the leader where the relative motion of the follower will be periodic and bounded. To this end, consider the Keplerian assumptions, that are: 1. the interacting bodies are spherically symmetric and can be treated as point masses, 2. the only forces acting on the interacting bodies are their mutual gravitational forces, 3. the orbiting body has insignificant mass with respect to the central body. Under

these assumptions, the relative nonlinear motion between spacecraft is globally bounded [46] while the linearized relative motion equations include a secular term leading the chaser to drift away from the follower. Different conditions for the periodicity of the linearized equations of the nonlinear relative motion have been given in the literature. For instance, the authors of [4] state that the identity of the semi-major axis of the spacecraft orbits is a necessary and sufficient condition for periodicity, while Inalhan in [50] proposed a periodicity condition at perigee, for the linearized relative motion and for arbitrary eccentricity in a Cartesian and local framework. It is important to notice that different parametrizations (Cartesian coordinates, orbital elements) of the relative motion have been used in these previous developments.

Here we consider the parametric expression for the relative motion proposed in [34] and used to characterize in a simple way box-constrained periodic relative motions [35]. Using that parametric expression, any relative periodic trajectory is defined, in a linearized context, by 5 constant parameters. In particular, building on the result presented in [34], the contribution of the present work is twofold. First, we propose a new coordinate transformation which leads to a simplified characterization of periodic trajectories when applied to the Tschauner-Hempel equations of the elliptic linearized relative motion. The Tschauner-Hempel equations, developed in the 60's, are solutions to the linearized satellites relative dynamics with a particularly useful form. Second, three different hybrid feedback-control laws are designed by taking advantage of the particular formulation of the rendezvous problem. The use of the hybrid framework [45] for representing nonlinear hybrid dynamical systems (whose solutions exhibit continuous evolution and impulsive behavior) allows us to state and prove suitable stability properties of the proposed impulsive control laws (including, e.g., the one originally presented in [33]) when applied to the linear time-varying dynamics of the closed-loop system.

Along this first part of the manuscript, we will refer with a, e, ν and T to, respectively, the semi-major orbit axis, the orbit eccentricity, the orbit true anomaly, and the orbital period of the leader's orbit, as illustrated in Figure 2.1. With $\mu_g = 398600.4415 \times 10^9$ $\mathrm{m}^3/\mathrm{s}^2$ we refer to the standard gravitational parameter for the Earth, i.e. the constant that relates the gravitational force acting on the orbiting body with the central body mass (i.e. the Earth) and the relative distance. Given a generic function $\nu \mapsto g(\nu)$, $g'(\nu)$ represents the differentiation of the function $g(\nu)$ with respect to the true anomaly ν.

2.2 LTI STATE-SPACE FOR THE LINEARIZED RELATIVE EQUATIONS OF MOTION

2.2.1 Hybrid form of the linearized relative equations of motion

The proximity operations between two spacecraft are characterized by the use of relative navigation since the separation between spacecraft is sufficiently small In this framework, the relative motion of the follower is described in the Local-Vertical-Local-Horizontal (LVLH) frame attached to the leader [66]. The origin of the coordinate frame is located at the center of mass of the leader and the

space is spanned by $(x,\ y,\ z)$ where the z axis is in the radial direction (R-bar) oriented towards the center of the Earth, the y axis is perpendicular to the leader orbital plane and pointing in the opposite direction of the angular momentum (h-bar) while the x axis is chosen such that $x = y \times z$ (see Figure 2.2).

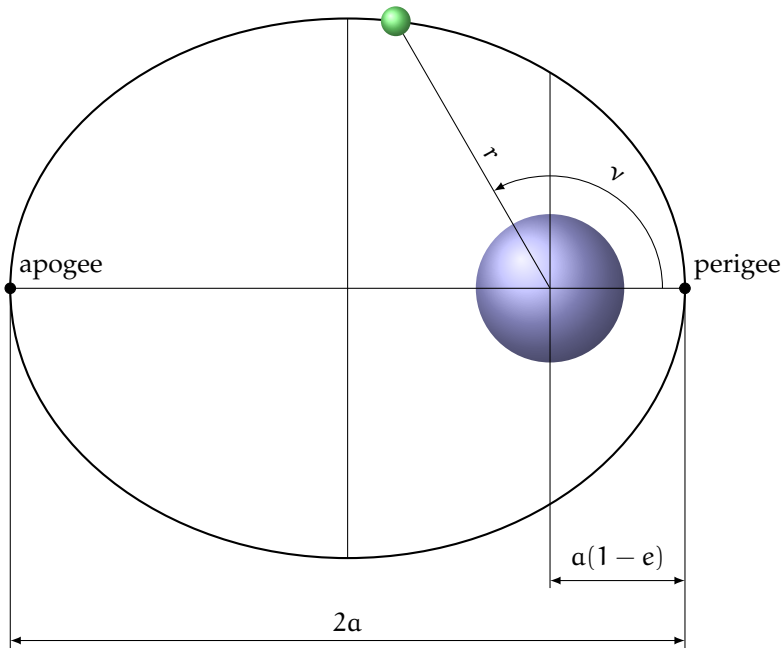

Figure 2.1: Orbital data used along the manuscript.

Under Keplerian assumptions (no orbital perturbations are considered) and an elliptic reference orbit, the equations of motion for the relative motion in the LVLH frame may be linearized for close separation between the leader and the follower [5, Chapter 5, Section 5.6.1]:

$$\begin{aligned} \dot{X} &= A(t)X && \text{free motion} \\ X^{+} &= X + \begin{bmatrix} 0_{3\times 3} \\ I_3 \end{bmatrix} \int_{t^-}^{t^+} \frac{f(\tau)}{m_F}\, d\tau && \begin{array}{c}\text{when applying} \\ \text{impulsive thrusts,}\end{array} \end{aligned} \tag{2.1}$$

where state $X = (x, y, z, dx/dt, dy/dt, dz/dt)$ represents positions and velocities in the three fundamental axes of the LVLH frame, $f(t)$ is the thrust vector, X^{+} is the state vector right after the impulsive thrust, m_F, the mass of the follower, is assumed constant, and matrix $A(t)$ is a suitable periodic function of time t given by:

$$A(t) := \begin{bmatrix} 0 & 0 & 0 & 1 & 0 & 0 \\ 0 & 0 & 0 & 0 & 1 & 0 \\ 0 & 0 & 0 & 0 & 0 & 1 \\ \dot{\nu}^2 + 2k^4\rho^3(\nu) & 0 & \ddot{\nu} & 0 & 0 & 2\dot{\nu} \\ 0 & \dot{\nu}^2 - k^4\rho^3(\nu) & 0 & 0 & 0 & 0 \\ -\ddot{\nu} & 0 & -k^4\rho^3(\nu) & -2\dot{\nu} & 0 & 0 \end{bmatrix}, \tag{2.2}$$

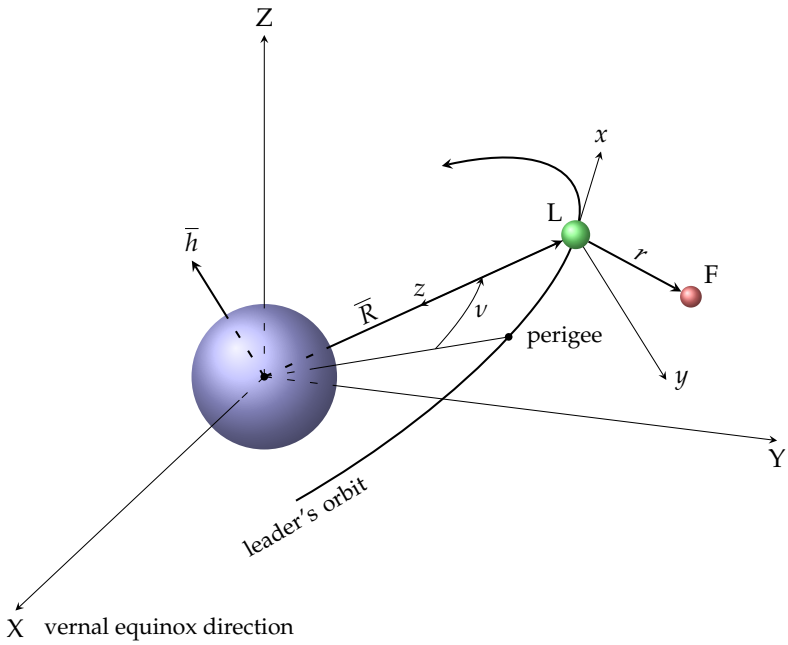

Figure 2.2: LVLH frame for relative spacecraft dynamics.

where we recall that:

$$\dot{\nu} := \frac{d\nu}{dt} = \frac{n}{(1-e^2)^{3/2}} \underbrace{(1+e\cos\nu)}_{:=\rho(\nu)}{}^2 =: k^2\rho(\nu)^2, \tag{2.3}$$

where $n = \sqrt{\frac{\mu_g}{a^3}} = 2\pi/T$ is the mean motion of the leader orbit, satisfying for any fixed ν_0, t_0,

$$\nu - \nu_0 = 2\pi \quad \Rightarrow \quad n(t-t_0) = 2\pi. \tag{2.4}$$

We may define the impulsive control input (essentially equivalent to velocity jumps in the three axes) as:

$$\Delta v(t_k) := \int_{t_k^-}^{t_k^+} \frac{1}{m_F} \begin{bmatrix} f_x(t) \\ f_y(t) \\ f_z(t) \end{bmatrix} dt, \tag{2.5}$$

which is directly associated to the fuel consumption and where t_k is a generic firing time.

In order to simplify the linearized equations (2.1) and (2.2), classical derivations dating back to the seminal publications of Lawden [60, Chapter 5] and Tschauner-Hempel [101] correspond to first applying a change of independent variable from time t to true anomaly ν, and then introducing the following

coordinate change which is indeed useful for simplifying the expression of the dynamics:

$$T(\nu) := \begin{bmatrix} \rho(\nu) I_3 & 0_{3\times 3} \\ \rho(\nu)' I_3 & \rho(\nu) I_3 \end{bmatrix}, \tag{2.6}$$

where $\rho(\nu)' := d\rho(\nu)/d\nu$. This leads to the following hybrid representation of the so-called Tschauner-Hempel (TH) equations with a new state $\tilde{X}(\nu)$ replacing $X(t)$:

$$\begin{aligned} \tilde{X}' &= \tilde{A}(\nu)\tilde{X} && \text{during free motion,} \\ \tilde{X}^+ &= \tilde{X} + \underbrace{\frac{1}{k^4\rho(\nu)^3}\begin{bmatrix} 0_{3\times 3} \\ I_3 \end{bmatrix}}_{=:\tilde{B}(\nu)} u && \text{when applying impulsive thrusts,} \end{aligned} \tag{2.7}$$

where $u = \Delta v$ represents the applied impulse, state $\tilde{X} = (\tilde{x}, \tilde{y}, \tilde{z}, d\tilde{x}/d\nu, d\tilde{y}/d\nu, d\tilde{z}/d\nu)$ represents positions and velocities with respect to ν, and

$$\tilde{A}(\nu) := \begin{bmatrix} 0 & 0 & 0 & 1 & 0 & 0 \\ 0 & 0 & 0 & 0 & 1 & 0 \\ 0 & 0 & 0 & 0 & 0 & 1 \\ 0 & 0 & 0 & 0 & 0 & 2 \\ 0 & -1 & 0 & 0 & 0 & 0 \\ 0 & 0 & \frac{3}{\rho(\nu)} & -2 & 0 & 0 \end{bmatrix}. \tag{2.8}$$

2.2.2 A new fundamental solution to the TH equations

In this chapter, we propose the two following additional transformations, the first one arising from similar observations to those in [33], and the second one arising from a Floquet-Lyapunov derivation. Although the state-space equation (2.7) is linear time-varying, $\tilde{A}(\nu)$ is simple enough to allow for the derivation of the autonomous solution of (2.7) via the computation of a fundamental matrix $\varphi_{\nu_0}(\nu)$ and a transition matrix $\tilde{\Phi}(\nu, \nu_0)$. For instance, the so-called Yamanaka-Ankersen form of this transition matrix has been proposed in [104]. Here, a new fundamental matrix is proposed, corresponding to

$$\varphi_{\nu_0}(\nu) := \begin{bmatrix} 0 & 0 & \rho^2 & -c\left(1+\frac{1}{\rho}\right) & s\left(1+\frac{1}{\rho}\right) & \rho^2 J \\ \frac{c}{\rho} & \frac{s}{\rho} & 0 & 0 & 0 & 0 \\ 0 & 0 & -e\,s & s & c & \frac{2}{3}\text{-}esJ \\ 0 & 0 & -2\,e\,s & 2s & 2c\text{-}e & 1\text{-}2esJ \\ -\frac{s}{\rho} & \frac{c}{\rho} & 0 & 0 & 0 & 0 \\ 0 & 0 & -e\,s' & s' & c' & \text{-}e\left(s'J+\frac{s}{\rho^2}\right) \end{bmatrix} \tag{2.9}$$

where the following shortcuts are used (with a slight abuse of notation):

$$\rho = \rho(\nu),\ s = \sin(\nu)\rho(\nu),\ c = \cos(\nu)\rho(\nu), \tag{2.10}$$

$$J = J(\nu, \nu_0) := \int_{\nu_0}^{\nu} \frac{1}{\rho(u)^2} du = \frac{n}{(1-e^2)^{3/2}}(t - t_0). \tag{2.11}$$

The 6 columns of $\varphi_{\nu_0}(\nu)$ form a basis spanning the 6-dimensional vector space of autonomous solutions of (2.7), since each column is indeed a solution of the autonomous equation (2.7), and

$$\det(\varphi_{\nu_0}(\nu)) = \frac{e^2-1}{3} \neq 0\ ,\ \forall\, e \in [0,1)\,. \tag{2.12}$$

These solutions are periodic except for the secular drift term $J(\nu,\nu_0)$, which zeroes-out only when $\nu = \nu_0$. For this special case, we may appreciate the usefulness of the fundamental matrix in (2.9), which leads to defining the change of coordinates in (2.15), inducing the simplified free motion dynamics in (2.17). The state transition matrix of the LTV free motion in (2.7) is then easily obtained as

$$\tilde{\Phi}(\nu,\nu_0) := \varphi_{\nu_0}(\nu)\varphi_{\nu_0}(\nu_0)^{-1}. \tag{2.13}$$

The particular interest of considering the fundamental matrix $\varphi_{\nu_0}(\nu)$ instead of the one used in the reference [104] appears clearly in the following, when trying to obtain the simplest possible LTI expression for the relative dynamical equations (2.7) via a Floquet-Lyapunov similarity transformation.

2.2.3 A periodic similarity transformation

Our first objective is to characterize the periodic autonomous solutions associated to (2.9) by transforming $\tilde{A}(\nu)$ into a convenient sparse dynamic matrix via a well chosen similarity transformation as proposed in [34]. The similarity transformation used in this chapter is slightly different from the one used in [34] and is given by:

$$\begin{array}{rcl} \bar{\xi}(\nu) & := & (\bar{\xi}_1(\nu),\,\ldots,\,\bar{\xi}_6(\nu)) \\ & := & C(\nu)\,\tilde{X}(\nu), \end{array} \tag{2.14}$$

where $C(\nu) := \varphi_\nu(\nu)^{-1}$ can be computed explicitly and corresponds to

$$C(\nu) = \begin{bmatrix} 0 & c_\nu & 0 & 0 & -s_\nu & 0 \\ 0 & s_\nu & 0 & 0 & c_\nu & 0 \\ 1 & 0 & -\frac{3es_\nu(1+\rho)}{\rho(e^2-1)} & \frac{es_\nu(1+\rho)}{e^2-1} & 0 & \frac{\rho^2-ec_\nu-3}{e^2-1} \\ e & 0 & -3s_\nu & s_\nu(1+\rho) & 0 & c_\nu\rho \\ 0 & 0 & \frac{3(c_\nu+e)}{e^2-1} & -\frac{c_\nu(1+\rho)+e}{e^2-1} & 0 & \frac{s_\nu\rho}{e^2-1} \\ 0 & 0 & -\frac{3(3ec_\nu+e^2+2)}{e^2-1} & \frac{3\rho^2}{e^2-1} & 0 & -\frac{3es_\nu\rho}{e^2-1} \end{bmatrix}, \tag{2.15}$$

where we used $c_\nu := \cos(\nu)$ and $s_\nu := \sin(\nu)$. We emphasize that the state in (2.14) is one among the infinitely many possible combinations of the constants appearing in the analytical solutions of [60, Chapter 5] and [101]. Alternative combinations have appeared in the literature, including those in [34] and those in [93]. For instance, we get the following linear relation between the set of

constants used in the reference [93] (and therein denoted by the symbol c) and the vector of constants $\bar{\xi}$ used herein.

$$\bar{\xi} = \begin{bmatrix} 0 & 0 & 0 & 0 & -1 & 0 \\ 0 & 0 & 0 & 0 & 0 & -1 \\ 0 & 0 & 3J/(e^2-1) & 1 & 0 & 0 \\ 0 & -1 & 0 & e & 0 & 0 \\ -1 & 0 & 0 & 0 & 0 & 0 \\ 0 & 0 & 3/(e^2-1) & 0 & 0 & 0 \end{bmatrix} \begin{bmatrix} c_1 \\ c_2 \\ c_3 \\ c_4 \\ c_5 \\ c_6 \end{bmatrix} \tag{2.16}$$

Note that, based on the results of [93] and the developments in [92], relation (2.16) may then be used to give the expression of the vector of differential orbital elements $(\delta a, \delta e, \delta i, \delta\Omega, \delta\omega, \delta M_0)$ as a function of $\bar{\xi}$. Applying the periodic similarity transformation in (2.15) to the dynamic matrix $\bar{A}(\nu)$, we get:

$$\begin{aligned} \bar{A}(\nu) &:= \left[C'(\nu)C^{-1}(\nu) + C(\nu)\tilde{A}(\nu)C^{-1}(\nu)\right], \\ &= \left[\begin{array}{cc|ccc|c} 0 & 0 & 0 & 0 & 0 & 0 \\ 0 & 0 & 0 & 0 & 0 & 0 \\ \hline 0 & 0 & 0 & 0 & 0 & \rho(\nu)^{-2} \\ 0 & 0 & 0 & 0 & 0 & 0 \\ 0 & 0 & 0 & 0 & 0 & 0 \\ 0 & 0 & 0 & 0 & 0 & 0 \end{array}\right]. \end{aligned} \tag{2.17}$$

Note that the structure of $C(\nu)$ preserves the decoupling between the motion in the leader's orbital plane (x, z) and the out-of-plane motion along y illustrated by the partitioning indicated in (2.17). Periodic autonomous solutions associated to (2.9) are characterized by constant solutions of $\bar{\xi}' = \bar{A}(\nu)\bar{\xi}$. From $\bar{A}(\nu)$, it is then possible to deduce that the states $\bar{\xi}_1$, $\bar{\xi}_2$, $\bar{\xi}_4$, $\bar{\xi}_5$, and $\bar{\xi}_6$ are constant solutions, while $\bar{\xi}_3(\nu)$ is a constant solution if and only if $\bar{\xi}_6(\nu) = 0$. This appears more clearly when computing the new state transition matrix associated to $\bar{A}(\nu)$ as:

$$\begin{aligned} \bar{\Phi}(\nu, \nu_0) &:= C(\nu)\bar{\Phi}(\nu, \nu_0)C(\nu_0)^{-1} \\ &= \left[\begin{array}{cc|ccc|c} 1 & 0 & 0 & 0 & 0 & 0 \\ 0 & 1 & 0 & 0 & 0 & 0 \\ \hline 0 & 0 & 1 & 0 & 0 & J(\nu, \nu_0) \\ 0 & 0 & 0 & 1 & 0 & 0 \\ 0 & 0 & 0 & 0 & 1 & 0 \\ 0 & 0 & 0 & 0 & 0 & 1 \end{array}\right]. \end{aligned} \tag{2.18}$$

2.2.4 A Floquet-Lyapunov similarity transformation

Before illustrating how a Floquet-Lyapunov similarity transformation is synthesized to further develop and suitably simplify the $\bar{\xi}$ dynamic in (2.17), in this section we give some notions about this tool based on [18, Chap. 1.2]. The notation used here is scoped just for this illustration.

Floquet-Lyapunov overview

Consider an LTV dynamic with state $x \in \mathbb{R}^n$:

$$\dot{x}(t) = A(t)x(t) \tag{2.19}$$

in which $A(t)$ is periodic with period T, that is:

$$A(t+T) = A(t)\,, \quad \forall t \geq 0\,. \tag{2.20}$$

The Floquet-Lyapunov transformation theory can be summarized as follows. If $S(t)$ is an invertible and periodic (of period T) similarity transformation matrix such that

$$\hat{x}(t) = S(t)x(t)\,, \tag{2.21}$$

then, the dynamic matrix in the new coordinates is given by

$$\hat{A}(t) = S(t)A(t)S(t)^{-1} + \dot{S}(t)S(t)^{-1}\,, \tag{2.22}$$

assuming that $S(t)$ and $S(t)^{-1}$ are continuously differentiable. The Floquet problem consist in finding $S(t)$ (if any) such that the dynamics matrix in the new coordinates is constant, i.e., $\hat{A}(t) = \hat{A}$. Plugging the condition $\hat{A}(t) = \hat{A}$ into equation (2.22), we obtain the following matrix differential equation

$$\dot{S}(t) = \hat{A}S(t) - S(t)A(t)\,. \tag{2.23}$$

Considering now t_0 as initial time and $S(t_0)$ as initial condition, the solution to (2.23) is given by

$$S(t) = e^{\hat{A}(t-t_0)}S(t_0)\Phi(t_0,t)\,, \tag{2.24}$$

in which $\Phi(t_0,t)$ is the state transition matrix of the dynamics (2.19). Taking now $t = t_0 + T$ and imposing the periodicity condition $S(t_0 + T) = S(t_0)$ to the solution (2.24) permits us to derive the following relation

$$\begin{aligned} S(t_0) = S(t_0+T) &= e^{\hat{A}T}S(t_0)\underbrace{\Phi(t_0+T,t_0)}_{:=\Psi(t_0)}{}^{-1} \\ &= e^{\hat{A}T}S(t_0)\Psi(t_0)^{-1}\,. \end{aligned} \tag{2.25}$$

in which we have defined the matrix $\Psi(t_0)$, known as the "monodromy matrix", that is the state transition matrix over a period. The Floquet problem reduces in finding a pair of matrices $(\hat{A}, S(t_0))$ solution to equations (2.24)-(2.25).

Since the dynamic matrix $\bar{A}(\nu)$ is periodic of period 2π, the next step consists in the application of Floquet-Lyapunov theory following the steps described above, as in [34] and [95], and in looking for a periodic similarity transformation matrix $S(\nu)$, transforming the original *LTV* dynamical system into an equivalent *LTI* dynamical system, namely:

$$\widehat{\bar{\xi}}(\nu) := S(\nu)\bar{\bar{\xi}}(\nu)\,, \tag{2.26}$$

such that

$$\widehat{\bar{\xi}}\,'(\nu) = \widehat{A}\,\widehat{\bar{\xi}}(\nu)\,, \tag{2.27}$$

and where $\widehat{A}$ is a matrix independent of ν. We know that, given $S(\nu)$, $\widehat{A}$ is given by:

$$\widehat{A} := S'(\nu)S^{-1}(\nu) + S(\nu)\bar{A}(\nu)S^{-1}(\nu) \,. \tag{2.28}$$

Via a right multiplication of (2.28) by $S(\nu)$, we obtain the differential equation:

$$S'(\nu) = \widehat{A}S(\nu) - S(\nu)\bar{A}(\nu) \,. \tag{2.29}$$

Equation (2.29) represents a matrix differential equation whose solution is given in the following equation and comes from Floquet Theory [18]. Therefore,

$$S(\nu) = \mathrm{e}^{\widehat{A}(\nu-\nu_f)}S(\nu_f)\bar{\Phi}(\nu_f,\nu) \,, \tag{2.30}$$

where $\nu_f \in [0, 2\pi]$ (f stands for Floquet) is an arbitrary parameter. Imposing the periodicity condition on $S(\nu)$ with $\nu = \nu_f + 2\pi$ in (2.30) gives:

$$S(\nu_f + 2\pi) = S(\nu_f) = \mathrm{e}^{2\pi\widehat{A}}S(\nu_f)\bar{\Phi}(\nu_f, \nu_f + 2\pi). \tag{2.31}$$

From (2.31) we get:

$$S(\nu_f) = \mathrm{e}^{2\pi\widehat{A}}S(\nu_f)\bar{\Psi}(\nu_f)^{-1} \,, \tag{2.32}$$

where $\bar{\Psi}(\nu_f) = \bar{\Phi}(\nu_f + 2\pi, \nu_f)$ is the monodromy matrix (state transition matrix over one period) of $\bar{A}(\nu)$. Denoting by T the leader's orbital period, we have:

$$J(\nu_f + 2\pi, \nu_f) = \frac{n}{(1-e^2)^{3/2}}T = \frac{2\pi}{(1-e^2)^{3/2}}. \tag{2.33}$$

Using (2.11) and (2.18), the monodromy matrix $\bar{\Psi}(\nu_f)$ is therefore given by:

$$\bar{\Psi}(\nu_f) = \left[\begin{array}{cc|ccc|c} 1 & 0 & 0 & 0 & 0 & 0 \\ 0 & 1 & 0 & 0 & 0 & 0 \\ \hline 0 & 0 & 1 & 0 & 0 & \dfrac{2\pi}{(1-e^2)^{3/2}} \\ 0 & 0 & 0 & 1 & 0 & 0 \\ 0 & 0 & 0 & 0 & 1 & 0 \\ 0 & 0 & 0 & 0 & 0 & 1 \end{array}\right] . \tag{2.34}$$

In solving (2.30) under constraint (2.32), we look for a solution having the same structure as $\bar{A}(\nu)$ in (2.17), namely satisfying $\widehat{A}^2 = 0$, which gives:

$$\mathrm{e}^{\widehat{A}\nu} = \sum_{k=1}^{\infty}\frac{\nu^k}{k!}\widehat{A}^k = I + \nu\widehat{A}. \tag{2.35}$$

Equation (2.32) becomes:

$$S(\nu_f)\bar{\Psi}(\nu_f) = (I + 2\pi\widehat{A})S(\nu_f) \,, \tag{2.36}$$

or equivalently:

$$2\pi\widehat{A} = S(\nu_f)\bar{\Psi}(\nu_f)S(\nu_f)^{-1} - I \,, \tag{2.37}$$

where $S(\nu_f)$ is an arbitrary matrix parameter. Here we select $S(\nu_f)$ as the identity matrix, to get

$$\widehat{A} = \left[\begin{array}{cc|ccc|c} 0 & 0 & 0 & 0 & 0 & 0 \\ 0 & 0 & 0 & 0 & 0 & 0 \\ \hline 0 & 0 & 0 & 0 & 0 & (1-e^2)^{-3/2} \\ 0 & 0 & 0 & 0 & 0 & 0 \\ 0 & 0 & 0 & 0 & 0 & 0 \\ 0 & 0 & 0 & 0 & 0 & 0 \end{array}\right]. \tag{2.38}$$

The Floquet-Lyapunov similarity transformation is finally computed from equation (2.30) as:

$$\begin{aligned} S(\nu) &= \left(I + (\nu - \nu_f)\widehat{A}\right) S(\nu_f)\Phi(\nu_f, \nu) \\ &= \left[\begin{array}{cc|ccc|c} 1 & 0 & 0 & 0 & 0 & 0 \\ 0 & 1 & 0 & 0 & 0 & 0 \\ \hline 0 & 0 & 1 & 0 & 0 & \dfrac{\sigma(\nu)}{(1-e^2)^{3/2}} \\ 0 & 0 & 0 & 1 & 0 & 0 \\ 0 & 0 & 0 & 0 & 1 & 0 \\ 0 & 0 & 0 & 0 & 0 & 1 \end{array}\right], \end{aligned} \tag{2.39}$$

where we introduced the function:

$$\begin{aligned} \sigma(\nu) :=& (\nu - \tilde{\nu}) - n(t - \tilde{t}) \\ =& (\nu - \tilde{\nu}) - (M - \tilde{M}) \\ =& \Delta\nu - \Delta M, \end{aligned} \tag{2.40}$$

based on an arbitrary true anomaly value $\tilde{\nu}$ (in our simulations we select $\tilde{\nu} = 0$) corresponding to a specific time value $\tilde{t}$ (in our simulations we select $\tilde{t} = 0$). Function σ in (2.40) is clearly periodic and bounded, due to the geometric dependence of ν and M when the leader follows a Keplerian elliptic motion.

The following result establishes a first contribution of this work, showing that dynamics (2.7) can be transformed to a convenient linear time-invariant form by exploiting transformations (2.6), (2.15), and (2.39). The proof of the lemma is omitted as it follows from the mathematical derivations discussed above, and from periodicity of matrices C and S.

Lemma 2.1. *Consider matrices in (2.15) and (2.39). Then the following operation:*

$$\widehat{\xi} := R(\nu)\tilde{X} := S(\nu)\, C(\nu)\tilde{X}\,, \tag{2.41}$$

is a linear time-varying coordinate change, namely $R(\nu)$ is invertible for all ν and R and R^{-1} are uniformly bounded. Moreover, R is periodic and transforms $\tilde{A}(\nu)$ into the following time-invariant form:

$$\begin{aligned} \widehat{A} \;:=\; & R'(\nu)R^{-1}(\nu) + R(\nu)\tilde{A}(\nu)R^{-1}(\nu) \\ =\; & \left[\begin{array}{cc|ccc|c} 0 & 0 & 0 & 0 & 0 & 0 \\ 0 & 0 & 0 & 0 & 0 & 0 \\ \hline 0 & 0 & 0 & 0 & 0 & (1-e^2)^{-3/2} \\ 0 & 0 & 0 & 0 & 0 & 0 \\ 0 & 0 & 0 & 0 & 0 & 0 \\ 0 & 0 & 0 & 0 & 0 & 0 \end{array}\right]. \end{aligned} \tag{2.42}$$

From the peculiar structure (quasi Jordan form) of the dynamic matrix $\widehat{A}$, the following result, that was already noticed for a similar coordinate changes in [33], can be proven.

Lemma 2.2. *A solution of the original dynamics (2.1) is periodic during free motion if and only if it is transformed into a constant state $\widehat{\xi}$ with the last component being zero.*

Proof. *If the last component of $\widehat{\xi}$ is zero, then matrix $\widehat{A}$ in (2.42) clearly implies that $\widehat{\xi}$ remains constant during flow (free motion). As a consequence, the free motion in the original coordinates X of (2.1) is a linear combination of the first five columns of the periodic transformation $R(\nu)$ followed by the periodic time-scale change from ν to t.*

Conversely, assume that the last component of $\widehat{\xi}$ is nonzero. Then during free motion that component remains constant (the last row of $\widehat{A}$ is zero) and the third component of $\widehat{\xi}$ ramps up to infinity due to the off diagonal term $(1-e^2)^{-3/2} \neq 0$ appearing in $\widehat{A}$. As a consequence $|\widehat{\xi}|$ diverges and so does also $\bar{X}$ because $R(\nu)$ is bounded and has bounded inverse (from Lemma 2.1). Also X must then diverge as $t \to \infty$ because the time-scale change is periodic. □

Based on Lemma 2.2, it is convenient to represent the system in terms of the error with respect to a desired motion $\widehat{\xi}^{\,ref}$:

$$\widehat{\xi}^{\,ref} := [\widehat{\xi}_1^{\,ref} \ \widehat{\xi}_2^{\,ref} \ \widehat{\xi}_3^{\,ref} \ \widehat{\xi}_4^{\,ref} \ \widehat{\xi}_5^{\,ref} \ 0]^\top, \tag{2.43}$$

so that one may analyze the dynamics of the mismatch vector:

$$\widehat{\varepsilon} := \widehat{\xi} - \widehat{\xi}^{\,ref} \tag{2.44}$$

between the coordinate $\widehat{\xi}$ in (2.41) and a constant reference value in (2.43), representing a desired target periodic motion.

Moreover, according to the coordinate change given in (2.41), and to the results of Lemma 2.1, matrix $\widehat{B}(\nu) = R(\nu)\tilde{B}(\nu)$ is a periodic function of ν arising from combining the similarity transformation in (2.41) with the input matrix in (2.7), and corresponds to the following matrix.

$$\widehat{B}(\nu) = R(\nu)\tilde{B}(\nu) = \frac{1}{k^2\rho^2(1-e^2)} \begin{bmatrix} 0 & -(1-e^2)\rho s_\nu & 0 \\ 0 & (1-e^2)\rho c_\nu & 0 \\ -e(1+\rho)\rho s_\nu - \dfrac{3\sigma\rho^3}{(1-e^2)^{3/2}} & 0 & \dfrac{3\sigma e\rho^2 s_\nu}{(1-e^2)^{3/2}} - \rho^3 + \rho^2 + 2\rho \\ (1-e^2)(1+\rho)\rho s_\nu & 0 & (1-e^2)\rho^2 c_\nu \\ (1+\rho)\rho c_\nu + e\rho & 0 & -\rho^2 s_\nu \\ -3\rho^3 & 0 & 3e\rho^2 s_\nu \end{bmatrix} \tag{2.45}$$

3 CONTROLLER DESIGN

In this chapter we propose a hybrid representation of the dynamics subject to impulsive thrusts in order to develop three different control laws for the stabilization of a desired periodic orbit. The proposed controllers performance is tested with several simulation studies also involving nonlinearities neglected in the design phase. This chapter is based on the published work [24] and its preliminary version [20].

3.1 IMPULSIVE CONTROL OF THE RELATIVE DYNAMICS

The coordinate transformation presented in Lemma 2.1 of the previous section is a useful means for suitably designing an impulsive control law assigning the firing times ν_k in (2.7) and also the corresponding selections of u at time ν_k to stabilize the periodic motions characterized in Lemma 2.2.

Problem 3.1. *Given plant (2.1) and its equivalent form (2.7), design a state feedback impulsive control law selecting the firing instants ν_k, $k \in \mathbb{N}$ and the corresponding inputs $u(\nu_k)$ such that for any selection of reference (2.43), a suitable set exists wherein $\widehat{\xi} = \widehat{\xi}^{\,ref}$ is globally asymptotically stable for the closed-loop dynamics.*

To solve Problem 3.1, in this section we will propose hybrid control laws relying on the presence of a timer τ in charge of the sequencing of the impulsive control actions. Then, using the hybrid systems notation in [45] and state $\widehat{\varepsilon} := \widehat{\xi} - \widehat{\xi}^{\,ref}$, we may write the following general dynamic description of the closed loop, enjoying the desirable property that timers ν and τ evolve in the compact set $[0, 2\pi]$ and that the flow equation for $\widehat{\varepsilon}$ is $\widehat{\varepsilon}\,' = \widehat{A}\,\widehat{\varepsilon}$, because $\widehat{A}\,\widehat{\xi}^{\,ref} = 0$:

$$\begin{cases} \widehat{\varepsilon}\,' = \widehat{A}\,\widehat{\varepsilon}, \\ \nu' = 1, \\ \tau' = -1, \end{cases} \qquad (\widehat{\varepsilon}, \nu, \tau) \in \mathcal{C}, \tag{3.1a}$$

$$\begin{cases} \widehat{\varepsilon}^{+} = \widehat{\varepsilon}, \\ \nu^{+} = 0, \\ \tau^{+} = \tau, \end{cases} \qquad (\widehat{\varepsilon}, \nu, \tau) \in \mathcal{D}_{\nu}, \tag{3.1b}$$

$$\begin{cases} \widehat{\varepsilon}^{+} = \widehat{\varepsilon} + \widehat{B}(\nu)\gamma_u\left(\widehat{\varepsilon}, \nu\right), \\ \nu^{+} = \nu, \\ \tau^{+} = \gamma_\tau\left(\widehat{\varepsilon}, \nu\right), \end{cases} \qquad (\widehat{\varepsilon}, \nu, \tau) \in \mathcal{D}_{u}. \tag{3.1c}$$

In equation (3.1), the impulsive control law has been selected as a feedback controller:

$$u = \gamma_u(\widehat{\varepsilon}, \nu), \quad \tau^{+} = \gamma_\tau(\widehat{\varepsilon}, \nu). \tag{3.2}$$

Equation (3.1) is a compact representation of the impulsive feedback control action as a set of dynamical constraints that solutions should satisfy for their correct evolution. In particular, using an overall state $\zeta = (\widehat{\varepsilon}, \nu, \tau)$, this dynamics falls into the general class of systems studied in [45]:

$$\begin{array}{ll} \zeta \in \mathcal{C}, & \dot{\zeta} = F(\zeta), \\ \zeta \in \mathcal{D}, & \zeta^+ \in G(\zeta). \end{array} \tag{3.3}$$

It is worth to point out that, due to notation reasons, in this case capital F represents a single valued mapping and not a set valued mapping, in contrast to what presented in the hybrid framework introduction of Section 1.4,. For our model, the following selections are made:

$$\mathcal{D}_\nu := \mathbb{R}^6 \times \{2\pi\} \times [0, 2\pi], \tag{3.4a}$$
$$\mathcal{D}_u := \mathbb{R}^6 \times [0, 2\pi] \times \{0\}, \tag{3.4b}$$
$$\mathcal{D} := \mathcal{D}_\nu \cup \mathcal{D}_u, \tag{3.4c}$$
$$\mathcal{C} := \overline{(\mathbb{R}^6 \times [0, 2\pi] \times [0, 2\pi]) \setminus \mathcal{D}}, \tag{3.4d}$$

which, due to (3.4c), is a choice that prioritizes jumps. In particular, based on (3.1), functions F and G in (3.3) are selected as:

$$F(\zeta) = \begin{bmatrix} \widehat{A}\,\widehat{\xi} \\ 1 \\ -1 \end{bmatrix}; \; G(\zeta) = \bigcup_{i \in \{u,\nu\} \text{ s.t. } \zeta \in \mathcal{D}_i} G_i(\zeta); \tag{3.5a}$$

$$G_\nu(\zeta) = \begin{bmatrix} \widehat{\varepsilon} \\ 0 \\ \tau \end{bmatrix}; \; G_u(\zeta) = \begin{bmatrix} \widehat{\varepsilon} + \widehat{B}(\nu)\gamma_u(\widehat{\varepsilon}, \nu) \\ \nu \\ \gamma_\tau(\widehat{\varepsilon}, \nu) \end{bmatrix}, \tag{3.5b}$$

in which, differently from what has been presented in Chapter 1 and for consistency of the notation of the proposed model, F represents a function instead of a set-valued map. The proposed hybrid model (3.1), (3.4) (or its equivalent compact form in (3.3), (3.4), (3.5)), corresponds to the following intuitive behavior of our solutions.

- Timer ν is used as an additional state to keep track of the periodic time-varying nature of the dynamics. Using the jump set in (3.4a) ensures that the timer is reset to zero each time it reaches the value 2π, thereby being confined [1] to the compact set $[0, 2\pi]$.
- Thrusters are fired according to (3.1c) whenever $\zeta \in \mathcal{D}_u$, namely when the timer τ crosses zero (see (3.4b)). Then, at each time during the evolution of the dynamics, state τ captures the information about how long we need to wait until the next impulsive control action.
- Each time an impulsive control action is triggered, the associated control law corresponds to the value of the two functions

$$\begin{array}{l} \gamma_u : \mathbb{R}^6 \times [0, 2\pi] \to \mathbb{R}^3, \\ \gamma_\tau : \mathbb{R}^6 \times [0, 2\pi] \to [0, 2\pi], \end{array} \tag{3.6}$$

1 To avoid situations where arbitrarily small noise may cause solutions to stop because they exit $\mathcal{C} \cup \mathcal{D}$, it may be useful to replace $\{2\pi\}$ by $[2\pi, 2\pi + \delta]$ for any positive δ in (3.4a).

the first one assigning the current selection of the impulsive input $\widehat{u}$ (based on (3.2)), and the second one preassigning the time to wait until the next impulsive input should be applied. Note that the range of γ_τ is bounded so that solutions will only take values of τ in the bounded set $[0, 2\pi]$.

Within the proposed hybrid context, the stability goal formulated in Problem 1 is well characterized in terms of the stability properties of the bounded attractor

$$\mathcal{A} := \{0\} \times [0, 2\pi] \times [0, 2\pi], \tag{3.7}$$

which may be analyzed using the tools of [45, Chapter 7], because selections (3.4), (3.5) satisfy the hybrid basic conditions of [45, Assumption 6.5].

3.2 CONTROL LAWS

In this section, we propose three different selections for the impulsive control law (3.2) solving Problem 1. They are comparatively illustrated on the example studies of Section 3.3.

3.2.1 Periodic norm-minimizing control law

We will refer to the controller developed in this section as Controller A. While formulation (3.1), (3.2) is general enough to allow for aperiodic optimized sampling, the simplest possible selection of function γ_τ in (3.2) is given by periodic thrusters firing, corresponding to a certain period $\overline{\nu} \in [0, 2\pi]$ fixed a priori. For instance,

$$\gamma_\tau(\widehat{\varepsilon}, \nu) = \overline{\nu}, \tag{3.8}$$

encodes the fact that each pair of consecutive jumps has a fixed angular distance of $\overline{\nu}$.

Regarding the selection of the stabilizer γ_u, to be evaluated periodically, we make here a conservative selection leading to the useful feature that after each impulse, the state $\widehat{\varepsilon}_6 = \widehat{\xi}_6$ is driven to zero. Then, in light of Lemma 2.2, in the absence of noise the spacecraft evolves through periodic (therefore bounded) motions. In particular, the following optimal selection is chosen:

$$\begin{aligned} u^\star = \underset{u \in \mathbb{R}^3}{\operatorname{argmin}} \, & |\widehat{\varepsilon}^+|^2, \text{ subject to:} \\ & \widehat{\varepsilon}^{\,+} = \widehat{\varepsilon} + \widehat{B}(\nu) u, \quad \widehat{\varepsilon}_6^{\,+} = 0. \end{aligned} \tag{3.9}$$

Due to the specific structure of matrix function $\widehat{B}(\nu)$ in (2.45) at the top of page 23, we may provide an explicit form of the minimizer in (3.9) after defining the following quantities:

$$\widehat{b}_6(\nu) := \frac{1}{k^2} \begin{bmatrix} -\frac{3\rho}{1-e^2} \\ 0 \\ \frac{3e\sin(\nu)}{1-e^2} \end{bmatrix}, \quad \widehat{B}_6^{\perp}(\nu) := \begin{bmatrix} e\sin(\nu) & 0 \\ 0 & 1 \\ \rho(\nu) & 0 \end{bmatrix}, \tag{3.10a}$$

which clearly satisfy $\widehat{b}_6(\nu)^\top \widehat{B}_6^\perp(\nu) = 0$ because matrix $\widehat{B}_6^\perp(\nu)$ generates the orthogonal complement of $\widehat{b}_6(\nu)$.

With these definitions in place, we may write the explicit expression of the proposed control law as:

$$\gamma_u(\widehat{\varepsilon}, \nu) = u_6 - \widehat{B}_6^\perp(\nu)(\widehat{B}(\nu)\widehat{B}_6^\perp(\nu))^{-L}(\widehat{\varepsilon} + \widehat{B}(\nu)\, u_6)$$
$$\text{with } u_6 := -\frac{\widehat{b}_6(\nu)}{|\widehat{b}_6(\nu)|^2}\widehat{\varepsilon}_6, \tag{3.10b}$$

where $M^{-L} = (M^\top M)^{-1}M^\top$ denotes the left pseudo-inverse of matrix M. The effectiveness of selection (3.10b) is stated in the next proposition.

Proposition 3.1. *For any value of ν, the inverses in function (3.10) always exist and selection (3.10) coincides with the minimizer in (3.9), namely $\gamma_u(\widehat{\varepsilon}, \nu) = u^\star$.*

Proof. *The existence of the inverses easily follows from the fact that*

$$\det\left((\widehat{B}(\nu)\widehat{B}_6^\perp(\nu))^\top(\widehat{B}(\nu)\widehat{B}_6^\perp(\nu))\right) \tag{3.11}$$
$$= (1-e)^2 + 2e(1+\cos(\nu)) > 0 \tag{3.12}$$
$$|\widehat{b}_6(\nu)|^2 = \frac{9\rho^4(\rho^2 + e^2\sin(\nu)^2)}{(1-e^2)^2} > 0, \tag{3.13}$$

which clearly indicates that the left inverse in the first line of (3.10b) and u_6 in the second line of (3.10b) can be evaluated. To show that (3.10) coincides with the minimizer in (3.9), first notice that constraint $\widehat{\varepsilon}_6^{\,+} = 0$ is automatically ensured by $\widehat{b}_6(\nu)^\top \widehat{B}_6^\perp(\nu) = 0$, which implies $\widehat{\varepsilon}_6^{\,+} = \widehat{b}_6^\top(\nu)u_6 = 0$. Therefore, noting that $\widehat{B}_6^\perp(\nu)$ is the orthogonal complement of $\widehat{b}_6(\nu)$, all possible inputs guaranteeing that $\widehat{\varepsilon}_6^{\,+} = 0$ are parametrized by $\widehat{v}^\star$ in:

$$u = u_6 + \widehat{B}_6^\perp(\nu)\, v^\star. \tag{3.14}$$

Therefore, the solution to (3.9) corresponds to (3.14) with $\widehat{v}^\star$ being the solution to the following unconstrained least squares problem:

$$v^\star = \underset{\widehat{v}}{\operatorname{argmin}}\, |\widehat{\varepsilon} + \widehat{B}(\nu)u_6 + \widehat{B}(\nu)\widehat{B}_6^\perp(\nu)\, v|^2. \tag{3.15}$$

Then, as is well known (see, e.g., [12, Ex.1 pg 92]), the minimizer $v^\star$ is given by:

$$v^\star = -(\widehat{B}(\nu)\widehat{B}_6^\perp(\nu))^{-L}(\widehat{\varepsilon} + \widehat{B}(\nu)\, u_6), \tag{3.16}$$

which, substituted in (3.14), gives (3.10b), as to be proven. □

Remark 3.1. *Based on Proposition 3.1, a desirable property of control law (3.8), (3.10) is that, in light of Lemma 2.2, it instantaneously minimizes the norm of $\widehat{\varepsilon}$ constrained to the fact that the subsequent motion be periodic. Since the norm of $\widehat{b}_6$ in (3.10a) is never zero, then clearly, equation (3.10b) is always well-posed and ensures that $\widehat{\varepsilon}_6^{\,+} = 0$. In addition to this, instantaneously minimizing the norm of $\widehat{\varepsilon}$ also ensures the best possible decrease at the specific fixed instant of time enforced by the periodic selection. With this logic in place, we can guarantee stability of the closed-loop but not convergence. Indeed, we can guarantee non-increase of $|\widehat{\varepsilon}|$ across jumps but there is no*

guarantee of obtaining a strict decrease. As a result, we anticipate a slow convergence (if any) in our simulation section when using this controller. Despite this fact, the choice (3.8), (3.10) is still an interesting one because it ensures that approaching between the two satellites is performed through periodic (bounded) motions, leading to some degree of fault tolerance (in case of malfunctioning, the satellite is on a stable relative orbit). ⌟

The following theorem certifies that the proposed controller solves part of Problem 3.1.

Theorem 3.1. *Given control law (3.8), (3.10), the attractor $\mathcal{A}$ in (3.7) is uniformly globally stable for the arising closed-loop dynamics with plant (3.1).*

Proof. *First notice that $|(\widehat{\varepsilon}, \nu, \tau)|_{\mathcal{A}} = |\widehat{\varepsilon}|$. Recall that a generic solution $(\mu, j) \mapsto \widehat{\varepsilon}(\mu, j)$ to the hybrid dynamics has a domain $\operatorname{dom}\widehat{\varepsilon}$ parametrized by a flowing direction and by a jumping direction j (see [45, Chap. 2] for details). Here the flowing direction is represented by the amount μ of true anomaly elapsed since the initial condition, as opposed to continuous time t for a classical hybrid systems representation. We first realize that before the first impulse, all solutions evolve in free motion along the LTI flow dynamics in (3.1), leading to:*

$$|\widehat{\varepsilon}(\mu, 0)| \leq |e^{2\pi\widehat{A}}||\widehat{\varepsilon}(0, 0)|. \tag{3.17}$$

Notice now that Proposition 3.1 ensures that $\gamma_u(\widehat{\varepsilon}, \nu) = u^\star$. In particular, after the first jump the state $\widehat{\varepsilon}_6$ remains at zero for all (hybrid) times. Then during all subsequent flows, the state $\widehat{\varepsilon}$ remains constant due to the structure of $\widehat{A}$. Moreover, across jumps, the control law is the minimizer of (3.9), clearly satisfying $|\widehat{\varepsilon}^+| \leq |\widehat{\varepsilon}|$. As a consequence, we get:

$$|\widehat{\varepsilon}(\mu, j)| \leq |\exp(2\pi\widehat{A})||\widehat{\varepsilon}(0, 0)|, \tag{3.18}$$

for all $(\mu, j) \in \operatorname{dom}\widehat{\varepsilon}$, which establishes uniform global stability. □

3.2.2 Two-step finite-time control law

We will refer to the controller developed in this section as Controller B. A second selection that we propose for the controller in (3.2) is once again periodic, thereby corresponding to selection (3.8) for γ_τ. However, it corresponds to a wiser selection of γ_u (in terms of envisioned fuel consumption), performed in similar ways to what is proposed in [33], by focusing on the overall effect on the state $\widehat{\varepsilon}$ of two impulses performed at a distance of $\overline{\nu}$ from one another. In particular, using straightforward computations, if two consecutive impulses u_1 and u_2 happen at times μ_1 and $\mu_2 = \mu_1 + \overline{\nu}$, we obtain, along the corresponding solution:

$$\begin{aligned}\widehat{\Phi}(-\overline{\nu})\widehat{\varepsilon}(\mu_2, j_2 + 1) = \\ \widehat{\varepsilon}(\mu_1, j_1) + \underbrace{\begin{bmatrix}\widehat{B}(\nu_1) & \widehat{\Phi}(-\overline{\nu})\widehat{B}(\nu_1 + \overline{\nu})\end{bmatrix}}_{:= M(\nu_1, \overline{\nu})} \begin{bmatrix}u_1 \\ u_2\end{bmatrix},\end{aligned} \tag{3.19}$$

where (μ_1, j_1) and (μ_2, j_2) denote the hybrid times before each one of the impulses, and

$$\widehat{\Phi}(\mu) = e^{\widehat{A}\mu} = \begin{bmatrix} 1 & 0 & 0 & 0 & 0 & 0 \\ 0 & 1 & 0 & 0 & 0 & 0 \\ 0 & 0 & 1 & 0 & 0 & \mu(1-e^2)^{-3/2} \\ 0 & 0 & 0 & 1 & 0 & 0 \\ 0 & 0 & 0 & 0 & 1 & 0 \\ 0 & 0 & 0 & 0 & 0 & 1 \end{bmatrix}$$

is the state transition matrix of the (LTI) flow dynamics in (3.1), and $\nu_1 = \nu(\mu_1, j_1)$.

Based on relation (3.19), and to the end of selecting u_1, u_2 in such a way that $\widehat{\varepsilon}(\mu_2, j_2 + 1)$ be zero, it is important to study the invertibility properties of matrix $M(\nu, \overline{\nu})$, which is done in the following conjecture. The result of the conjecture restricts the set of possible selections of $\overline{\nu}$ in (3.8).

Conjecture 3.1. *For any value of $\nu \in [0, 2\pi]$, matrix $M(\nu, \overline{\nu})$ in (3.19) is invertible if and only if $\overline{\nu} \neq k\pi$, $k \in \mathbb{Z}$.*

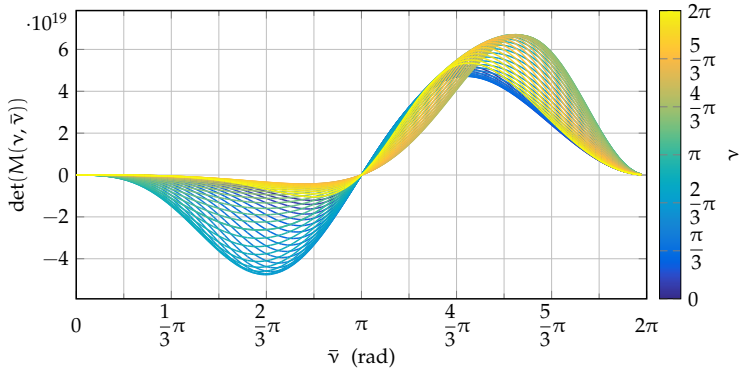

Figure 3.1: Determinant of matrix $M(\nu, \overline{\nu})$ with $e = 0.4$.

In support of the conjecture, we report in Figure 3.1 the value of the determinant of $M(\nu, \overline{\nu})$ for different values of ν (represented by the color code) and $\overline{\nu}$ (represented by the horizontal axis). The plot corresponds to the value $e = 0.4$ and similar plots are experienced for any value of $e < 1$. Proving Conjecture 3.1 is challenging from a mathematical viewpoint, but is of little interest in light of the improved results reported in Section 3.2.3.

If Conjecture 3.1 holds, for any selection $\overline{\nu} \in (0, 2\pi) \setminus \{\pi\}$, Equation (3.19) can be inverted to compute the unique pair of inputs $u_1^\star$, $u_2^\star$ ensuring $\widehat{\varepsilon}(\mu_2, j_2 + 1) = 0$ (namely that the state $\widehat{\varepsilon}$ is driven to zero after two impulses separated by $\overline{\nu}$ times). Following a receding horizon type of paradigm, we may apply the first impulse and re-evaluate the control law at the next impulse time. The above control design paradigm leads to the following selection:

$$\gamma_u(\widehat{\varepsilon}, \nu) := -\left[\, I \; 0 \,\right] M(\nu, \overline{\nu})^{-1} \widehat{\varepsilon}, \quad \gamma_\tau(\widehat{\varepsilon}, \nu) = \overline{\nu}. \tag{3.20}$$

The overall control strategy (3.8), (3.20) guarantees convergence to zero of the error $\widehat{\varepsilon}$ after two impulses, as established next.

Lemma 3.1. *If $M(\nu, \overline{\nu})$ is invertible for all $\nu \in [0, 2\pi]$, then selection (3.8), (3.20) guarantees that all solutions to (3.1) have the $\widehat{\varepsilon}$ component equal to zero after at most two jumps.*

Proof. *Consider two subsequent impulses associated to the control selections $u_j = \begin{bmatrix} I & 0 \end{bmatrix} \begin{bmatrix} u_{j,1} \\ u_{j,2} \end{bmatrix} = u_{j,1}$ and $u_{j+1} = \begin{bmatrix} I & 0 \end{bmatrix} \begin{bmatrix} u_{j+1,1} \\ u_{j+1,2} \end{bmatrix} = u_{j+1,1}$. Then, due to the property that $\begin{bmatrix} u_{j,1} \\ u_{j,2} \end{bmatrix}$ brings the state to zero after two impulses, it follows that selection $\begin{bmatrix} u_{j+1,1} \\ u_{j+1,2} \end{bmatrix} = \begin{bmatrix} u_{j,2} \\ 0 \end{bmatrix}$ is a feasible one for the second impulse. As a consequence of uniqueness, arising from relation (3.19), this is the only possible solution and we must have $\widehat{\varepsilon}^+ = 0$ after the second impulse.* □

Based on Lemma 3.1 we can now prove that our second control law solves Problem 1 as established in the next theorem.

Theorem 3.2. *Given $\overline{\nu} \in (0, 2\pi) \setminus \{\pi\}$, assume that matrix $M(\nu, \overline{\nu})$ is invertible for any value of $\nu \in [0, 2\pi]$.*

Then, control law (3.8), (3.20) ensures that attractor $\mathcal{A}$ in (3.7) is uniformly globally asymptotically stable along the arising closed-loop dynamics with (3.1).

Proof. *The proof is carried out by exploiting the following global version of [45, Prop. 7.5] (its proof is straightforward, taking $\mu \to \infty$ in the semiglobal version of [45, Prop. 7.5], and is actually therein implicitly used for establishing the result in [45, Ex. 7.6]).*

Proposition 3.2. *Given a nominally well-posed hybrid system $\mathcal{H}$, suppose that the compact set $\mathcal{A}$ in (3.7) is strongly forward invariant and globally uniformly attractive for $\mathcal{H}$. Then, it is uniformly globally asymptotically stable for $\mathcal{H}$.*

To apply Proposition 3.2 to our case, we first notice that the data of hybrid system (3.1), (3.8), (3.20) satisfy the hybrid basic conditions in [45, As. 6.5], therefore, from [45, Thm 6.8], it is nominally well-posed. Concerning forward invariance of $\mathcal{A}$ (namely, all solutions starting in $\mathcal{A}$ remain in $\mathcal{A}$ for all times), it follows from the fact that the flow dynamics of $\widehat{\varepsilon}$ is linear (so the origin is an equilibrium) and the jumps guarantee non-increase of $\widehat{\varepsilon}$ (see the proof of Theorem 3.1). Finally, global uniform convergence is a straightforward consequence of the stronger property of uniform finite-time convergence established in Lemma 3.1. □

Remark 3.2. *A desirable feature of the established global asymptotic stability of set $\mathcal{A}$ can be obtained by the robustness characterization given in [45, Ch. 7], which holds under the mild assumption that the hybrid dynamics satisfy the hybrid basic conditions (these are easily checked for dynamics (3.1), (3.8), (3.20)) and that the attractor is compact (this is easy to verify as well for set $\mathcal{A}$ in (3.7)). Robustness of asymptotic stability (established in [45, Thm 7.21]) allows to conclude that there exists a sufficiently small, but nonzero perturbation of the dynamics, for which the established nominal asymptotic stability is not destroyed. As a consequence, we expect our control law to perform well also under the presence of uncertainties, such as unmodeled dynamics, or external perturbations, as long as they are sufficiently small,*

and they are zero when the state belongs to the attractor (see, [45, Ch 7] for details). For more general settings, another useful feature arising from these robustness properties is that for stronger perturbations we have a semiglobal practical robust stability result, established in [45, Thm 7.20]. This result ensures that perturbations not vanishing in $\mathcal{A}$ lead to a gradual deterioration of the convergence properties, which is what one should expect when persistent disturbances, such as atmospheric drag or high solar activities or also measurement noise coming from the GNC devices affect the closed-loop dynamics. All these desirable properties are confirmed by our simulation results of Section 3.3. ⌟

3.2.3 Three-step finite-time control law

We will refer to the controller developed in this section as Controller C. The two controllers presented in the previous sections have the following features:

- Controller A is desirable because it forces the chaser to evolve along periodic (therefore bounded) motions, but does not lead to a convergence guarantee;
- Controller B is desirable because it guarantees finite time convergence, but these maneuvers are fragile since the chaser evolves on divergent trajectory until it reaches its goal. This can be unsafe in case of actuators failure.

In this section we combine the desirable features of the two above laws in a single enhanced control law following again a receding horizon paradigm, arising from the observation that we can separate our control design in two completely decoupled problems corresponding to the following partitions of vectors u and $\widehat{\varepsilon}$:

$$u = \begin{bmatrix} 0 \\ u_y \\ 0 \end{bmatrix} + \begin{bmatrix} 1 & 0 \\ 0 & 0 \\ 0 & 1 \end{bmatrix} u_{xz}, \quad u_y \in \mathbb{R},\ u_{xz} \in \mathbb{R}^2, \tag{3.21a}$$

$$\widehat{\varepsilon} = \begin{bmatrix} \widehat{\varepsilon}_y \\ \widehat{\varepsilon}_{xz} \\ \widehat{\varepsilon}_6 \end{bmatrix}, \quad \widehat{\varepsilon}_y \in \mathbb{R}^2,\ \widehat{\varepsilon}_{xz} \in \mathbb{R}^3,\ \widehat{\varepsilon}_6 \in \mathbb{R}. \tag{3.21b}$$

With this partition in mind, we may write the hybrid dynamics of state component $\widehat{\varepsilon}$ in (3.1) as follows:

$$\begin{cases} \widehat{\varepsilon}_y{}' = 0 \\ \widehat{\varepsilon}_{xz}{}' = (1-e)^{3/2} \begin{bmatrix} 1 \\ 0 \\ 0 \end{bmatrix} \widehat{\varepsilon}_6 \\ \widehat{\varepsilon}_6{}' = 0 \end{cases} \qquad (\widehat{\varepsilon}, \nu, \tau) \in \mathcal{C}, \tag{3.22a}$$

$$\begin{cases} \widehat{\varepsilon}_y^+ = \widehat{\varepsilon}_y + \widehat{B}_y(\nu) u_y \\ \begin{bmatrix} \widehat{\varepsilon}_{xz}^+ \\ \widehat{\varepsilon}_6^+ \end{bmatrix} = \begin{bmatrix} \widehat{\varepsilon}_{xz} \\ \widehat{\varepsilon}_6 \end{bmatrix} + \widehat{B}_{xz}(\nu) u_{xz} \end{cases} \qquad (\widehat{\varepsilon}, \nu, \tau) \in \mathcal{D}_u, \tag{3.22b}$$

where

$$\widehat{B}_y(\nu) := \frac{1}{k^2\rho}\begin{bmatrix} -s_\nu \\ c_\nu \end{bmatrix},$$
$$\widehat{B}_{xz}(\nu) := \frac{1}{k^2\rho(1-e^2)}\begin{bmatrix} -e(1+\rho)s_\nu - \frac{3\sigma\rho^2}{(1-e^2)^{3/2}} & \frac{3\sigma e\rho s_\nu}{(1-e^2)^{3/2}} - \rho^2 + \rho + 2 \\ (1-e^2)(1+\rho)s_\nu & (1-e^2)\rho c_\nu \\ (1+\rho)c_\nu + e & -\rho s_\nu \\ -3\rho^2 & 3e\rho s_\nu \end{bmatrix}. \tag{3.23}$$

Once the dynamics has been separated in two components, we may perform similar computations to (3.19) and obtain:

$$\widehat{\varepsilon}_y(\mu_2, j_2+1) = \tag{3.24}$$
$$\widehat{\varepsilon}_y(\mu_1, j_1) + \underbrace{\begin{bmatrix}\widehat{B}_y(\nu_1) & \widehat{B}_y(\nu_1+\overline{\nu})\end{bmatrix}}_{M_y(\nu_1,\overline{\nu}):=} \begin{bmatrix} u_y(\mu_1, j_1) \\ u_y(\mu_2, j_2)\end{bmatrix},$$

which is simpler than (3.19) because $\widehat{\varepsilon}_y$ remains constant along flowing solutions. The following result then parallels Conjecture 3.1 and Lemma 3.1.

Lemma 3.2. *Given any value of $\overline{\nu} \neq h\pi$, $h \in \mathbb{Z}$, matrix $M_y(\nu, \overline{\nu})$ is nonsingular for all $\nu \in [0, 2\pi]$. Moreover, for any such value of $\overline{\nu}$, selection:*

$$u_y := -\begin{bmatrix}1 & 0\end{bmatrix} M_y(\nu, \overline{\nu})^{-1}\widehat{\varepsilon}_y, \quad \gamma_\tau(\widehat{\varepsilon}_y, \nu) = \overline{\nu}, \tag{3.25}$$

guarantees that all solutions to (3.1), (3.21), (3.22) have the $\widehat{\varepsilon}_y$ component equal to zero after at most two jumps.

Proof. *Let us first compute:*

$$\begin{aligned}\det(M_y(\nu, \overline{\nu})) &= \frac{1}{k^2}\left(\frac{\sin(\nu)\cos(\nu+\overline{\nu})}{\rho(\nu)\rho(\nu+\overline{\nu})} + \frac{\sin(\nu+\overline{\nu})\cos(\nu)}{\rho(\nu)\rho(\nu+\overline{\nu})}\right) \\ &= \frac{\sin(\overline{\nu})}{k^2\rho(\nu)\rho(\nu+\overline{\nu})},\end{aligned}$$

which proves invertibility of $M_y(\nu, \overline{\nu})$ for all $\overline{\nu} \neq h\pi$, and all ν. The proof of finite-time convergence follows similar steps to the proof of Lemma 3.1, based on uniqueness of the solution of $\widehat{\varepsilon}_y(\mu_2, j_2+1) = 0$ in (3.24) and based on the fact that for any solution $\widehat{\varepsilon}_y$ with two consecutive impulses at (μ_1, j_1) and (μ_2, j_2), we have $\widehat{\varepsilon}_y(\mu_2, j_2) = \widehat{\varepsilon}_y(\mu_1, j_1+1)$, due to the trivial flow dynamics in (3.22a). □

Consider now state $\begin{bmatrix}\widehat{\varepsilon}_{xz} \\ \widehat{\varepsilon}_6\end{bmatrix}$ and input u_{xz}. To obtain periodic motion, from the structure of (3.22a) and because of Lemma 2.2, we want to select u_{xz} in such a way that any impulse brings the last component $\widehat{\varepsilon}_6$ of $\widehat{\varepsilon}$ to zero. To this end, paralleling (3.10a), and with reference to $\widehat{B}_{xz}$ in (3.23), define:

$$\widehat{b}_4(\nu) := \frac{3}{k^2(1-e^2)}\begin{bmatrix}-\rho \\ es_\nu\end{bmatrix}, \quad \widehat{B}_4^\perp(\nu) := \begin{bmatrix}\frac{es_\nu}{\rho} \\ 1\end{bmatrix}, \tag{3.26a}$$

and notice that we may obtain $\widehat{\varepsilon}_6^+ = 0$ with selection:

$$u_{xz} := -\frac{\widehat{b}_4(\nu)}{|\widehat{b}_4(\nu)|^2}\widehat{\varepsilon}_6 + \widehat{B}_4^{\perp}(\nu)v_{xz}, \tag{3.26b}$$

which mimics selection (3.10b), (3.14). The difference, as compared to before, is that we will now select v_{xz} in (3.26) following the receding horizon paradigm, which is here simplified because after any impulse, we obtain $\widehat{\varepsilon}_6^+ = 0$ and the solution $\widehat{\varepsilon}_{xz}$ remains constant along flows (see (3.22a)). Let us then introduce the reduced input matrix:

$$\widehat{B}_{xz}^r(\nu) := [\, I_3 \; 0 \,]\, \widehat{B}_{xz}(\nu)\widehat{B}_4^{\perp}(\nu) \tag{3.27}$$

$$= \frac{1}{k^2\rho^2}\begin{bmatrix} 2 + ec_\nu & 2e + c_\nu(1+e^2) & -s_\nu \end{bmatrix}^\top, \tag{3.28}$$

and notice that we need at least three impulses to drive $\widehat{\varepsilon}_{xz}$ to zero. Let us use $\widehat{\varepsilon}_6^+ = 0$ and the arising zero right-hand side of (3.22a) to obtain that three consecutive impulses with selection (3.26) lead to (compare to (3.24)):

$$\widehat{\varepsilon}_{xz}(\mu_3, j_3 + 1) = \widehat{\varepsilon}_{xz}(\mu_1, j_1) + \tag{3.29}$$

$$\underbrace{\begin{bmatrix} \widehat{B}_{xz}^r(\nu_1) & \widehat{B}_{xz}^r(\nu_1 + \overline{\nu}_1) & \widehat{B}_{xz}^r(\nu_1 + \overline{\nu}_1 + \overline{\nu}_2) \end{bmatrix}}_{M_{xz}(\nu_1, \overline{\nu}_1, \overline{\nu}_2) :=} \begin{bmatrix} v_{xz}(\mu_1, j_1) \\ v_{xz}(\mu_2, j_2) \\ v_{xz}(\mu_3, j_3) \end{bmatrix},$$

where $\overline{\nu}_1 = \nu(\mu_2, j_2) - \nu(\mu_1, j_1)$ and $\overline{\nu}_2 = \nu(\mu_3, j_3) - \nu(\mu_2, j_2)$ are the free motions durations between each pair of consecutive impulses. The following result then parallels Lemma 3.2.

Lemma 3.3. *Given any values of $\overline{\nu}_1$, $\overline{\nu}_2$ such that*

$$\overline{\nu}_1 \neq 2h\pi, \quad \overline{\nu}_2 \neq 2h\pi, \quad \overline{\nu}_1 + \overline{\nu}_2 \neq 2h\pi, \quad \forall h \in \mathbb{Z}, \tag{3.30}$$

matrix $M_{xz}(\nu, \overline{\nu}_1, \overline{\nu}_2)$ is nonsingular for all $\nu \in [0, 2\pi]$. Moreover, selecting any value of $\overline{\nu}_1 = \overline{\nu}_2 = \overline{\nu}$, selection:

$$v_{xz} := -[\, 1\, 0\, 0 \,]\, M_{xz}(\nu, \overline{\nu}, \overline{\nu})^{-1}\widehat{\varepsilon}_{xz}, \quad \gamma_\tau(\widehat{\varepsilon}_{xz}, \nu) = \overline{\nu}, \tag{3.31}$$

guarantees that all solutions to (3.1), (3.21), (3.22), (3.26) have the $\widehat{\varepsilon}_{xz}$, $\widehat{\varepsilon}_6$ components equal to zero after at most three jumps.

Proof. *First consider the following expression that emerges from direct computation:*

$$\begin{aligned} d_M &:= \det(M_{xz}(\nu, \overline{\nu}_1, \overline{\nu}_2)) \\ &= 2\frac{\sin(\overline{\nu}_1) + \sin(\overline{\nu}_2) - \sin(\overline{\nu}_1 + \overline{\nu}_2)}{\rho(\nu)^2\rho(\nu + \overline{\nu}_1)^2\rho(\nu + \overline{\nu}_1 + \overline{\nu}_2)^2}. \end{aligned} \tag{3.32}$$

since ρ never vanishes we may study the invertibility of M_{xz} by only focusing on the numerator, which satisfies:

$$\begin{aligned} d_M^n &= \sin(\overline{\nu}_1) + \sin(\overline{\nu}_2) - \sin(\overline{\nu}_1 + \overline{\nu}_2) \\ &= \sin(\overline{\nu}_1)(1 - \cos(\overline{\nu}_2)) + \sin(\overline{\nu}_2)(1 - \cos(\overline{\nu}_1)) \\ &= 4\sin\left(\frac{\overline{\nu}_1}{2}\right)\sin\left(\frac{\overline{\nu}_2}{2}\right)\sin\left(\frac{\overline{\nu}_1}{2} + \frac{\overline{\nu}_2}{2}\right) \end{aligned} \tag{3.33}$$

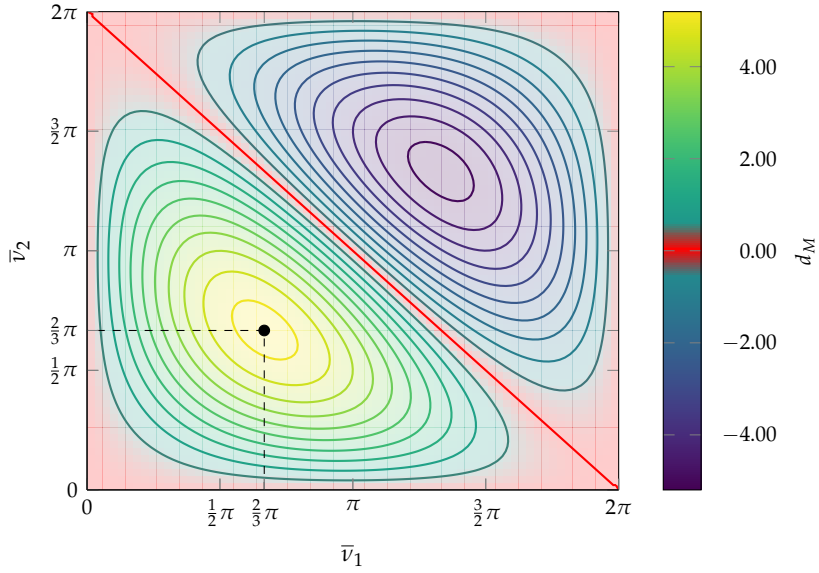

Figure 3.2: Level sets for $\det(M_{xz}(\nu, \overline{\nu}_1, \overline{\nu}_2))$ with $e = 0$.

and which clearly does not vanish if and only if (3.30) *holds, regardless the value of* ν.

The fact that with controller (3.31) *all solutions have* $\widehat{\varepsilon}_{xz}$, $\widehat{\varepsilon}_6$ *converge to zero in finite time follows similar steps to the proof of Lemma* 3.2*, from uniqueness of* v_{xz} *in* (3.31). □

The following result can be established by similar derivations to those in the proof of Theorem 3.2, relying on the uniform finite-time convergence established in Lemmas 3.2 and 3.3. Its proof is omitted due to this similarity to that of Theorem 3.2.

Theorem 3.3. *Control law* (3.21), (3.25), (3.26b), (3.31) *ensures that attractor* $\mathcal{A}$ *in* (3.7) *is uniformly globally asymptotically stable along the closed-loop dynamics with* (3.1).

Figure 3.2 shows the level sets of $\det(M_{xz}(\nu, \overline{\nu}_1, \overline{\nu}_2))$ for a circular orbit, i.e. $e = 0$, which clearly indicates that the determinant is maximized with $\overline{\nu}_1 \approx \overline{\nu}_2 \approx 120°$. Due to this fact and to reduce consumption, we select this value for $\overline{\nu}_1 = \overline{\nu}_2$ in our simulation section.

Remark 3.3. *The three control laws proposed in this chapter require estimates of relative positions and velocities of the follower. During proximity operations, far range and close range rendezvous operations, relative measurements of positions and velocities between the leader and the follower may be provided either by passive or active sensors data processed by the navigation system of the follower (e.g. vision-based relative pose estimation, filtered Carrier-phase Differential GPS) [38]. Note that the impact of the sensors noise and the robustness of the hybrid schemes are analyzed numerically in the*

simulation section and are expected to be non-damageful for the asymptotically stable closed loops in light of the robustness results highlighted in Remark 3.2. ⌟

3.3 SIMULATIONS

In this section, we present the simulation results obtained with the control laws designed in Section 3.2 and system (3.1) (equivalently (3.3)–(3.5)) using a nonlinear simulator and comparing the results with a linearized model in *Matlab-Simulink* for the PRISMA mission [19].

3.3.1 Simulated context and performance metrics

The simulator is composed by two main blocks: the controller and the dynamics. The controller recovers the current state in LVLH coordinates and transforms it into state $\widehat{\xi}$ to compute the mismatch (2.44). Afterwards, the control input u is computed, to be applied to the dynamics block.

For a given orbital rendezvous scenario, the output of the nonlinear simulator is the history of the relative position and velocity between the two spacecrafts, obtained by simulating their inertial trajectories in the Earth-centered frame via the integration of the Gauss equations. The simulator accounts for the disturbances provoked by the Earth's oblatness (so-called J_2-effect) and the atmospheric drag. Moreover, uncertainties that originate from GNC devices (measurement noise and chemical thrusters limitations) are also simulated. For instance, the measured relative state is affected by a white noise characterised by the following standard deviation on the relative position and velocity: $d_p = 10^{-2}$ m, $d_v = 10^{-5}$ m/s (see Remark 3.3). Then, the applied control u is obtained from the computed control u^* through the thrusters saturation and dead-zone filter along each axis independently:

$$u_i = \begin{cases} u_i^* \text{ if } u_i^* \in [-\Delta v_{max} \ -\Delta v_{min}] \cup [\Delta v_{min} \ \Delta v_{max}], \\ 0 \text{ if } u_i^* \in [-\Delta v_{min} \ \Delta v_{min}], \\ \dfrac{u_i^*}{|u_i^*|}\Delta v_{max} \text{ if } u_i^* \in (-\infty \ -\Delta v_{max}] \cup [\Delta v_{max} \ \infty), \end{cases} \tag{3.34}$$

with $\Delta v_{max} = 0.5$ m/s and $\Delta v_{min} = 5 \cdot 10^{-4}$ m/s. This simulation set-up is a simple way to check the robustness properties of hybrid schemes mentioned in Remark 3.2. Aside, a linearized dynamics with no environment disturbances nor devices uncertainties is also propagated along with the different controllers for the sake of comparison.

Within the PRISMA mission, the leader vehicle evolves on a given orbit with a semi-major axis of 7011 km, an eccentricity of $e = 0.004$ and an inclination of $i = 98$ deg. The performed simulations are run from the initial true anomaly $\nu_0 = 0$ up to a final true anomaly $\nu_f = \nu_0 + 20\pi$, namely ten orbital periods later. The chaser satellite begins the rendezvous maneuver at initial state X_0 at

$\nu_0 = 0$. The simulations aim at stabilizing the chaser in a periodic trajectory specified by a suitable selection of $\widehat{\xi}^{\,ref}$ in (2.43):

$$\widehat{\xi}^{\,ref} = (7.68,\ 17.68,\ 87.78,\ 33.04,\ -15.77,\ 0) \tag{3.35}$$

where we emphasize that the last element is zero (a necessary and sufficient condition for periodic motion, as established in Lemma 2.2). The reference periodic trajectory $\widehat{\xi}^{\,ref}$ is free to evolve inside a tolerance box $\mathcal{B}$, centered at point $X_{\mathcal{B}} = (100,\ 0,\ 0)$m (expressed in the target's position frame used in (2.1)) and has positive and negative widths $X_{tol} = (50,\ 25,\ 25)$m in the three LVLH directions.The different control thrusts are separated by an angular distance $\overline{\nu} = 120^{\circ}$ from one to another along the whole duration of the rendezvous. This value of $\overline{\nu}$ has been selected in order to maximize the norm of the determinant of matrix M either from (3.19) or (3.29) depending on the selected control law (see Figures 3.1 and 3.2). Doing this, the consumption is expected to be reduced as the control input is computed through the inversion of M.

For each one of the three control laws in Section 3.2, four different initial conditions X_{0i}, $i \in \{1, \cdots, 4\}$ for state $X(t)$ in (2.1) have been used, which are chosen at four different distances from the target satellite located at the origin of the LVLH frame:

$$\begin{aligned} &|X_{01}| \approx 500,\ \text{m} && |X_{02}| \approx 750,\ \text{m} \\ &|X_{03}| \approx 2000,\ \text{m} && |X_{04}| \approx 5200\ \text{m}. \end{aligned}$$

The first to initial conditions X_{01} and X_{02} correspond to a close range rendezvous scenario, while the last to X_{03} and X_{04} to a far range rendezvous scenario.

The initial conditions are selected as:

$$\begin{aligned} X_{01} &= (400,\ 300,\ -40,\ 0,\ 0,\ 0), \\ X_{02} &= (600,\ 400,\ 200,\ 0,\ 0,\ 0), \\ X_{03} &= (-1500,\ 1300,\ 150,\ 0,\ 0,\ 0), \\ X_{04} &= (5000,\ 1300,\ 500,\ 0,\ 0,\ 0), \end{aligned} \tag{3.36}$$

where the first three components are meters and the last three are meters per second. Let us denote by $\widehat{\xi}_{0i}$ the image of the initial states X_{0i} through $R(\nu)$ defined in (2.41). The initial relative velocity has been selected to be zero to account for the fact that the starting point of our trajectory may be a holding point arising from a previous station keeping along the space mission.

Two performance indexes are considered: the fuel consumption J, and the convergence time T_c, both described next.

The fuel consumption is characterized in [89], when firing is achieved by 6 identical thrusters rigidly mounted to the satellite, and corresponds to the cost function:

$$J := \sum_{\nu_k \in \mathcal{V}} \|u(\nu_k)\|_1, \tag{3.37}$$

where $u = \Delta v$ has been introduced in (2.5), (2.7), $\mathcal{V}$ is the set of firing instants, and $|\cdot|_1$ denotes the 1-norm, so that $\|\Delta v(\nu_k)\|_1 = |\Delta v_x(\nu_k)| + |\Delta v_y(\nu_k)| +$

$|\Delta v_z(\nu_k)|$. The convergence is evaluated by means of the mismatch ratio η given by

$$\eta(\nu) = \frac{\|\widehat{\varepsilon}(\nu)\|_2}{\|\widehat{\varepsilon}(\nu_0)\|_2} = \frac{\|\widehat{\xi}(\nu) - \widehat{\xi}^{\,ref}\|_2}{\|\widehat{\xi}(\nu_0) - \widehat{\xi}^{\,ref}\|_2} \tag{3.38}$$

The convergence time T_c is defined as the smallest time after which the solution remains in the δ vicinity of the reference point, namely:

$$\eta(\nu) \leq \delta, \quad \forall\, \nu \geq T_c \tag{3.39}$$

where δ is set to 5%.

3.3.2 Comparative simulation results

Different simulations have been performed for each one of the three control laws in Section 3.2, and for each one of the initial conditions in (3.36). The trajectories concerning the initial condition X_{01} for the three controllers are represented in Figure 3.3 at page 41. The corresponding applied impulses and the corresponding convergence profile are represented in Figure 3.4 at page 42. The trajectories from the other initial conditions have not been included for sake of brevity, while in Figure 3.5 at page 43 we reported the applied impulses and the convergence profile in the case of the initial condition X_{04}, the one with the largest initial error.

In the following study, we first address the results of the linear simulations in order to analyze the nominal behavior of the different controllers. Then, we focus on the nonlinear simulation to assess their robustness with respect to modeling errors, navigation uncertainties and input saturation. Finally, for the sake of comparison, we report on the simulation results obtained with the MPC controller proposed in [9], whose results are depicted in Figure 3.6 at page 44.

LINEAR SIMULATIONS Figures 3.4a, 3.4b and 3.4c reveal how the different control strategies steer the chaser to the tolerance box along different paths in a linear environment. Controller A makes the chaser inch to the tolerance box while controllers B and C have more "straight" paths. These facts are corroborated by the impulsive control plan on the upper graphs of Figures 3.4a, 3.4b and 3.4c. Controllers B and C concentrate most of their consumption on the two first controls while the 7 first controls have a relative importance for Controller A.

The differences among the control strategies can also be observed on the evolution of η the mismatch ratio (lower graphs of Figures 3.4a, 3.4b and 3.4c). Thanks to the safe orbit transfer philosophy (maintaining $\widehat{\xi}_6$ to zero which ensures, by Lemma 2.2, intermediate periodic motions), the Controllers A and C make the tracking trajectory jump from a periodic orbit to another so that $\widehat{\xi}$ and $\widehat{\varepsilon}$ remain constant between control impulses. On the contrary, Controller C allows to follow a path possibly with a high divergence coefficient $\widehat{\xi}_6$, so that the error norm can possibly evolve fast (either diverging or converging) between successive firing times. Indeed, in the linear simulation, Controller B provides

faster convergence time, compared to Controllers A and C, with an equivalent consumption. In fact, in an ideal context, only two impulses are needed to bring the chaser to the steady state, while Controllers A and C need at least three impulsive controls. On the other hand, if Controller A is the slowest in the linear simulator, it is generally the less demanding in terms of consumption among the hybrid controllers, as expected.

NONLINEAR SIMULATIONS Addressing the nonlinear simulations, two cases can be distinguished depending on how close to the target relative orbit the chaser starts. For the close range control maneuvers (starting from initial conditions X_{01}) illustrated in Figures 3.3 and 3.4, the difference between the linear and nonlinear simulations are slight: the consumption and the convergence time are equivalent, as one can notice from the first rows of Tables 3.1 and 3.2. It can also be observed on Figure 3.4 that no controls are saturated: the feedback control is properly executed in close range in the nonlinear simulation. However, the trajectories have small differences that can be imputed to the dynamics linearization process and navigation uncertainties. Analyzing the simulations starting from the initial states X_{02}, the same kind of conclusions can be drawn. Note that for Controllers A and C, the control inputs are slightly saturated but not enough to degrade the performances in terms of convergence time.

On the contrary the simulations from the initial states X_{03} and X_{04} expose different behaviors. Due to the larger distance from the target box, every controllers demand for a first large impulsive control action. However, it can be observed on Figure 3.5 that all the first impulses are saturated in the nonlinear simulator. Each controller reacts in a different manner to such a drawback. Controller B fails to stabilize the chaser in the presence of saturations for initial states X_{03} and X_{04}. In fact, the size of input $u = \Delta v$ (see (2.5) and (2.7)) demanded by the controller is largely beyond the thrusters capabilities, while such an amount is supposed to steer the chaser to the box after two impulses. Instead, since the impulsive controls are truncated, the chaser is brought on a random orbit with no particular interest and obviously divergent (see Figure 3.5b). On the contrary, for Controllers A and C, a part of the control is dedicated to guiding the chaser to the set of periodic orbits. Thus, even if this control is truncated, the chaser is steered to states with gradually decreasing divergence parameter $\widehat{\xi}_6$. This fact can be observed on Figures 3.5a and 3.5c, where the slope of the error norm decreases after each impulsive control and tends to zero. Both controllers expose two phases: first stabilizing $\widehat{\xi}_6$ and then steering states ξ_1 to ξ_5 to ξ^{ref}. The consequence is that the convergence time is degraded for both controllers. Naturally, the presence of saturation limits the consumption for both controllers, as compared to the linear simulations. Indeed Controllers A and C show some robustness abilities with respect to saturation at the price of a slower convergence time.

COMPARISON WITH MPC STRATEGY Parallel simulations have been performed with the MPC-based method recently presented in [9], which directly addresses the minimization of J and accounts for saturation. This controller has

been benchmarked using the nonlinear simulator. For the sake of comparison, we report on the controlled trajectory for the initial condition X_{01}, shown in Figure 3.6a, and the applied impulses as well as the profile of η, shown in Figures 3.6b and 3.6c for the initial conditions X_{01} and X_{04}. Note that in the MPC framework η refers to the relative distance from the set of the relative periodic orbits included in the tolerance box (see [35] for a rigorous description of this set) including the relative orbit ξ^{ref}.

For the close range initial conditions (X_{01} and X_{02}), the hybrid controllers ensure faster convergence of the chaser as compared to the MPC controller. This can be explained by two facts. First, it has been mentioned earlier that, for those initial conditions, the behavior of the hybrid controllers is equivalent between the nonlinear and the linear simulator, probably due to the fact that saturation does not play a dominant role. Second, the convergence and stability properties of the hybrid controllers probably justifies the faster convergence as compared to the MPC controller from [9], which lacks a guarantee of asymptotic stability.

For the far range initial conditions X_{03} and X_{04}, the performance of the hybrid controllers are degraded probably because of the saturations. Conversely the MPC controller, which explicitly takes into account the presence of saturations, exhibits a better behavior for far range initial conditions. Finally, the MPC controller leads to smaller consumption at the price of a significantly higher numerical complexity (a numerical optimization must be solved at each firing instant).

Initial condition	Control A		Control B		Control C		MPC
	LIN	NL	LIN	NL	LIN	NL	NL
X_{01}	1.00	1.10	0.86	1.10	0.93	1.02	0.57
X_{02}	1.92	1.92	2.18	2.19	2.85	2.40	1.37
X_{03}	4.50	3.77	4.44	$\times\times\times$	4.00	4.12	2.17
X_{04}	9.05	8.96	9.23	$\times\times\times$	9.35	8.16	7.11

Table 3.1: Consumption J $\left[\frac{\mathrm{m}}{\mathrm{s}}\right]$.

Initial condition	Control A		Control B		Control C		MPC
	LIN	NL	LIN	NL	LIN	NL	NL
X_{01}	2.91	2.86	0.34	0.34	0.98	0.97	1.63
X_{02}	2.59	2.59	0.34	0.34	0.98	0.98	1.34
X_{03}	3.55	2.91	0.34	$\times\times\times$	0.98	1.94	1.64
X_{04}	3.87	5.48	0.33	$\times\times\times$	0.98	4.20	2.97

Table 3.2: Convergence time T_c [numer of orbits].

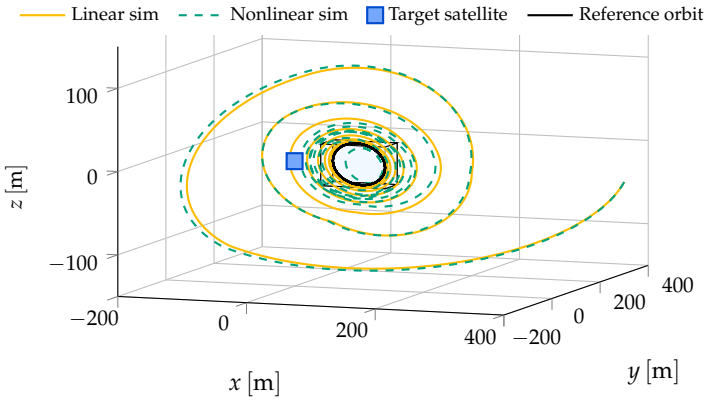

(a) Trajectories for Controller A when starting from X_{01}.

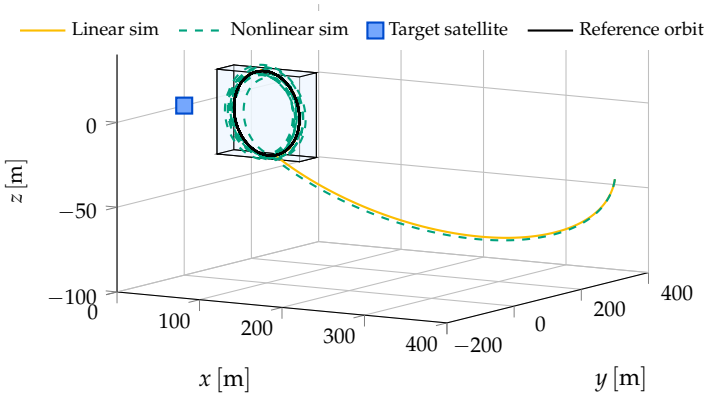

(b) Trajectories for Controller B when starting from X_{01}.

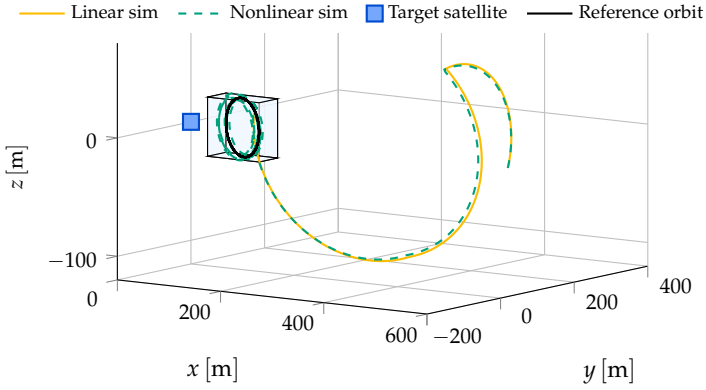

(c) Trajectories for Controller C when starting from X_{01}.

Figure 3.3: Trajectories for Controllers A, B, and C when starting from X_{01}.

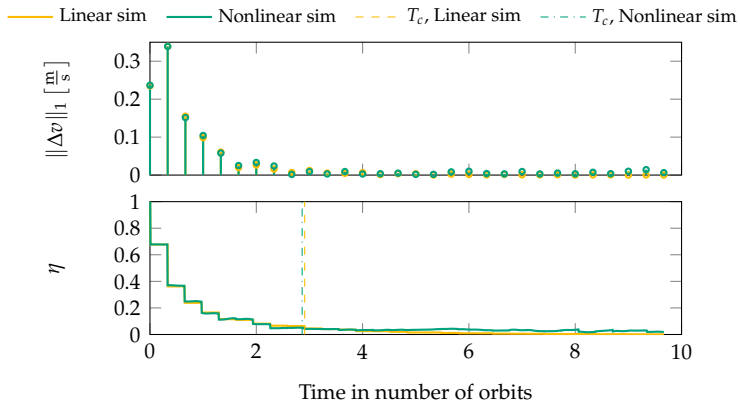

(a) Impulses and convergence from X_{01} for Controller A.

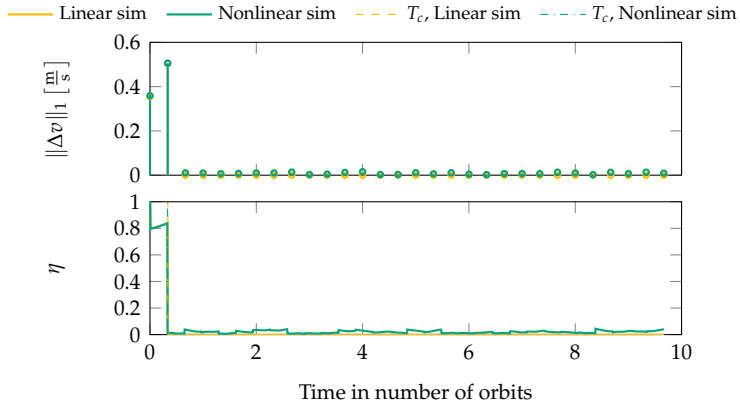

(b) Impulses and convergence from X_{01} for Controller B.

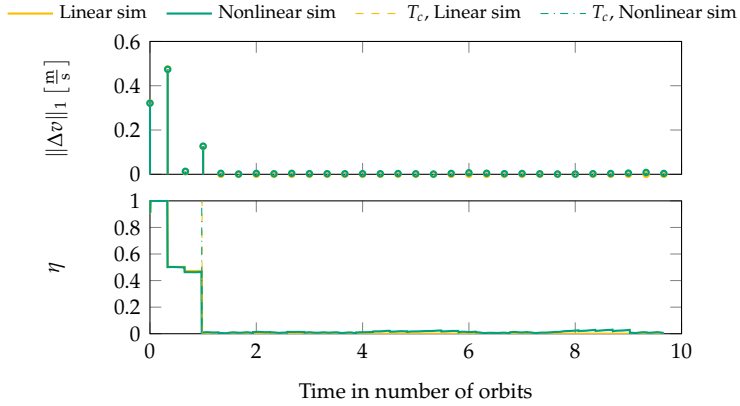

(c) Impulses and convergence from X_{01} for Controller C.

Figure 3.4: Impulses and convergence from X_{01} for Controllers A, B, and C.

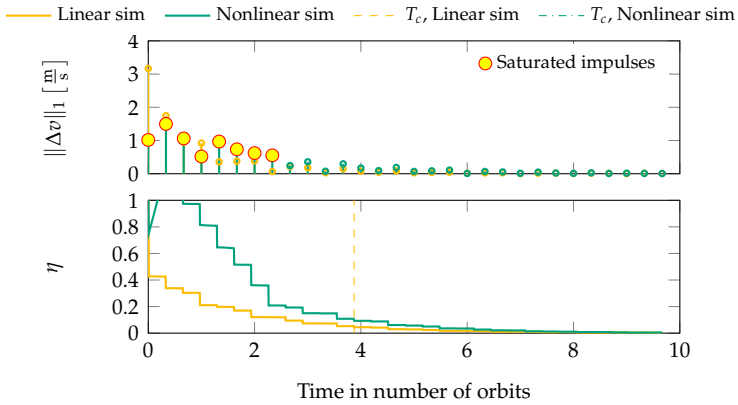

(a) Impulses and convergence from X_{04} for Controller A.

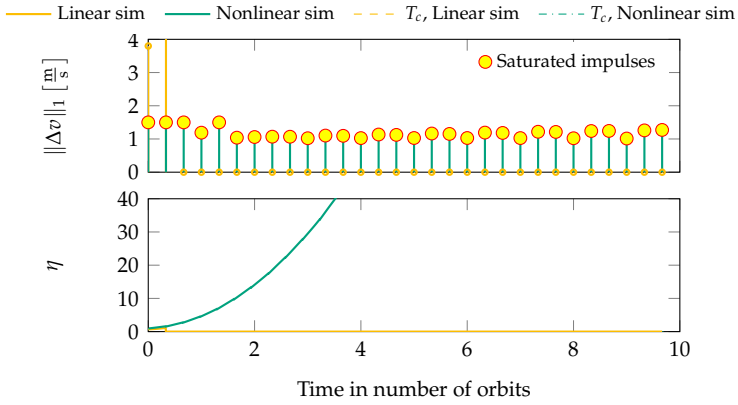

(b) Impulses and convergence from X_{04} for Controller B.

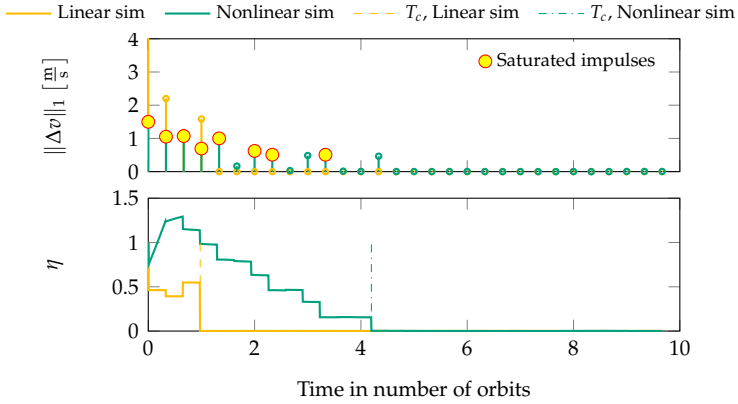

(c) Impulses and convergence from X_{04} for Controller C.

Figure 3.5: Impulses and convergence from X_{04} for Controllers A, B, and C.

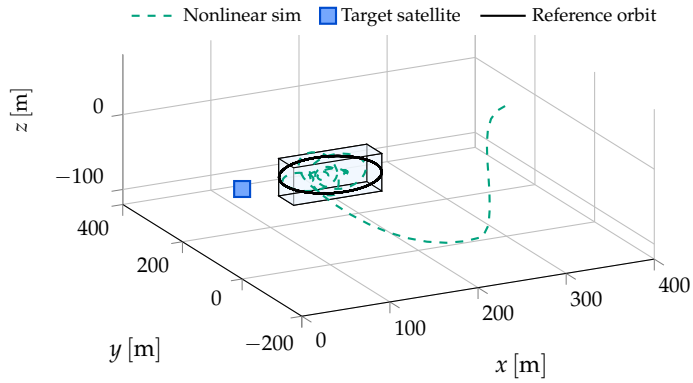

(a) Trajectory for the MPC controller when starting from X_{01}.

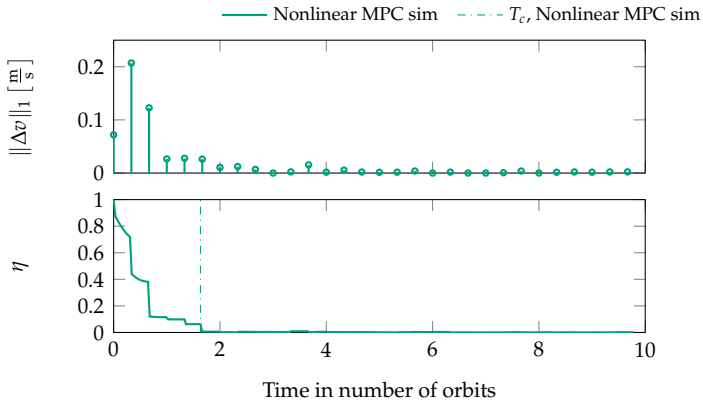

(b) Impulses and convergence from X_{01} for the MPC controller.

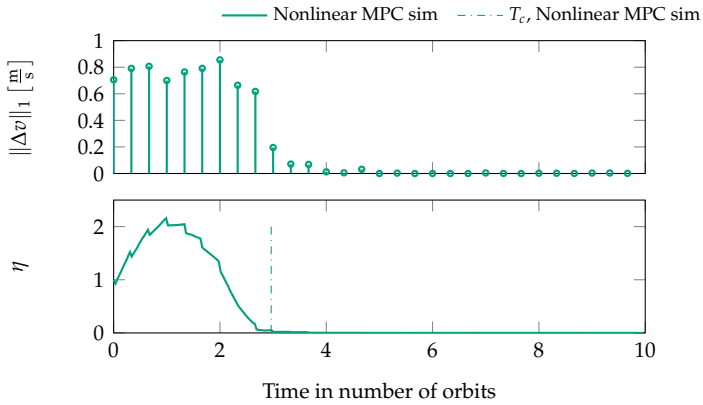

(c) Impulses and convergence from X_{04} for the MPC controller.

Figure 3.6: Comparative simulations using the MPC controller of [9]

Part II

ROBUST TIME SUB-OPTIMAL CONTROLLER

4 ROBUST TIME-SUB-OPTIMAL CONTROL FOR A CLASS OF SATURATED LINEAR PLANTS

This chapter illustrates a novel Robust Time-Sub-Optimal (RTSO) control framework for a class of linear SISO systems with saturated input, based on a hybrid blend of a local and a global controller. The scheme makes use of two hysteresis mechanisms in order to provide robustness to unmodelled dynamics and measurement noise. Rigorous certificates of the stability of the proposed controller are given for the saturated double integrator, by exploiting the properties of hybrid dynamical systems established in [44], [45], and other recent related work by Rafal Goebel, Ricardo G. Sanfelice, and Andrew R. Teel. This chapter is based on the published work [21] and on some more recent advancements.

4.1 INTRODUCTION: MOTIVATION AND APPROACH

Chains of integrators with saturated input are fundamental dynamical processes. The control of them is widely investigated by the control community, see, for example, [99] and [77]. Among many control strategies, time-optimal controllers are capable of achieving finite time stabilization of such plants in minimum time, see for example [40], [16].

Time-optimal control with bounded controls is well-known to yield bang-bang and hence discontinuous open-loop and feedback controls [10]. A classical example of this is the second-order integrator $\dot{x}_1 = u$, $\dot{x}_2 = x_1$, with $u \in [-1, 1]$, which is one of the most fundamental systems in control applications, and has many mechatronic applications [25] [57]. There, the time-optimal feedback that drives the states to the origin takes on the value -1 above the curve $x_2 = \text{sign}(x_1)\, x_1^2/2$, and the value 1 below that curve, and is thus discontinuous along that curve. Open-loop controls switch from one value of the control to its negative upon reaching this "switching curve". The computation of the curve, thanks to the Pontryagin Maximum Principle, boils down to backward integration of the optimal dynamics, and the same idea applies to higher-order integrators. More advanced methods, for example Groebner bases, have been tested in computation of the switching surfaces for the third-order integrator [102] and can be used for more involved linear dynamics [79].

The discontinuity of the time-optimal feedback raises the issue of its robustness. Essentially, the discontinuity, measurement error and/or unmodelled dynamics may lead to frequent switching/chattering and loss of performance. One early proposal to deal with this [75], for the second-order integrator, in-

volves smoothing of the bang-bang behavior along the switching curve and linear control near the origin, resulting in sub-optimal behavior. Similarly, replacing the switching curve and the two regions, above and below it, by three regions has been considered in discrete-time [57] and applied to disk-drive control. Similar ideas are followed for the third-order integrator in [77], [78]. Alternatively, some robustness can be introduced through hysteresis [47], thus suggesting a hybrid formulation of the feedback. For a related discussion of robustness aspects of time-optimal and other stabilizing controllers for the second-order integrator, see [87].

This work builds on the ideas considered before, like hysteresis implementation of the switching surface and use of linear feedback near the origin, and, for a class of linear systems, formulates a sub-time-optimal feedback in the hybrid dynamical systems framework of [45]. The use of hybrid controllers for improving performances of continuous time plants has been already investigated for example in [65] and, for reset control systems, in [74]. One advantage of using this framework is that it easily allows for modeling of hysteresis-type switching of various controllers, for example a local (in this case, linear) and a global one; see [45] and, for example, [82]. The resulting model is, in fact, simpler than one resulting from continuous interpolation of the original discontinuous feedback. Another advantage is that robustness of asymptotic stability follows from the general results in [45], if the data meets the mild regularity conditions (the functions modeling the feedback are continuous, and the set where different functions apply are closed) already introduced in Assumption 1.1.

4.2 TIME OPTIMAL SWITCHING SURFACES

The class of SISO LTI processes with bounded input for which the robust time-sub-optimal controller is developed can be parametrized by the following dynamics with state $z = (z_1, z_2, \ldots, z_n) \in \mathbb{R}^n$

$$\dot{z} = \begin{bmatrix} \dot{z}_1 \\ \dot{z}_2 \\ \vdots \\ \dot{z}_n \end{bmatrix} = \begin{bmatrix} -a z_1 + q \\ z_1 \\ \vdots \\ z_{n-1} \end{bmatrix} =: \bar{A}\, z + \bar{b}\, q\,, \tag{4.1a}$$

for a suitable state matrix $\bar{A} \in \mathbb{R}^{n\times n}$ and input vector $\bar{b} \in \mathbb{R}^n$, together with bounded input q:

$$q \in [-1,\, 1]\,, \tag{4.1b}$$

and parameter

$$a \in \mathbb{R}_{\geq 0}\,. \tag{4.1c}$$

This system represents a chain of n integrators if $a = 0$, while if $a > 0$ the first element of the chain has a real negative eigenvalue. In both cases we consider $n \in \{1, 2, 3\}$. In this work, we do not consider dynamical systems

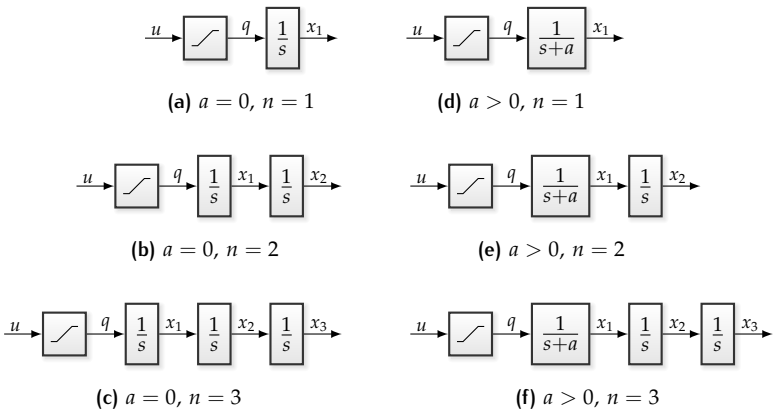

Figure 4.1: Block diagram representation of the systems generated by (4.1).

with order higher than 3 due to the lack of easy-to-compute and closed-form time optimal switching surface for such higher order systems. Never the less, considering dynamical order up to 3 covers many of the technological scenarios. In Figure 4.1 the systems generated from equation (4.1) are depicted in a block diagram representation.

Remark 4.1. *Matrix $\bar{A}$ in (4.1) has n eigenvalues in $\{-a, 0, \ldots, 0\}$, therefore it has only real and non-positive eigenvalues.* ⌟

In order to develop the RTSO controller, the time-optimal control law for the class of systems described by (4.1) has to be studied. In particular, from general optimal control theory, the following theorem can be stated:

Theorem 4.1. *From [58, Theorem 5.4], system (4.1) has a unique time-optimal control, which is bang-bang (i.e., it takes only the extreme values) and switches at most $(n-1)$ times.*

Remark 4.2. *Theorem 4.1 holds because system (4.1) is an LTI system whose dynamics matrix $\bar{A}$ has only real and non positive eigenvalues.* ⌟

For the computation of the time-optimal controller, we rely on an auxiliary state x arising from a similarity transformation

$$x := Sz\,, \tag{4.2a}$$

which transforms system (4.1) to

$$\dot{x} = Ax + bq \tag{4.2b}$$

with

$$\begin{aligned} A &:= S\bar{A}S^{-1}\,, \\ b &:= S\bar{b}\,. \end{aligned} \tag{4.2c}$$

For the auxiliary system (4.2) with, $n \in \{1, 2, 3\}$, it is possible to express the time-optimal controller as a feedback law trough a function φ_n depending from the auxiliary state x. This function will be called time-optimal switching function or time-optimal switching surface, since the set $\{x|\varphi_n(x) = 0\}$ represents a hypersurface in the x state space.

The process of computing such a time-optimal switching function is well known, and is covered in classical optimal control books such as [10] and [58]. It is essentially based on integrating backward in time the dynamics, taking into account a control q that toggles $(n-1)$ times between the extreme values (see Theorem 4.1).

The above mentioned set $\{x|\varphi_n(x) = 0\}$ has the peculiarity of splitting the state space in two halves, to which we will refer as set $\mathcal{U}_+$ and set $\mathcal{U}_-$, where the time-optimal control law is perfectly known. In particular consider the following Proposition.

Proposition 4.1. *Let us define the following sets:*

$$\begin{aligned} \mathcal{U}_+ &:= \{x|\varphi_n(x) > 0\} \\ \mathcal{U}_- &:= \{x|\varphi_n(x) < 0\} \end{aligned} \tag{4.3a}$$

Then, given a generic initial condition x_0 for system (4.2), $x_0 \in \mathcal{U}_+$ (respectively, $x_0 \in \mathcal{U}_-$) implies that the time-optimal control takes the value $q = -1$ (respectively, $q = 1$) for an initial time interval of non zero length. Moreover, it holds that $\mathcal{U}_+ \cap \mathcal{U}_- = \varnothing$ and

$$\overline{\mathcal{U}_+ \cup \mathcal{U}_-} = \mathbb{R}^n \tag{4.3b}$$

We now start covering the illustration of the switching functions for the considered class of systems described by (4.1).

4.2.1 Poles at the origin

In this case, we take the auxiliary state x in (4.2) to be the original state z, that is, we consider a trivial similarity transformation.

$$x = z\,. \tag{4.4}$$

Moreover, for the case of poles in the origin, $a = 0$ holds.

SINGLE INTEGRATOR Start considering system (4.2) (or, equivalently in this case, (4.1)) with $n = 1$. The trivial time-optimal switching surface for the first order case corresponds to

$$\varphi_1(x) := x_1\,. \tag{4.5}$$

DOUBLE INTEGRATOR Consider now system (4.1) with $n = 2$, $a = 0$. This system is known as "saturated double integrator", and its time-optimal control with saturated input is well known and studied, see, among others, [10, 58, 86]. Nevertheless, for this case and for the sake of illustration, we report here the

procedure followed for computing the time-optimal switching surface, which is the same followed for the other covered cases. Consider therefore the double integrator dynamics deriving from (4.1) with $n = 2$, $a = 0$:

$$\begin{aligned} \dot{x}_1 &= q\,, \\ \dot{x}_2 &= x_1\,. \end{aligned} \tag{4.6}$$

As mentioned before, the procedure for deriving the time-optimal switching surface is based on integrating backward in time the dynamics, taking into account a control q that toggles $(n-1)$ times (one time for the analyzed case) between the extreme values. We therefore proceed in backward integrating the dynamics for a time $t = t_1 \geq 0$ (that will correspond to the toggling time of q):

$$x(t_1) = \begin{cases} \left(-t_1,\ \frac{t_1^2}{2}\right) & \text{if } q = 1 \\ \left(t_1,\ -\frac{t_1^2}{2}\right) & \text{if } q = -1 \end{cases} \tag{4.7}$$

Exploiting the fact that $t_1 \geq 0$, we can re-parameterizing this trajectories in terms of the state x as follows for deriving the time optimal switching curve:

$$\varphi_2(x) = \begin{cases} x_2 - \frac{x_1^2}{2} & \text{if } x_1 \geq 0 \\ x_2 + \frac{x_1^2}{2} & \text{if } x_1 \leq 0\,. \end{cases} \tag{4.8}$$

We recognize that the just derived switching surface $\varphi_2(x)$ depends by the lower order switching surface $\varphi_1(x) = x_1$ as follows

$$\varphi_2(x) := x_2 + \operatorname{sign}\left(\varphi_1(x_1)\right) \frac{x_1^2}{2}\,. \tag{4.9}$$

This last equation represents the time-optimal switching surface for the saturated double integrator. The following switching surfaces are derived following the same presented procedure.

TRIPLE INTEGRATOR Consider finally system (4.1) with $n = 3$. This case is the most involved one, but the explicit representation of its time-optimal switching surface is still known, see for example [37] and [77], and may be written as:

$$\begin{aligned} \varphi_3(x) :=& x_3 + \frac{x_1^3}{3} + \\ &+ \operatorname{sign}\left(\varphi_2(\left[\begin{smallmatrix} x_1 \\ x_2 \end{smallmatrix}\right])\right) \left(x_1 x_2 + \left(\frac{x_1^2}{2} + \operatorname{sign}\left(\varphi_2(\left[\begin{smallmatrix} x_1 \\ x_2 \end{smallmatrix}\right])\right) x_2 \right)^{\frac{3}{2}} \right)\,. \end{aligned} \tag{4.10}$$

It is interesting to observe how the presented time-optimal switching functions exhibit a nested structure. Indeed the n-th order surface can be written as a function of the $(n-1)$-th order surface.We will see that this peculiarity arises for the case with $a > 0$ as well.

4.2.2 One negative pole plus poles at the origin

Consider now the case of system (4.1) with $a > 0$. To compute the switching surfaces in this case a non trivial similarity transformation S in (4.2a) arising from a Jordan normal form decomposition and a dynamic rescaling will be used.

FIRST ORDER In the case of system (4.1) with $n = 1$, $a > 0$, we select a trivial similarity transformation $S = 1$ in (4.2) leading to, similar to the case with $a = 0$,

$$\varphi_1(x) := x_1 \,. \tag{4.11}$$

Note that in this case the time-optimal switching function coincides with the case of $a = 0$, $n = 1$.

SECOND ORDER In the second order case, i.e. system (4.1) with $n = 2$, $a > 0$, we rely on the following similarity transformation S:

$$S = \begin{bmatrix} a & 0 \\ a & a^2 \end{bmatrix} \tag{4.12a}$$

which leads to, following equation (4.2)

$$A = \begin{bmatrix} -a & 0 \\ 0 & 0 \end{bmatrix}, \quad b = \begin{bmatrix} a \\ a \end{bmatrix} \,. \tag{4.12b}$$

The arising dynamics leads to

$$\varphi_2(x) := x_2 - \operatorname{sign}\left(\varphi_1(x_1)\right) \log(1 + \operatorname{sign}\left(\varphi_1(x_1)\right) x_1) \,, \tag{4.12c}$$

where $\varphi_1(x_1)$ is the first order time-optimal switching function for the case with $a > 0$, reported in (4.11). Moreover, equation (4.12c) represents a different parametrization of the time-optimal switching surface presented in [10, Chap 7.4, subsystem (1)-(2)]. Our parametrization preserves a nested structure with the lower and higher order time-optimal switching function.

THIRD ORDER In the case of system (4.1) with $n = 3$, $a > 0$, the similarity transformation that we use is

$$S = \begin{bmatrix} a & 0 & 0 \\ a & a^2 & 0 \\ -a & 0 & a^3 \end{bmatrix}, \tag{4.13}$$

which leads to, following equation (4.2),

$$A = \begin{bmatrix} -a & 0 & 0 \\ 0 & 0 & 0 \\ 0 & a & 0 \end{bmatrix}, \quad b = \begin{bmatrix} a \\ a \\ -a \end{bmatrix} \,. \tag{4.14}$$

The transformed dynamics allows computing the following time-optimal switching function

$$\varphi_3(x) := x_3 + x_2 + \operatorname{sign}\left(\varphi_2([\tfrac{x_1}{x_2}])\right) \times \left(\frac{x_2^2}{2} - \log^2 \left(1 + \sqrt{1 - (1 + \operatorname{sign}\left(\varphi_2([\tfrac{x_1}{x_2}])\right) x_1) e^{-\operatorname{sign}\left(\varphi_2([\tfrac{x_1}{x_2}])\right) x_2}} \right) \right) \,, \tag{4.15}$$

where $\varphi_2([\begin{smallmatrix} x_1 \\ x_2 \end{smallmatrix}])$ is the second order time-optimal switching function for the case with $a > 0$, reported in (4.12c).

Once again, in (4.15) we present a different parametrization of the time-optimal switching surface as compared to the one reported in [10, Chap 7.4] and [90] for the same plant, because the proposed parametrization allows preserving the nested structure with the lower order case.

Moreover, it is interesting to notice that the time-optimal switching functions in the cases with $a > 0$ do not depend on the parameter a, but the dependence on this parameter appears only in the transformation matrix S.

Based on these switching functions and on Proposition 4.1, we will now proceed in illustrating the developed hybrid framework for Robust Time-Sub-Optimal control.

4.3 HYBRID FRAMEWORK FOR ROBUST TIME-SUB-OPTIMAL CONTROL

In this section we exploit Proposition 4.1 and the switching surfaces illustrated in Sections 4.2.2 and 4.2.1 to design an ϵ-modification of the time-optimal feedback law ensuring global convergence to an ϵ-small neighborhood of the origin.

Rather then treating q in (4.2) as an input, we perform this by choosing an overall state:

$$\xi := \mathrm{col}(x,\ q) \in \mathbb{R}^n \times \{-1, 1\} \tag{4.16}$$

and noting that $x \in \mathcal{U}_+$ and $q = 1$ (respectively, $x \in \mathcal{U}_-$ and $q = -1$) implies that q should toggle. Consequently, we represent our hybrid stabilizer in terms of the set $\mathcal{D}_0$ from which q should toggle between $+1$ and -1 via the trivial jump map $q^+ = -q$. In particular, based on Proposition 4.1, one notices that both in $\mathcal{U}_+$ and in $\mathcal{U}_-$, the product $q\varphi_n(x)$ must be negative during flow. Therefore set $\mathcal{D}_0$ could be selected as:

$$\mathcal{D}_0 = \{\xi |\ \varphi_n(x)q > 0\}\,, \tag{4.17}$$

which is not a closed set. Since we are interested in robust stabilizers, and [45] shows that closed jump/flow sets ensure robustness of stability (see the hybrid basic conditions of Assumption 1.1), rather than selecting $\mathcal{D}_0$ in (4.17), we prefer to introduce a hysteresis mechanism related to the choice of a (small) scalar $\epsilon > 0$ and the following ϵ-dependent closed loop:

$$\begin{aligned} \dot{\xi} &= A_c\,\xi \quad \xi \in \mathcal{C} \\ \xi^+ &= A_d\,\xi \quad \xi \in \mathcal{D} \\ \mathcal{C} &:= \{\xi |\ \ \varphi_n(x)q \leq \epsilon\} \\ \mathcal{D} &:= \{\xi |\ \ \varphi_n(x)q \geq \epsilon\} \end{aligned} \tag{4.18a}$$

where, with I_n being the $n \times n$ identity matrix,

$$A_c := \left[\begin{array}{c|c} A & b \\ \hline 0 & 0 \end{array}\right] \in \mathbb{R}^{(n+1)\times(n+1)}$$
$$A_d := \left[\begin{array}{c|c} I_n & 0 \\ \hline 0 & -1 \end{array}\right] \in \mathbb{R}^{(n+1)\times(n+1)} . \tag{4.18b}$$

In system (4.18), matrix A_c simply encodes equation (4.2b), while A_d encodes the toggling mechanism of q. Finally, as commented above, set $\mathcal{D}$ encodes the fact that a switch should happen whenever $q\varphi_n(x) > 0$ (because this means that $x \in \mathcal{U}_- \cup \mathcal{U}_+$ and q has the wrong sign), possibly allowing for some "erroneous" feedback when $|\varphi_n(x)| \leq \epsilon$.

Remark 4.3. *The advantage of this ϵ-modified law is to introduce a hysteresis zone around $\{x|\varphi_n(x) = 0\}$, the set where characterizing the time-optimal feedback could require extra care. Indeed, the selection of a positive ϵ gives several advantages. It allows synthesizing a time-sub-optimal control law based on the knowledge of only the two sets $\mathcal{U}_+$ and $\mathcal{U}_-$. Moreover, it prevents the possibility of Zeno solutions (such as solutions with persistent simultaneous jumps) [45, Definition 2.5], corresponding to having a control q that switches infinitely fast, causing chattering phenomena and possibly damaging of the actuators. Moreover, this ϵ-inflation makes the controller robust to unmodeled dynamics or sufficiently small measurement noise. The smaller is the hysteresis amplitude ϵ, the closer the input is to the optimal one, but the less robust is the control scheme. Therefore, the parameter ϵ represents a controller tuning parameter, acting as a trade-off between optimality and robustness.* ⌟

Stability properties will be established for sets where the input q is "don't care" and the state x belongs to some compact neighborhood $\mathcal{A}_{xn}$ of the origin. In particular we will focus on compact sets of the form

$$\mathcal{A}_n := \mathcal{A}_{xn} \times \{-1, 1\} . \tag{4.19}$$

Since non-smooth Lyapunov functions will be used for stability certificates, and exploiting the structure of (4.19) and the fact that x remains constant across jumps, we will rely on the following corollary of Theorem 1.1 in Chapter 1 for giving stability certificates of attractor $\mathcal{A}_n$ in (4.19).

Corollary 4.1. *If there exists a Lipschitz function $x \mapsto V(x)$ such that:*

1. *V is positive definite with respect to $\mathcal{A}_{xn}$ and radially unbounded;*
2. *using $\xi = (x, q)$ and the Clarke subdifferential $\partial V(x)$ of V,*

$$\dot{V}(\xi) := \max_{v \in \partial V(x)} \langle v,\, A_c\xi \rangle \leq 0 \quad \forall \xi \in \mathcal{C} \setminus \mathcal{A}_n ; \tag{4.20}$$

3. *no complete solution exists that keeps V constant and non zero;*

then $\mathcal{A}_n$ in (4.19) is uniformly globally asymptotically stable for (4.18).

Proof. *Since V depends on x only, and x remains constant across jumps, then the condition $G(\mathcal{A} \cap \mathcal{D}) \subset \mathcal{A}$ in Theorem 1.1 is trivially satisfied, and $V(x^+) - V(x) \leq 0$ for all $\xi \in \mathcal{D}$. The remaining assumptions of Theorem 1.1 are guaranteed by the hypotheses of Corollary 4.1.* □

Remark 4.4. *Rigorous stability certificates will be given for the case of $a = 0$, $n \in \{1, 2\}$ and $a > 0$, $n = 1$ for system (4.18). The proof of stability for the other cases is still an open problem and object of research which in this thesis will be treated as a conjecture.* ⌟

4.3.1 The first order case

The first order case (i.e. $n = 1$) is the only case that can be studied in a general way, both for $a = 0$ and $a > 0$, that is with $a \geq 0$. We therefore specialize system (4.18) with $n = 1$ and $a \geq 0$, making use of the switching function $\varphi_1(x)$ in equation (4.5) and (4.11).

For clarity, the phase portrait of such a system is depicted in Figure 4.2.

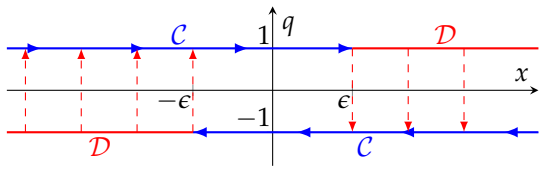

Figure 4.2: Flow set $\mathcal{C}$ and jump set $\mathcal{D}$ on the phase portrait of system (4.18) with $n = 1$, $a \geq 0$.

Figure 4.2 shows that the hysteresis introduced by parameter $\epsilon > 0$ turns into allowing flows with any value of q when $x_1 \in [-\epsilon, \epsilon]$. The solutions exhibit a steady-state limit cycle. Inspecting that limit cycle we may define the following bounded attractor:

$$\begin{aligned} \mathcal{A}_1 :=& \mathcal{A}_{x1} \times \{-1, 1\} = [-\epsilon, \epsilon] \times \{-1, 1\} \\ =& \{x | \ \mathrm{dz}_\epsilon(\varphi_0(x)) = 0\} \times \{-1, 1\}, \end{aligned} \tag{4.21a}$$

where the deadzone function $\mathrm{dz}_\epsilon(\cdot)$ is defined as:

$$\mathrm{dz}_\epsilon(x) := \begin{cases} 0 & \text{if } -\epsilon \leq x \leq \epsilon \\ x - \epsilon & \text{if } x \geq \epsilon \\ x + \epsilon & \text{if } x \leq -\epsilon \end{cases} \tag{4.21b}$$

The following statement establishes its useful properties in terms of pratical stabilization of the origin of (4.1a) (equivalently of (4.2b)).

Theorem 4.2. *Attractor (4.21a) is uniformly globally asymptotically stable (UGAS) for (4.18) with $n = 1$ and $a \geq 0$.*

Proof. *Consider the differentiable candidate Lyapunov function $V_1 : \mathbb{R} \to \mathbb{R}$ defined as*

$$V_1(x) := \frac{1}{2}\mathrm{dz}_\epsilon^2(\varphi_1(x)) \ . \tag{4.22}$$

In other words, $V_1(x)$ is the square of the distance of x from $[-\epsilon, \epsilon]$, and, trivially, $V_1(x) = 0 \ \forall x \in \mathcal{A}_{1x} = [-\epsilon, \epsilon]$, $V_1(x) > 0 \ \forall x \in \mathbb{R} \setminus \mathcal{A}_{1x}$, and it is radially unbounded, thus satisfying item 1 of Proposition 4.1. Also,

$$\begin{aligned} &\dot{V}_1(\xi) = \langle \nabla V_1(x),\, A_c \xi \rangle = \mathrm{dz}_\epsilon\left(\varphi_1(x)\right) \dot{x}_1 = \\ &= \mathrm{dz}_\epsilon\left(\varphi_1(x)\right)(q - a x_1) = q\mathrm{dz}_\epsilon\left(\varphi_1(x)\right) - a x_1 \mathrm{dz}_\epsilon\left(\varphi_1(x)\right) . \end{aligned} \tag{4.23a}$$

Thanks to the flow set definition in (4.18), during flows it holds that $\varphi_0(x) q \leq \epsilon$. Moreover, $\xi \in \mathcal{C} \setminus \mathcal{A}_1$ implies $|\varphi_1(x)| > \epsilon$, therefore

$$\varphi_1(x) q < -\epsilon \tag{4.23b}$$

implying

$$q\mathrm{dz}_\epsilon\left(\varphi_1(x)\right) < 0 \ \ \forall \ \ \xi \in \mathcal{C} \setminus \mathcal{A}_1 . \tag{4.23c}$$

The fact that

$$-a x_1 \mathrm{dz}_\epsilon\left(\varphi_1(x)\right) \leq 0 \ \ \forall \ \ \xi \in \mathcal{C} \setminus \mathcal{A}_1 \tag{4.23d}$$

is trivial since $a \geq 0$ and $\varphi_1(x) = x_1$, and therefore (4.22) implies

$$\dot{V}_1(\xi) < 0 \ \ \forall\, \xi \in \mathcal{C} \setminus \mathcal{A}_1 , \tag{4.23e}$$

which implies item 2 of Proposition 4.1 and also implies item 3 because any (complete) solution is such that after any jump $\xi^+ \in \mathcal{C} \setminus \mathcal{D}$, and some flow must occur, which will cause a decrease of V_1 (if non zero) from (4.23e). Proposition 4.1 finishes the proof. □

Remark 4.5. *The convergence to attractor $\mathcal{A}_1$ is a finite-time type of convergence.* ⌟

4.3.2 The Double Integrator

We now specialize system (4.18) with $n = 2$ and $a = 0$, i.e., for the double integrator, making use of the switching function $\varphi_2(x)$ in equation (4.5). For clarity, the phase portrait of this system is depicted in Figure 4.3.

Observe that also in this case the hysteresis introduced by the parameter $\epsilon > 0$ introduces a neighborhood of $\{x | \varphi_n(x) = 0\}$ where solutions can flow for any of the two values of q. The solutions exhibit an "eye-shaped" steady-state limit cycle whose orbit can be described by:

$$\lambda_2 := \{x |\ v(x) = \epsilon\} \tag{4.24}$$

where $v(x)$ is the following scalar function:

$$v(x) := \begin{cases} \dfrac{x_1^2}{2} + x_2 & \text{if } x_2 \geq 0 \\ \dfrac{x_1^2}{2} - x_2 & \text{if } x_2 \leq 0 \end{cases} , \tag{4.25}$$

Let us now define the following bounded attractor, also depicted in green in Figure 4.3:

$$\mathcal{A}_2 := \mathcal{A}_{2x} \times \{-1, 1\} := \{x |\ v(x) \leq \epsilon\} \times \{-1, 1\} . \tag{4.26}$$

The next theorem parallels Theorem 4.2 for the case $n = 2$.

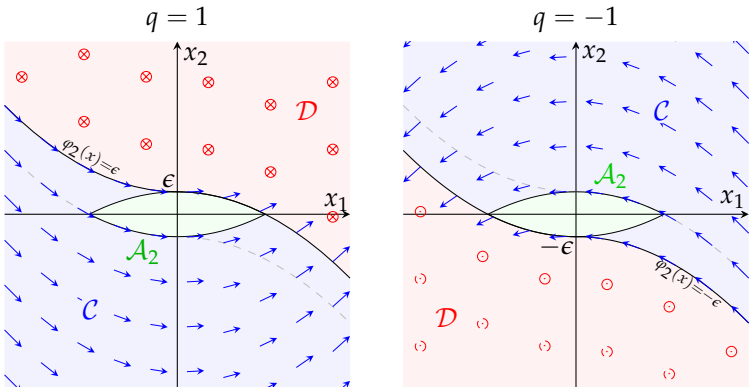

Figure 4.3: Flow set $\mathcal{C}$ and jump set $\mathcal{D}$ on the phase portrait of system (4.18) with $n = 2$ and $a = 0$.

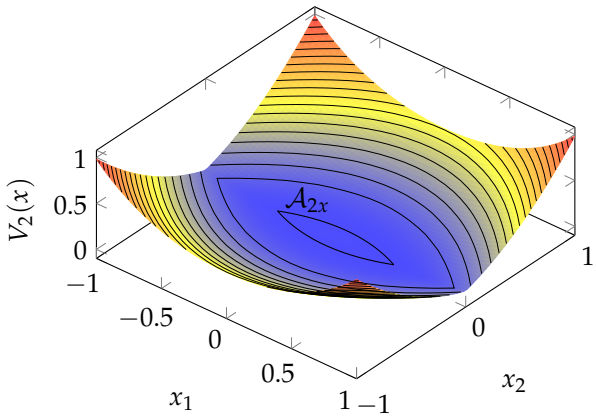

Figure 4.4: Lyapunov function V_2 in (4.27) and attractor $\mathcal{A}_{2x}$ in (4.26).

Theorem 4.3. *Attractor (4.26) is UGAS for (4.18) with $n = 2$ and $a = 0$.*

Proof. *Consider the candidate Lyapunov function $V_2 : \mathbb{R}^2 \to \mathbb{R}$ defined as:*

$$V_2(x) := \frac{1}{2}\mathrm{dz}_\epsilon^2\left(v(x)\right) \tag{4.27}$$

where v is defined in (4.25). It holds that $V_2(x) = 0 \;\forall\; x \in \mathcal{A}_{2x}$, $V_2(x) > 0 \;\forall\; x \in \mathbb{R}^2 \setminus \mathcal{A}_{2x}$, and V_2 is radially unbounded, thus proving item 1 of Proposition 4.1. Items 2 and 3 are proven below. The Clarke subdifferential ∂V_2 of V_2, is, at points where V_2 is not differentiable, the convex hull of gradients of V_2 at nearby points where V_2 is differentiable [30, Theorem 2.5.1]. Hence

$$\partial V_2(x) = \bigcup_{s \in \mathrm{SGN}(x_2)} \left\{ \mathrm{dz}_\epsilon\left(v(x)\right) \begin{bmatrix} x_1 \\ s \end{bmatrix} \right\} \tag{4.28}$$

where $\mathrm{SGN}(\cdot)$ *is the regularized sign function defined as:*

$$\mathrm{SGN}(s) := \begin{cases} -1 & \text{if } s < 0 \\ 1 & \text{if } s > 0 \\ [-1,\, 1] & \text{if } s = 0\,. \end{cases} \tag{4.29}$$

Based on (4.28) *and structure of* A_c *in* (4.18b)

$$\dot{V}_2(\xi) = \max_{\delta \in \partial V_2(x)} \langle \delta,\, Ax + bq \rangle = \max_{s \in \mathrm{SGN}(x_2)} x_1 \mathrm{dz}_\epsilon\left(v(x)\right)(q+s)\,. \tag{4.30}$$

Notice that from (4.25) $\mathrm{dz}_\epsilon\left(v(x)\right) > 0 \;\; \forall \;\; x \in \mathbb{R}^2 \setminus \mathcal{A}_{2x}$.

Let us now evaluate $\dot{V}_2(\xi)$ *in three separate cases.*

Let $x_2 > 0$, *i.e.,* $s = 1$ *in* (4.30). *If* $q = -1$, *then* $\dot{V}_2(\xi) = 0$, *whereas with* $q = 1$ *we exploit the fact that for proving item 2 of Proposition 4.1 the analysis has to be carried out in* $\mathcal{C} \setminus \mathcal{A}_2$, *which (from trivial computations) implies that* $x_1 < 0$ *(see Figure 4.3 for an intuition), and then* $\dot{V}_2(\xi) < 0$. *Parallel reasonings holds for* $x_2 < 0$.

Consider now the case $x_2 = 0$. *By recalling that* $\mathrm{SGN}(0) = [-1,\, 1]$ *in* (4.30), $\dot{V}_2(\xi)$ *reduces to:*

$$\dot{V}_2(\xi) = \mathrm{dz}_\epsilon\left(\frac{x_1^2}{2}\right) \max_{s \in [-1,\, 1]} x_1(q+s)\,. \tag{4.31}$$

If $q = 1$ ($q = -1$, *respectively), using again* $\xi \in \mathcal{C} \setminus \mathcal{A}_2$, *basic computations yield* $x_1 < 0$ ($x_1 > 0$, *respectively), and therefore we can conclude that* $\dot{V}_2(\xi) = 0$.

Thus, we have that $\dot{V}_2(\xi) \leq 0 \;\; \forall \xi \in \mathcal{C} \setminus \mathcal{A}_2$, *which implies item 2 of Proposition 4.1.*

It remains to show Item 3 of Proposition 4.1. The dynamics is such that every flowing solution not starting in $\mathcal{A}_2$ *will make* x *enter the open second or fourth quadrant, namely the set where* $x_1 x_2 < 0$. *In these quadrants, the dynamics makes* x_1 *increase in norm, and* x_2 *decrease in norm, thus the solution will enter the jump set. The jump dynamics then maps the solution into the set where* $x_1 q < 0$. *Combining* $x_1 x_2 < 0$ *with* $x_1 q < 0$, *we obtain* $x_1(q+s) < 0$, *which guarantees* $\dot{V}_2(\xi) < 0$, *as noticeable from* (4.30). *Therefore all solution initially flowing, eventually lead to a decrease of* V_2. *Consider now solutions initially jumping. Since the image* $\mathcal{D}^+$ *of the jump set* $\mathcal{D}$ *trough the jump dynamics is in the interior of the flow set* $\mathcal{C}$ *(from* (4.18)), *i.e.,* $\mathcal{D}^+ = \{\xi | \varphi_1(x) q \leq -\epsilon\} \subset \mathrm{int}(\mathcal{C})$, *then any such solution will start flowing after the jump, and the previous analysis proves decrease of* V_2.

Therefore, Proposition 4.1 establishes UGAS of $\mathcal{A}_2$. □

4.3.3 The remaining cases

As mentioned in Remark 4.4, the problem of giving rigorous stability certificates for system (4.18) in the case of $a = 0$, $n = 3$ and $a > 0$, $n \in \{2,\, 3\}$ is a non-trivial problem which is still open. We therefore continue this manuscript formulating the following conjecture.

Conjecture 4.1. *There exists some compact neighborhood $\mathcal{A}_{xn}$ of the origin of system (4.2) such that the attractor defined in (4.19) is UGAS for (4.18) in the cases of $a = 0$, $n = 3$ and $a > 0$, $n \in \{2, 3\}$.*

In support of Conjecture 4.1, we report some numerical analysis in the cases of $a = 0$, $n = 3$ and $a > 0$, $n \in \{2, 3\}$.

CASE $n = 2$, $a > 0$ In Figure 4.5 we report three simulations of system (4.18) in the case of $n = 2$, $a = 1$ showing both the evolution in the phase space and the time history of states x and q. Parameter ϵ was set to $\epsilon = 0.13$. The simulation starts from three different initial conditions for the state x:

$$\begin{aligned} x_{01} &:= (-1.0, -1.5) && \text{blue curve in Figure 4.5} \\ x_{02} &:= (-1.0, 1.5) && \text{red curve in Figure 4.5} \\ x_{03} &:= (1.7, -1.7) && \text{green curve in Figure 4.5} \end{aligned} \tag{4.32}$$

The initial condition for q was chosen in such a way to obtain solutions starting with a flow phase. It is possible to observe that similarly to the case $n = 1$, $a = 0$ the solutions end up in a steady-state limit cicle at the border of an "eye-shaped" set containing the origin, corroborating Conjecture 4.1. Indeed, this suggests that there exist a neighborhood of the origin $\mathcal{A}_{xn}$ in (4.19) to which system (4.18) with $n = 2$, $a > 0$ is UGAS.

CASE $n = 3$, $a = 0$ In Figure 4.6 two simulations of system (4.18) with $n = 3$, $a = 0$ are depicted. For the sake of clarity, we reported the simulations in the phase space of state x, while state q is represented by a color code, i.e., in red the parts of the trajectory with $q = 1$, while in blue the ones with $q = -1$. Parameter ϵ was set to $\epsilon = 0.1$. The initial conditions for state x are reported below in equation (4.33), while the initial condition for state q was selected to have solutions starting with flow.

$$\begin{aligned} x_{01} &:= (0.0, 1.0, 1.0) \\ x_{02} &:= (0.5, -1.0, -1.0) \end{aligned} \tag{4.33}$$

Two representations of the switching function $\varphi_3(x)$ in (4.10) are depicted, in particular, the set $\{x | \varphi_3(x) = -\epsilon\}$ is in orange and the set $\{x | \varphi_3(x) = \epsilon\}$ is in green. It is possible to observe that the solutions exhibit one more time a steady-state "eye-shaped" limit cycle around the origin, depicted with a dashed white curve in Figure 4.6. This observation therefore supports Conjecture 4.1, suggesting that there exist a neighborhood of the origin $\mathcal{A}_{xn}$ in (4.19) to which system (4.18) with $n = 3$, $a = 0$ is UGAS.

CASE $n = 3$, $a > 0$ Finally, we present some numerical evidence for the case of system (4.18) with $n = 3$, $a = 1$. In Figure 4.7 two simulations are depicted in a similar fashion as the previous case of Figure 4.6. The initial conditions for state x are reported below in equation (4.34), and like previously

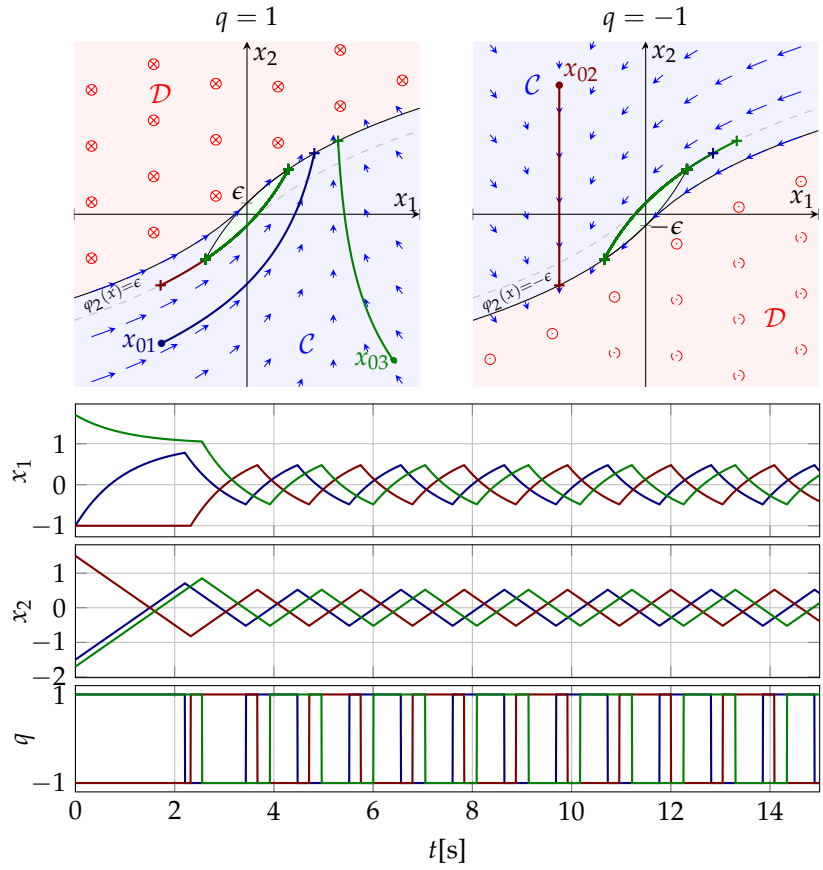

Figure 4.5: Flow set $\mathcal{C}$ and jump set $\mathcal{D}$ on the phase portrait of system (4.18) with $n = 2$, $a = 1$ together with three simulations starting from initial conditions for state x in (4.32).

the initial condition for state q was selected to have solutions starting with flow.

$$\begin{aligned} x_{01} &:= (-0.5,\ 1.0,\ 0.0) \\ x_{02} &:= (1.0,\ -0.7,\ -0.7) \end{aligned} \tag{4.34}$$

Conjecture 4.1 is once more supported by these simulations, showing that the trajectories end up evolving in a limit cycle around the origin, depicted in dashed white in Figure 4.7. These numerical results therefore suggest the existence of a neighborhood of the origin $\mathcal{A}_{xn}$ in (4.19) for which system (4.18) with $n = 3$, $a > 0$ is UGAS.

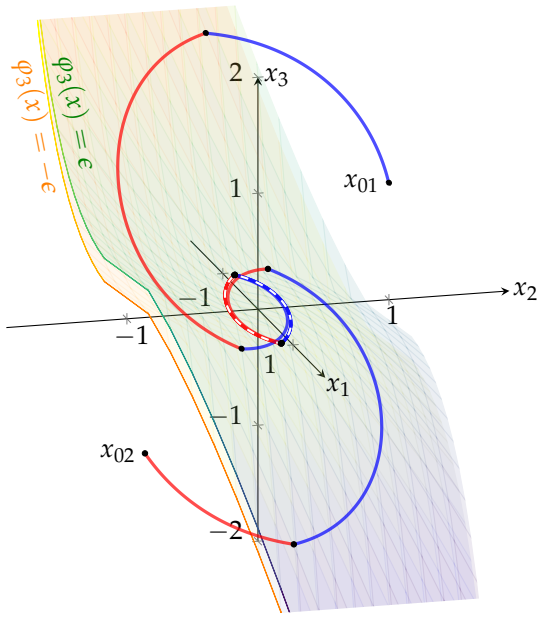

Figure 4.6: Solutions to (4.18) with $n = 3$, $a = 0$. The red and blue part of the trajectory correspond respectively to state $q = 1$ and $q = -1$.

4.4 BLEND WITH A LOCAL LINEAR FEEDBACK

In this section, the blending of the controller developed in Section 4.3 with a local linear feedback is addressed. The local controller is chosen as a linear a state feedback kx inducing the following closed loop:

$$\dot{x} = A_{cl}\, x := (A + b\, k^\top) x\,, \tag{4.35}$$

where $k \in \mathbb{R}^n$ is a suitable gain vector such that matrix A_{cl} is Hurwitz. For example, vector k can be selected as an LQR gain or by means of any other state feedback design procedure.

This controller can be incorporated in hybrid system (4.18) by modifying the matrix A_c previously defined in (4.18b) as follows:

$$A_c = \left[\begin{array}{c|c} A + (1 - |q|) b\, k^\top & b \\ \hline 0 & 0 \end{array}\right] \in \mathbb{R}^{(n+1)\times(n+1)}\,. \tag{4.36}$$

With the latter, the local controller is activated whenever the logic variable q is set to zero. In particular, the new dynamics evolves in the set $\xi \in \mathbb{R}^n \times \{-1,\, 0,\, 1\}$, extending the previous set $\xi \in \mathbb{R}^n \times \{-1, 1\}$ in (4.18).

A strategy for choosing whether the local controller or the global controller of Section 4.3 has to be applied is needed. For this purpose, the *uniting global and local controller* strategy presented in [45, Example 1.7] and [82] is adopted, where we use q as a supervisor variable. In particular, when $|q| = 1$ the global

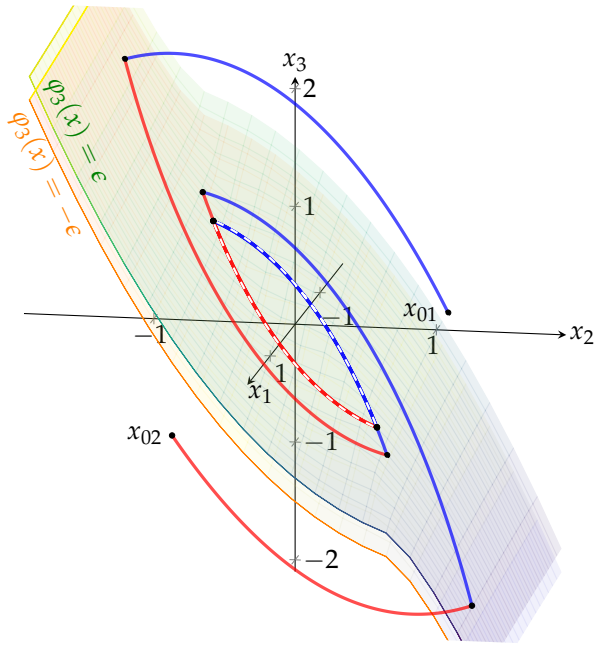

Figure 4.7: Solutions to (4.18) with $n = 3$, $a = 1$. The red and blue part of the trajectory correspond respectively to state $q = 1$ and $q = -1$.

controller is active, whereas when $q = 0$ the local controller is activated by virtue of (4.36).

Following [45, Example 1.7], given scalars $0 < \rho < 1$ and $\ell \in \mathbb{R}_+$ to be chosen later, if $P = P^\top > 0$ is any matrix solving the continuous-time Lyapunov equation

$$(A + bk^\top)^\top P + P(A + bk^\top) < 0, \tag{4.37}$$

we define the set where we would like to switch from the local to the global controller as:

$$\mathcal{D}_l := \left\{ \xi \middle| q = 0,\ x^\top P x \geq \ell \right\}. \tag{4.38a}$$

Also, we define the set where we would like to switch from the global to the local controller as:

$$\mathcal{D}_g := \left\{ \xi \middle| |q| = 1,\ x^\top P x \leq \rho \ell \right\}. \tag{4.38b}$$

The overall jump dynamics turns out to be the following one:

$$\xi^+ \in G(\xi), \quad \xi \in \mathcal{D}_u := \mathcal{D}_l \cup \mathcal{D}_g \cup \mathcal{D}, \tag{4.39a}$$

where the jump map $G(\xi)$ corresponds to:

$$G(\xi) = \begin{cases} \left\{ \begin{bmatrix} x \\ \pm(1-|q|) \end{bmatrix} \right\} & \text{if } \xi \in (\mathcal{D}_l \cup \mathcal{D}_g) \setminus \mathcal{D} \\ \begin{bmatrix} x \\ -q \end{bmatrix} & \text{if } \xi \in \mathcal{D} \setminus (\mathcal{D}_l \cup \mathcal{D}_g) \\ \left\{ \begin{bmatrix} x \\ \pm(1-|q|) \end{bmatrix} \right\} \cup \left\{ \begin{bmatrix} x \\ -q \end{bmatrix} \right\} & \text{if } \xi \in \mathcal{D} \cap (\mathcal{D}_l \cup \mathcal{D}_g), \end{cases} \tag{4.39b}$$

with

$$\left\{ \begin{bmatrix} x \\ \pm(1-|q|) \end{bmatrix} \right\} := \left\{ \begin{bmatrix} x \\ (1-|q|) \end{bmatrix} \right\} \cup \left\{ \begin{bmatrix} x \\ -(1-|q|) \end{bmatrix} \right\}. \tag{4.39c}$$

The overall flow equation is enabled on the closed complement of $\mathcal{D}_u$, and from (4.18) corresponds to:

$$\dot{\xi} = A_c \, \xi \,, \quad \xi \in \mathcal{C}_u := \overline{\mathbb{R}^n \times \{-1, 0, 1\} \setminus \mathcal{D}_u}, \tag{4.39d}$$

with A_c defined in equation (4.36).

The proposed scheme is completed by a suitable selection of the scalars ℓ and ρ in (4.38) ensuring that the local feedback $k^\top x$ has smaller norm than 1 (i.e., it is below the saturation level) as long as $x^\top P x \leq \ell$. This property is established in the next lemma.

Lemma 4.1. *Given $P = P^\top > 0$ and a gain $k \in \mathbb{R}^n$, if $\ell = (k^\top P^{-1} k)^{-1}$, then*

$$x^\top P x \leq \ell \Rightarrow |k^\top x| \leq 1. \tag{4.40}$$

Proof. *As in [54, Example 8.8], the following holds:*

$$\min_{|k^\top x| \geq 1} x^\top P x = \min_{|k^\top x| = 1} x^\top P x = (k^\top P^{-1} k)^{-1} = \ell \,. \tag{4.41}$$

Therefore, we have (4.40) by contradiction, because, from (4.41), no $\overline{x}$ exists such that $\overline{x}^\top P \overline{x} \leq \ell$ and $|k^\top \overline{x}| > 1$. □

Based on Lemma 4.1, we can prove the following statement, which requires that set $\mathcal{A}_n$ is sufficiently small (ϵ is sufficiently small) or scalar ℓ is sufficiently large (k is sufficiently small).

Theorem 4.4. *Given P and k satisfying (4.37) and $\ell = (k^\top P^{-1} k)^{-1}$, if $\rho \in (0, 1)$ and ϵ are such that $\mathcal{A}_n \subset \text{int}(\mathcal{D}_g)$ and $\mathcal{A}_n$ is UGAS for system (4.18), then $A_0 := \{0\} \times \{-1, 0, 1\}$ is UGAS for system (4.39).*

Proof. *UGAS of $\mathcal{A}_n$ together with $\mathcal{A}_n$ being in the interior of $\mathcal{D}_g$ implies uniform finite-time convergence to the interior of $\mathcal{D}_g$. Since the local controller is activated (from (4.39b)) before leaving the boundary of $\mathcal{D}_g$, and $\mathcal{D}_g$ is forward invariant and contractive for the arising closed-loop (see (4.37)), then UGAS of $\mathcal{A}_0$ follows from forward invariance and uniform global attractivity of $\mathcal{A}_0$ [45, Prop. 7.5].* □

The condition $\mathcal{A}_n \subset \text{int}(\mathcal{D}_g)$ could be hard to check in general, but becomes trivial for the case $n = 1$, both for $a = 0$ and $a > 0$. For the cases with $n > 1$, as a general approach, even if possibly conservatively, we propose to rely on an auxiliary bounding box $\mathcal{B}$ of the attractor $\mathcal{A}_n$ (such that $\mathcal{A}_n \subset \mathcal{B}$) for which $\mathcal{B} \subset \text{int}(\mathcal{D}_g)$ is easier to check. In particular, for the case $n = 2$, $a = 0$ according to Figure 4.8, we suggest the selection

$$\mathcal{B} := \{\xi | |x_1| < \sqrt{2\epsilon},\ |x_2| < \epsilon\}\,. \tag{4.42}$$

Corollary 4.2. *Given P and k satisfying (4.37) and $\ell = (k^\top P^{-1} k)^{-1}$, if*

$$\max\{\alpha^\top P \alpha,\ \beta^\top P \beta\} < \rho\ell \tag{4.43}$$

with $\alpha = [\sqrt{2\epsilon},\ \epsilon]^\top$ and $\beta = [\sqrt{2\epsilon},\ -\epsilon]^\top$ (i.e., the two vertices of the box $\mathcal{B}$), then $\mathcal{A}_0$ is UGAS for system (4.39).

Proof. *Property (4.43) implies that the four vertices $x_i,\ i = 1, \ldots, 4$ of $\mathcal{B}$ satisfy $x_i^\top P x_i < \rho\ell$. Since $\mathcal{B}$ is convex,*

$$\max_{x \in \mathcal{B}} x^\top P x < \rho\ell\,, \tag{4.44}$$

which clearly implies $\mathcal{B} \subset \text{int}(\mathcal{D}_g)$. Theorem 4.3 then establishes UGAS of $\mathcal{A}_2$, which, together with Theorem 4.4 proves UGAS of $\mathcal{A}_0$. □

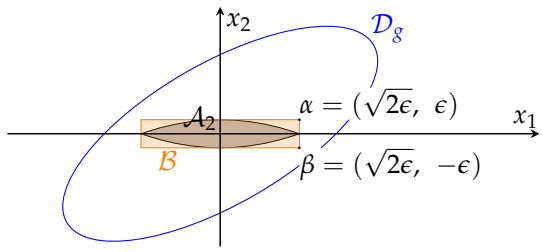

Figure 4.8: Bounding box $\mathcal{B}$, attractor $\mathcal{A}_2$ and jump set $\mathcal{D}_g$ in the case $n = 2$, $a > 0$.

Similar conditions to Corollary 4.43 can be checked for the other cases as well. For the case $n = 3$, $a = 0$ this approach leads to the computation of a bounding box $\mathcal{B}$ containing the limit-cycle arising from (4.18) as illustrated in Section 4.3.3 computing the maximum amplitudes of the limit-cycle for each state. In particular, it is possible to describe this bounding box $\mathcal{B}$ as a box centered in the origin with positive and negative widths equivalent to the components of α defined as follows

$$\alpha := \left(\alpha_1,\ \frac{\alpha_1^2}{2},\ \frac{\alpha_1^3}{3}\right) = \left(\sqrt{2}\epsilon^{1/3},\ \epsilon^{2/3},\ \frac{2\sqrt{2}}{3}\epsilon\right)\,, \tag{4.45}$$

that is

$$\mathcal{B} := \left\{\xi \,|\, |x_1| < \sqrt{2}\epsilon^{1/3},\ |x_2| < \epsilon^{2/3},\ |x_3| < \frac{2\sqrt{2}}{3}\epsilon\right\}\,. \tag{4.46}$$

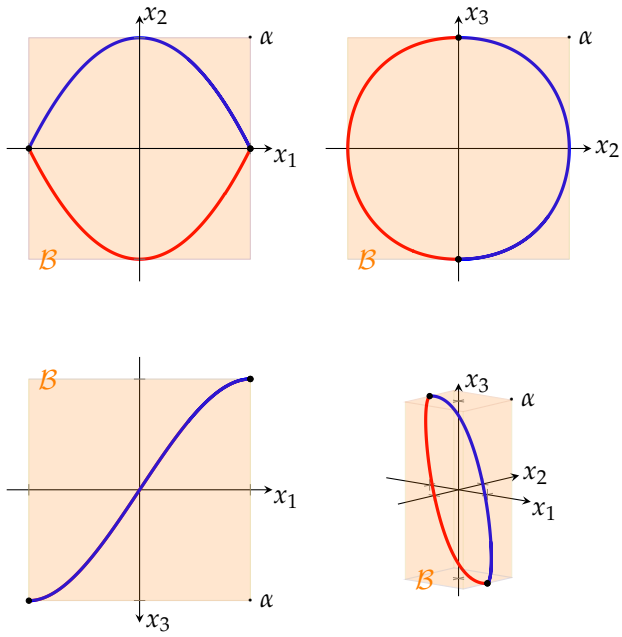

Figure 4.9: Bounding box $\mathcal{B}$, and limit cycle of system (4.18) with $n = 3$, $a = 0$.

For the case $n = 2$, $a > 0$, the bounding box containing the arising limit cycle illustrated in Section 4.3.3 has positive and negative widths equivalent to the components of α defined as follows

$$\alpha := (\alpha_1, \operatorname{atanh}(\alpha_1)) = \left(\frac{\sqrt{e^{2\epsilon} - 1}}{e^{\epsilon}}, \operatorname{atanh}\left(\frac{\sqrt{e^{2\epsilon} - 1}}{e^{\epsilon}} \right) \right), \tag{4.47}$$

where $x \mapsto \operatorname{atanh}(x)$ is the inverse hyperbolic tangent function defined on the open set $(-1, 1)$. Note that $\lim_{\epsilon \to \infty} \alpha_1 = 1$.

For the case with $n = 3$, $a > 0$, the computation of a bounding box containing the limit cycle induced by (4.18) leads to finding the solution of transcendent equations, therefore requiring a numerical approach.

In the following two chapters, the application of the developed RTSO controller to two real-scenario cases will be illustrated by means of two different experimental setups. In particular, the case of $n = 3$, $a > 0$ will prove to be of a particular technological interest, since it well represents the common scenario of a second order system such as a free inertia controlled by an actuator with a quasi-first-order dynamical behavior.

5 BENCHMARK MODEL OF QUANSER'S 3 DOF HELICOPTER

This chapter proposes a software benchmark tool for the three degrees-of-freedom experiment "3 DOF Helicopter" by Quanser, based on a multi-body model of the experimental setup. Along with this software-in-the-loop tool, a novel reduced complexity non-linear model for the Quanser "3 DOF Helicopter" is derived, with the scope of being used in the control synthesis phase. A feedback linearizing control law is as well proposed, based on the reduced complexity model. This benchmark tool will be then used in Chapter 6 for validate the RTSO controller developed in Chapter 4 in a real-world scenario. This chapter is based on the work currently under revision [22].

5.1 INTRODUCTION: LITERATURE REVIEW AND PROBLEM STATEMENT

Propeller-actuated aerial vehicles and unmanned aerial vehicles (UAVs) are gaining increasing popularity (they are de-facto a standard) due to their simplicity and the availability of increasingly cheaper and lightweight control and sensing electronics. Nevertheless, due to their under-actuated nature, they represent an interesting and challenging control application. Many different architectures of propeller-actuated aerial vehicles have been proposed and studied, frequently in the VTOL (Vertical Take Off and Landing) configuration. Among these, consider the widespread quadrotors drones [49], ducted-fan configurations [81], and helicopter-like configurations [52].

The use of a benchmark platform both for research and educational purposes is a well established practice in these days. Quanser [84] is a Canada-based company that supplies a vast range of didactic platforms for control, robotics and mechatronics applications. Among these, a relevant propeller-based platform comprising many of the challenges of the VTOL configuration is the three degrees-of-freedom (DOF) experiment *"3 DOF Helicopter"*, because not only it is actuated by the nowadays vastly used propeller actuation, but it is underactuated and embeds a multi-body dynamics. It is composed by three rotational joints, with the end bar carrying a pair of propellers actuated by DC-motors. Measurements of the joints angles are supplied by incremental encoders and two power amplifiers are in charge of actuating the DC-motor/propeller assemblies. Both angular measurements and control voltages are then made available in *MATLAB-Simulink* environment.

For these reasons, Quanser's *"3 DOF Helicopter"* is considered a challenging application and a good benchmark example. Indeed, many works focusing

on the control of this platform have appeared in the last years, proposing a variety of control strategies and focusing on different aspects. Among them, robust schemes are widely investigated. For example, [88] proposes two robust controllers based on sliding mode techniques, while [64] proposes a robust hierarchical controller. The authors of [106] focus on the regulation of two of the three helicopter's degrees-of-freedom thanks to a robust attitude control algorithm and an exogenous system in charge of generating the reference signals. In [63], a decentralized robust second-order consensus tracking controller is proposed for a bench of 3-DOF helicopters. Adaptive control seems to be another well investigated control strategy. Indeed, [29] makes use of the *"3 DOF Helicopter"* for experimentally validating an adaptive attitude controller based on the super-twisting algorithm, while in [41] the adaptive paradigm is addressed based on passivity and Implicit Reference Model techniques. In [80] a linear matrix inequality (LMI) procedure is proposed which allows designing simple adaptive control laws, while [61] focuses on an adaptive parameter identification algorithm. In [59], an adaptive controller is proposed which considers adaptation to parametric uncertainty, unmodeled dynamics, and actuator characteristics, while in [51] a nonlinear adaptive controller is considered, which includes a parameter identification scheme in the closed loop. In [85] a nonlinear model using a tree structure notation is developed, whose parameters are identified with an inverse dynamic model, while [56] deals with the trajectory tracking problem considering both state and input constraints in order to accomplish aggressive maneuvers. In [43], a data-driven controller is synthesized for an experimental setup similar to the Quanser's 3-DOF Helicopter, and in [67] an optimal output regulation problem is faced for the same experimental setup. In [27], combining a continuous differentiator with an adaptive super twisting design, a controller is proposed, capable of accurate tracking while reducing the control effort.

Finally, in [103] a nonlinear multivariable predictive controller is proposed, based on a each-sample-linearization of a neural network model of the nonlinear plant.

All of the above mentioned works are based on various reduced complexity models of the full helicopter dynamics. In this chapter, instead, we propose the derivation of a full dynamical model of the Quanser *"3 DOF Helicopter"* experiment, based on a multi-body representation of the physical setup. A motivation for developing a multi-body model of the experimental setup is that a rigid body model cannot well represent the corresponding complex coupled dynamics. Based on this multi-body representation, we develop a software-in-the-loop platform in the *MATLAB-Simulink* environment based on the *Simscape* package, which takes into account a number of implementation features. We provide a downloadable version of this simulator as well, available at (`https://github.com/mrkrb/3dof_helicopter_benchmark`), in order to make it usable by everyone for testing and validating control algorithms, thereby obtaining reliable results before running actual experiments. This benchmark can be useful both for teaching and for research purposes. Indeed, to the best of our knowledge, no reliable simulation model is available in the literature for this widespread experimental setup. In addition to the above, based on

Figure 5.1: Picture of the Quanser *"3 DOF Helicopter"*.

the Lagrangian representation of the full dynamical model, a novel reduced complexity model is also derived, with the objective of supplying a tool to be used for control design. Differently from past works, the proposed reduced complexity model is derived with a strong link to the full dynamical model. Both the full model and the control model are identified using experimental data, and a comparison is performed with existing models from the literature. A feedback-linearizing controller has been finally developed based on the reduced complexity model, and has been then tested both on the simulation tool and on the real experiment, obtaining consistently desirable results, once more proving that the proposed control model catches the most relevant dynamical behavior of the experimental setup.

5.2 THE EXPERIMENTAL SETUP AND MECHANICAL MODEL

The experimental setup considered in this work is the Quanser *"3 DOF Helicopter"* and we will refer to it as "the helicopter". In particular, the used specimen is the one present at the LAAS-CNRS in Toulouse (FR).

It is composed by a base on which an arm is connected by means of 2 revolute joints, one allowing the arm to rotate around the vertical axis (the "travel" motion), and one allowing the arm to tilt around the horizontal axis (the "elevation" motion). The helicopter body is mounted on one of the two extremities and it is allowed to tilt around the axis aligned with the arm (the "pitch" motion). It carries two propellers actuated by two DC-motors, which can generate a force that depends on the applied voltage. On the other arm extremity, a counterweight is mounted. The three "degrees-of-freedom" (*dof*), (i.e. the travel, the elevation and the pitch) are measured by three encoders with a resolution of 0.0015 rad. A picture of the helicopter is reported in Figure 5.1.

In order to study the helicopter motion, we now proceed with the illustration of a mechanical dynamical model (the "mechanical model" in the following) that fully describes the helicopter mechanical dynamics. This model is a lumped-mass model, with the mass concentrated in four points, two representing the counterweight and the arm, and the other two representing the

two motor-propeller assemblies. In Figure 5.2, a representation of the model is depicted.

Some simplifying assumptions are exploited when deriving the mechanical model: the gyroscopic torques developed by the spinning motor-propeller assemblies are neglected, as well as the aerodynamic effects acting on the helicopter. The structure is considered as non deformable.

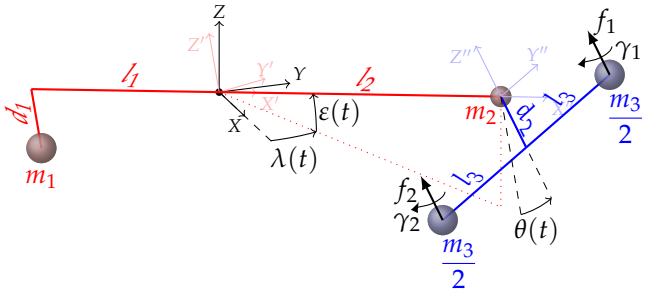

Figure 5.2: Mechanical model of the helicopter.

In the following description we will refer to some physical quantities, such as the lumped masses m_1, m_2, and m_3 represented by spheres in Figure 5.2, and lengths l_1, l_2, and d_1 of the helicopter arm, and l_3, d_2 of the helicopter body.

Let us start by defining an inertial Reference Frame (RF) $\{X\text{-}Y\text{-}Z\}$ whose origin corresponds to the point where the arm is connected to the base by means of the two revolute joints. We will refer to this reference frame as the "inertial RF". We consider the gravity acting along the negative Z direction with magnitude g. A second RF $\{X'\text{-}Y'\text{-}Z'\}$ (represented in light red in Figure 5.2) is obtained by applying to the inertial RF a Z-Y rotation sequence, corresponding respectively to a rotation of an angle $\lambda(t)$ (travel angle) and a subsequent rotation of an angle $-\varepsilon(t)$ (elevation angle). The arm of the helicopter lays along the X'-axis: for this reason we call the $\{X'\text{-}Y'\text{-}Z'\}$ frame the "arm RF". The arm mass is concentrated at its extremities, therefore we place a first mass m_1 at $(-l_1,\, 0,\, -d_1)$ and a second mass m_2 at $(l_2,\, 0,\, 0)$, both in the arm RF. A third RF $\{X''\text{-}Y''\text{-}Z''\}$ (represented in light blue in Figure 5.2) is obtained starting from the arm RF and applying a translation of l_2 along the X'-axis and a rotation of an angle $\theta(t)$ (pitch angle) around the same axis. The helicopter body lays in this third RF, for this reason we refer to $\{X''\text{-}Y''\text{-}Z''\}$ as the "helicopter body RF". As mentioned before, the helicopter body mass m_3 is split in two halves, each one concentrated at one extremity of the helicopter body. Therefore, the two masses representing the motors-propellers assemblies are placed respectively at $(0,\, l_3,\, -d_2)$ (front motor-propeller assembly) and at $(0,\, -l_3,\, -d_2)$ (rear motor-propeller assembly), both coordinates being expressed in the helicopter body RF. Moreover, two lumped forces parallel to the Z''-axis are placed in correspondence to the two motor-propeller assemblies, respectively f_1 for the front and f_2 for the rear. These forces represent the forces generated by the spinning propellers. Finally, two torques γ_1 and γ_2 are applied at the

same positions, representing the aerodynamics drag torques exerted by the propellers.

Without loss of generality, a constraint equation is added to the mechanical model, and it is such that the elevation equilibrium position corresponds to zero. This is done by selecting $m_1 = \frac{l_2}{l_1}(m_2 + m_3)$.

The friction at the joints has to be taken into account as well. While complex friction models, such as Coulomb friction, could be considered and implemented in the mechanical model, those highly nonlinear effect do not seem to be dominant in the experimental responses. Therefore, to reduce the model complexity we consider only linear viscous friction acting at each joint. Similar assumptions have been made in past works focusing on this experiment, for example in [41], [29], and in [80].

As the common practice, we assume that both the thrust forces f_1 and f_2 as well as the drag torques γ_1 and γ_2 exerted by the propeller have a quadratic relationship with the angular speed of the propellers themselves (see for example [26] and [39]). This leads to a linear relation between the thrust force and the drag torque (see for example [72]):

$$\gamma_i = k_{\gamma f} f_i \quad i \in \{1, 2\}. \tag{5.1}$$

For the helicopter, the propellers are both right-handed, therefore $k_{\gamma f} < 0$.

The mechanical model introduced in this section fully describes the dynamics of the helicopter experiment, and can be used in order to validate a reduced complexity model designed for control purposes. Moreover, it can be straightforwardly implemented in numerical physical simulation softwares such as *MathWorks Simscape* in order to simulate the helicopter dynamics and using it as a model-in-the-loop test platform for control strategies. Indeed, a *MathWorks Simscape* implementation of the proposed model is provided here (`https://github.com/mrkrb/3dof_helicopter_benchmark`), which embeds as well the identified parameters thanks to the procedure discussed further in the chapter in Section 5.4.

5.3 REDUCED COMPLEXITY MATHEMATICAL MODEL

The aim of this section is to build a reduced complexity mathematical model of the helicopter that, in spite of its simplicity, captures the most relevant dynamic behavior of the real experiment. This model is useful in order to synthesize control laws, and we will refer to it as the "control model". The control model is constructed based on the mechanical model described in Section 5.2, depicted in Figure 5.2.

5.3.1 Standard Lagrangian derivation

The Lagrangian approach is widely used in order to compute the equations of motion of multi-body systems as the one of the helicopter (see, for example, [96, Chapter 7]).

The equations of motion of the system are obtained from the Lagrange equation:

$$\frac{\mathrm{d}}{\mathrm{d}t}\left(\frac{\partial \mathcal{L}}{\partial \dot{q}}\right) - \frac{\partial \mathcal{L}}{\partial q} = \xi \tag{5.2}$$

where $\mathcal{L} = \mathcal{K} - \mathcal{U}$ is the Lagrangian function defined as the difference between the kinetic $\mathcal{K}$ and potential $\mathcal{U}$ energies, $q \in \mathbb{R}^n$ is the vector of the generalized coordinates, and $\xi \in \mathbb{R}^n$ is the vector of the generalized forces associated to q. In the case of our mechanical model, we select $q(t) = (\lambda(t), \varepsilon(t), \theta(t))$ (see Figure 5.2).

In general, for a mechanical system equation (5.2) can be written in the following standard form [96, Section 7.1.3]:

$$M(q)\ddot{q} + C(q,\dot{q})\dot{q} + R\dot{q} + g(q) = S(q)\tau \tag{5.3}$$

where $M(q)$ is a symmetric uniformly positive definite and uniformly bounded matrix representing the inertia of the system, $C(q,\dot{q})$ is a matrix associated to the Coriolis and centrifugal terms. R is a diagonal matrix of viscous friction coefficients, $g(q)$ represents the gravitational term, $S(q)$ is an $n \times m$ actuation matrix that maps the real input forces of the system $\tau \in \mathbb{R}^m$ into the generalized forces ξ.

In our case, we choose as τ as a combination of the input forces f_1 and f_2 exerted by the propellers (see Figure 5.2):

$$\tau := \begin{bmatrix} f_s \\ f_d \end{bmatrix} := \begin{bmatrix} f_1 + f_2 \\ f_1 - f_2 \end{bmatrix}. \tag{5.4a}$$

This choice allows us to obtain a more compact input matrix $S(q)$ and, as clarified in the following, it is more convenient during the control synthesis.

For the sake of conciseness, we report here only the terms R, $g(q)$, and $S(q)$, since the full $M(q)$ and $C(q,\dot{q})$ are very complex and not necessary for the derivation below:

$$R := \begin{bmatrix} r_\lambda & 0 & 0 \\ 0 & r_\varepsilon & 0 \\ 0 & 0 & r_\theta \end{bmatrix}, \tag{5.4b}$$

$$g(q) := \begin{bmatrix} 0 \\ \frac{g}{l_1}\sin(\varepsilon)(d_1 l_2 (m_2 + m_3) + d_2 l_1 m_3 \cos(\theta)) \\ g d_2 m_3 sin(\theta)\cos(\varepsilon) \end{bmatrix}, \tag{5.4c}$$

$$\begin{aligned} S(q) := & \underbrace{\begin{bmatrix} -l_2\cos(\varepsilon)\sin(\theta) & 0 \\ l_2\cos(\theta) & 0 \\ 0 & l_3 \end{bmatrix}}_{:=S_1(q)} + \\ & + \underbrace{\begin{bmatrix} k_{\gamma f}\cos(\varepsilon)\cos(\theta) & l_3\sin(\varepsilon) \\ k_{\gamma f}\sin(\theta) & 0 \\ 0 & 0 \end{bmatrix}}_{:=S_2(q)}, \end{aligned} \tag{5.4d}$$

where we emphasize the peculiar structure of the two terms S_1 and S_2 in the expression of $S(q) := S_1(q) + S_2(q)$ in (5.4d). This structure is motivated by the fact that we will consider $S_2(q)$ acting on the system as a bounded-time-varying disturbance, which will be neglected in the reduced complexity model. This results into having a decoupled input action on the λ-ε and on the θ dynamics. Even if the derivation described here follows a standard approach, the peculiar form of the entries in equation (5.3), (5.4) is somewhat new and reveals the dynamical structure of the considered setup, in particular the peculiar structure of the input matrix $S(q)$.

5.3.2 Model reduction

The novel control model that we are going to introduce is a simplified version of the full equations of motion (5.3), (5.4) of the mechanical model presented in Section 5.2, where some terms are neglected after some assumptions. In particular, the following assumptions are made.

Assumption 5.1. *The inertial coupling effects are neglected, and the diagonal part of $M(q)$ is constant or slowly varying. Moreover, the Coriolis and centrifugal term $C(q, \dot{q})\dot{q}$ is neglected.*

We make this assumption because the terms $M(q)$ and $C(q, \dot{q})$ are the most convoluted ones and their contribution is not fundamental for reproducing the relevant part of the dynamical behavior of the helicopter, as confirmed later in the chapter. Assumption 5.1 turns into having a diagonal and constant inertia matrix M and not having the $C(q, \dot{q})\dot{q}$ into the control model. Based on these assumptions, the following control model is obtained:

$$\ddot{q} = M^{-1}\left(-g(q) - R\dot{q} + S_1(q)\tau\right) \tag{5.5a}$$

where

$$M := \begin{bmatrix} j_\lambda & 0 & 0 \\ 0 & j_\varepsilon & 0 \\ 0 & 0 & j_\theta \end{bmatrix}, \tag{5.5b}$$

and j_i, $i \in q$ are constant parameters to be identified.

As one can notice, the control model (5.4), (5.5) preserves the full gravitational term $g(q)$ and a part of the input matrix $S(q)$ of the mechanical model, at the cost of neglecting the complex terms of the inertial coupling between the different *dof*, the fictitious forces contained in the $C(q, \dot{q})$ term, and a part of the input matrix, which is considered to act on the system as a limited-time-varying disturbance. Even with these simplifications, in the following sections it will be shown that the relevant dynamical behavior of the helicopter is retained.

Model (5.4), (5.5) will be tuned with a system identification procedure in order to reproduce as well as possible the helicopter dynamics.

Hereafter, we rearrange the equations of the control model (5.4), (5.5) collecting the physical parameters into a set of non-redundant parameters to be identified.

$$\ddot{q} = -\overline{g}(q) - \overline{R}\dot{q} + \overline{S_1}(q)\tau \tag{5.6a}$$

where

$$\overline{g}(q) := M^{-1}g(q) = \begin{bmatrix} 0 \\ \sin(\varepsilon)(a_{\varepsilon 1} + a_{\varepsilon 2}\cos(\theta)) \\ a_\theta \cos(\varepsilon)\sin(\theta) \end{bmatrix}, \tag{5.6b}$$

$$\overline{R} := M^{-1}R = \begin{bmatrix} c_\lambda & 0 & 0 \\ 0 & c_\varepsilon & 0 \\ 0 & 0 & c_\theta \end{bmatrix}, \tag{5.6c}$$

$$\begin{aligned} \overline{S_1}(q) :&= M^{-1}S_1(q) = \begin{bmatrix} -b_\lambda \cos(\varepsilon)\sin(\theta) & 0 \\ b_\varepsilon \cos(\theta) & 0 \\ 0 & b_\theta \end{bmatrix} = \\ &= \underbrace{\begin{bmatrix} -b_\lambda \cos(\varepsilon) & 0 & 0 \\ 0 & b_\varepsilon & 0 \\ 0 & 0 & b_\theta \end{bmatrix}}_{:=T(\varepsilon)} \underbrace{\begin{bmatrix} \sin(\theta) & 0 \\ \cos(\theta) & 0 \\ 0 & 1 \end{bmatrix}}_{:=B(\theta)}. \end{aligned} \tag{5.6d}$$

The factorization of the input matrix $\overline{S_1}(q) = T(\varepsilon)B(\theta)$ will be useful for the synthesis of the control law proposed in the following.

We thus obtain the following equations of motion:

$$\begin{aligned} \ddot{\lambda} &= -c_\lambda \dot{\lambda} - b_\lambda \cos(\varepsilon)\sin(\theta) f_s \\ \ddot{\varepsilon} &= -a_{\varepsilon 1}\sin(\varepsilon) - a_{\varepsilon 2}\sin(\varepsilon)\cos(\theta) - c_\varepsilon \dot{\varepsilon} + b_\varepsilon \cos(\theta) f_s \\ \ddot{\theta} &= -a_\theta \cos(\varepsilon)\sin(\theta) - c_\theta \dot{\theta} + b_\theta f_d \end{aligned} \tag{5.6e}$$

whose state is $q = (\lambda, \varepsilon, \theta)$ with $\dot{q}$, and whose input is $\tau = (f_s, f_d)$. It is worth to point out that the factorization of the parameters of model (5.4), (5.5) into the redundant parameters of (5.6) is not a reversible relationship, but it makes sense in a system identification procedure viewpoint as it will be commented in Section 5.4.

5.4 IDENTIFICATION

In this section we describe the identification procedure followed in order to estimate the models parameters. A "gray-box model estimation" paradigm has been followed, in which the goal is the estimation of the model parameters of a known model. As outlined in Section 5.2, in the experimental setup the input forces are generated by applying a voltage to each motor-propeller assembly. In the following subsection, the relation between the applied voltages and the exerted forces will be identified.

5.4.1 Input nonlinearity

Consider a τ in (5.4a) such that $f_d = 0$ and consider that the two motor-propeller assemblies are equal. Under these conditions, we can state that

$$f_s = h(v_s) \tag{5.7}$$

where $v_s = v_1 + v_2$ is the total voltage applied to the motors, and h is an unknown function that maps the total voltage v_s into the thrust f_s. Consider now the elevation dynamics in equation (5.6) at some equilibrium, with $\theta = 0$, and with a constant input $f_s = h(v_s)$:

$$-a_{\varepsilon 1} \sin(\varepsilon_{ss}) + b_\varepsilon h(v_s) = 0 \tag{5.8}$$

By applying n different voltages $v_{s,k}$ $k \in \{1 \dots n\}$ spanning the allowed range $[-10, 10]$V ($[-5, 5]$V for each motor), it is possible to take n samples of a scaled version $\widetilde{h}$ of function h (and therefore a scaled version $\widetilde{f_s}$ of the thrust f_s) by observing the resulting steady state condition $\varepsilon_{ss,k}$:

$$\widetilde{f_s} := \widetilde{h}(v_s) := c\, f_s = c\, h(v_s) = \sin(\varepsilon_{ss}) \tag{5.9}$$

The voltage to be applied to a motor in order to exert a desired scaled force $\widetilde{f_i}$ can be then computed as:

$$v_i = \frac{1}{2}\widetilde{h}^{-1}(\widetilde{f_i}) \,, \tag{5.10}$$

with $i \in \{1, 2\}$. Since we are identifying a scaled version of the thrust, we include as well a normalization procedure, such that the maximum applicable scaled force $\widetilde{f_i}$, $i \in \{1, 2\}$ corresponds to 1. Based on some experimental evidences and intuitions, $\widetilde{h}(v_s)$ has been selected to be a locally quadratic and globally linear function based on the following piecewise description:

$$\widetilde{h}(v_s) := \begin{cases} p_2^- v_s + p_3^- & \text{if} \quad v_s \leq v_{sn} \\ p_1^- v_s^2 & \text{if} \quad v_{sn} \leq v_s \leq 0 \\ p_1^+ v_s^2 & \text{if} \quad 0 \leq v_s \leq v_{sp} \\ p_2^+ v_s + p_3^+ & \text{if} \quad v_{sp} \leq v_s \end{cases}, \tag{5.11}$$

where v_{sn} and v_{sp} represents threshold values specified below. This particular choice can be justified observing that the transfer function of a DC-motor is such that in steady state conditions the rotational speed depends linearly on the applied voltage and on the applied load torque. Then for a DC-motor with a propeller connected on its shaft, since both the thrust ad the aerodynamic load torque exerted by the propeller depend quadratically on the rotational speed, a linear relation between the voltage applied to the DC-motor and the thrust exerted by the propeller is expected. Nevertheless, at slow rotational speed the aerodynamic load torque is negligible, and a quadratic dependence between the thrust and the voltage emerges.

A least square procedure has been then applied to identify the parameters of function (5.11), in order to best fit the experimental samples. C^1 continuity

constraints of function (5.11) have been imposed during the optimization procedure. The threshold values v_{sn} and v_{sp} have been manually selected based on the measured points. The numerical values are reported in Table 5.1. In Figure 5.3 both the experimental samples and the fitted function are depicted. Note that the function is non symmetric due to the propellers shape.

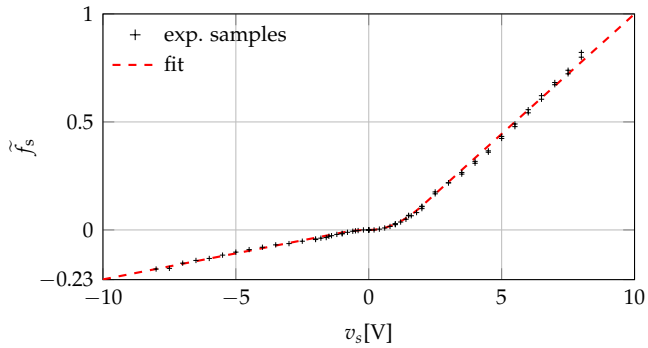

Figure 5.3: Input nonlinearity relation within the domain $[-10, 10]$V of the voltage input v_s.

Due to the fact that a scaled version of the forces $\widetilde{f}_s$ has been identified, we introduce the scaled input $\widetilde{\tau}$ acting on model (5.6) defined as:

$$\widetilde{\tau} = c\tau. \tag{5.12}$$

Due to this scaling, we will identify a scaled version of the input parameters of the control model b_λ, b_ε, b_θ, taking into account the scaling factor, i.e. $\widetilde{b}_\lambda = b_\lambda/c$, $\widetilde{b}_\varepsilon = b_\varepsilon/c$, $\widetilde{b}_\theta = b_\theta/c$.

5.4.2 Identification of the models parameters

Once the relation between the scaled version of the forces exerted by the two motor-propeller assemblies has been identified, the estimation of the model parameters can be faced. The identification procedure is based on a "gray-box" paradigm, both for the mechanical model and the control model, as detailed next.

5.4.2.1 *Identification of the control model*

For the control model the "gray-box" identification has been carried out using *MATLAB* `idnlgrey` and `pem` tools, due to their suitability for identifying nonlinear systems. Firstly, the free motion of the ε-θ dynamics has been identified. This permits to have an estimate for the parameters of the autonomous part of the ε-θ dynamics in equation (5.6), i.e. $a_{\varepsilon 1}$, $a_{\varepsilon 2}$, c_ε, a_θ, c_θ. To this end, experiments with initial elevation and pitch angle different form zero and no voltages applied to the motors have been carried out. The parameters estimation resulting from this first identification procedure has then been used as a

parameter	c_λ	$\widetilde{b}_\lambda$	$a_{\varepsilon 1}$	$a_{\varepsilon 2}$	c_ε	$\widetilde{b}_\varepsilon$
value	0.274	0.257	2.356	0.799	0.053	0.565
unit	$\frac{1}{s}$	$\frac{1}{s^2}$	$\frac{1}{s^2}$	$\frac{1}{s^2}$	$\frac{1}{s}$	$\frac{1}{s^2}$
parameter	a_θ	c_θ	$\widetilde{b}_\theta$	p_1^-	p_2^-	p_3^-
value	0.858	0.048	7.340	-0.012	0.024	0.012
unit	$\frac{1}{s^2}$	$\frac{1}{s}$	$\frac{1}{s^2}$	$\frac{1}{V^2}$	$\frac{1}{V}$	-
parameter	p_1^+	p_2^+	p_3^+	v_{sn}	v_{sp}	
value	0.028	0.111	-0.111	-1	2	
unit	$\frac{1}{V^2}$	$\frac{1}{V}$	-	V	V	

Table 5.1: Control model identified parameters.

warm-start for the identification of the full motion. Forced experiments have been performed with input voltages consisting in a combination of steps in $\widetilde{f}_s$ and $\widetilde{f}_d$ applied to the helicopter. The resulting parameters estimation for the control model are reported in Table 5.1.

5.4.2.2 *Identification of the mechanical model*

The identification of the mechanical model is more delicate than the one of the control model. First of all, there are more parameters to be identified. In addition to the lengths, masses and friction coefficients, there are the constant $k_{\gamma f}$ in equation (5.1) generating the aerodynamic drag torques, and the constant c in equation (5.12) needed to generate the real forces starting from the scaled forces. Secondly, the mechanical model is computationally heavier to be simulated. Moreover, there exist more than one realization of the mechanical model that produce the same responses of the experimental setup. Indeed, the same inertia properties can be achieved with infinitely many combinations of lengths and masses. For this reason, and in order to remove some degrees-of-freedom during the identification process, the length parameters l_1, l_2 and l_3 have been constrained to be similar to the ones of the real experiment. The experimental data used to tune the mechanical model are the same used to identify the control model. An initial manual tuning has been performed in order to fit as close as possible the free motion. Then, starting from this first tuning, an optimization procedure has been launched in order to refine the parameters with the aim of minimizing the root mean square (RMS) of the difference between the responses of the mechanical model with respect to the experimental responses. To this end, the *MATLAB* functions `lsqnonlin` and `ga` have been used, due to their flexibility and the good exploration properties of the genetic algorithm. The resulting parameters estimation for the mechanical model are reported in Table 5.2.

Figures 5.4 and 5.5 at page 79 and 80 compare experimental data (real flight, solid gray) with simulation runs of the identified control model (dashed red) and of the identified mechanical model (dash-dotted blue). In particular, Figure 5.4 shows experiments and simulations with the input signal used

parameter	l_1	l_2	l_3	d_1	d_2	m_2
value	0.520	0.650	0.180	0.192	0.003	1.00
unit	m	m	m	m	m	kg
parameter	m_3	r_λ	r_ε	r_θ	$k_{\gamma f}$	c
value	0.771	0.250	0.050	0.003	-0.067	1.272
unit	kg	Nms	Nms	Nms	m	Nm

Table 5.2: Mechanical model identified parameters.

for the two identifications. Figure 5.5 shows the corresponding curves with validation input signal not used for the identification.

Below each plot, a table reports the RMS of the difference between the experimental data and the models responses. From these tables it is possible to notice that in the case of the identification set, the mechanical model performs better than the control model, as expected. Except for the λ *dof*, this trend is present in the validation set as well. With regard to the λ *dof*, some observation can be done to justify the mismatch in the responses. Consider firstly the λ responses after 20s. Except for a rigid translation, here the trend of both the control model and the mechanical model are similar to the real one, with more detail fidelity produced by the mechanical model. The big difference is in the motion accumulated during the responses before 20s. This mismatch can be justified by considering that the λ dynamics is such that a non constant solution can only be experienced with a nonzero input. This makes the identification procedure of the λ *dof* harder and even a slight presence of dry friction can influence the response. Nevertheless, it will be shown that the closed-loop responses are such that this mismatch is compensated by the stabilizing controller.

5.5 EXPERIMENTAL VALIDATION AND COMPARISON

This section focuses on the comparison between the reduced complexity model introduced in equation (5.6) and other control oriented models from the literature dealing with the *Quanser* experimental system considered here [83]. From the vast literature on this experimental setup, we chose for our comparisons a selection of models used in some of the most cited references.

Indeed, despite the presence of many reduced complexity models of the 3-DOF helicopter in the literature (for example [64], [29], [80], [56], and [106]), the control model (5.6) is somewhat new and better justified than the existing ones, while preserving their core structure. In particular, in the reduced complexity model proposed in [64], the authors take into account a Coriolis contribution in the ε *dof*, while in [80] a variant of the input matrix is considered. In [29] and [56] slightly different input and gravitational effects are considered, while in [106] another different version of reduced-complexity model is taken into account. As a result, the reduced complexity models of the above works are simpler than the one proposed here but there is no clear link between the standard Lagrangian model discussed in Section 5.3.1 and those reduced models. Conversely, the control model (5.6) is more justifiable due to its clear

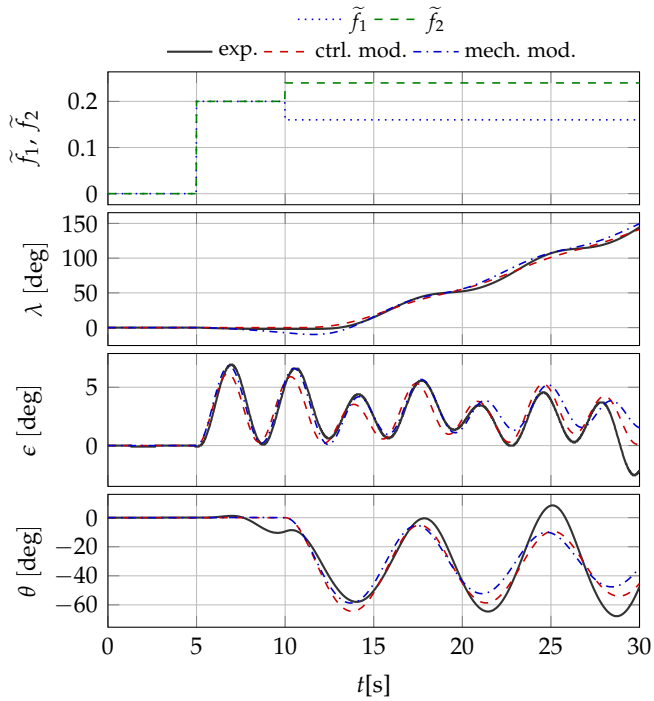

dof	RMS mechanical model	RMS control model
λ	2.805°	4.297°
ε	0.913°	1.070°
θ	6.835°	8.680°

Figure 5.4: Identification result of the mechanical and control model.

and strong link with the Lagrangian representation of the equation of motion of the helicopter's mechanical model (5.3), (5.4).

We now proceed in comparing our model with the open-loop behaviors of the control-oriented models of [64], [29], [80], [56], and [106], using the experimental responses coming from real flights as ground truth reference. Each one of the considered control oriented models has been rewritten in order to match with the *dof* and actuation convention adopted here, and has undergone a gray-box parameter identification procedure, as described in Section 5.4. The same identification and validation datasets as those considered in Section 5.4 have been used. We will refer to the model in [64] as "Liu2014", to the one in [29] as "Chriette2016", to the one in [80] as "Peaucelle2011", to the one in [56] as "Kiefer2010", and to the one in [106] as "Zheng2011".

In Table 5.3, similar to the tables below Figures 5.4 and 5.5, we report the RMS of the difference between the experimental data and the responses of the five analyzed models from the literature, together with the one proposed in this work, when using the validation dataset. In Figure 5.6 at page 81, a plot of the compared responses is depicted, where the black dotted curves represent

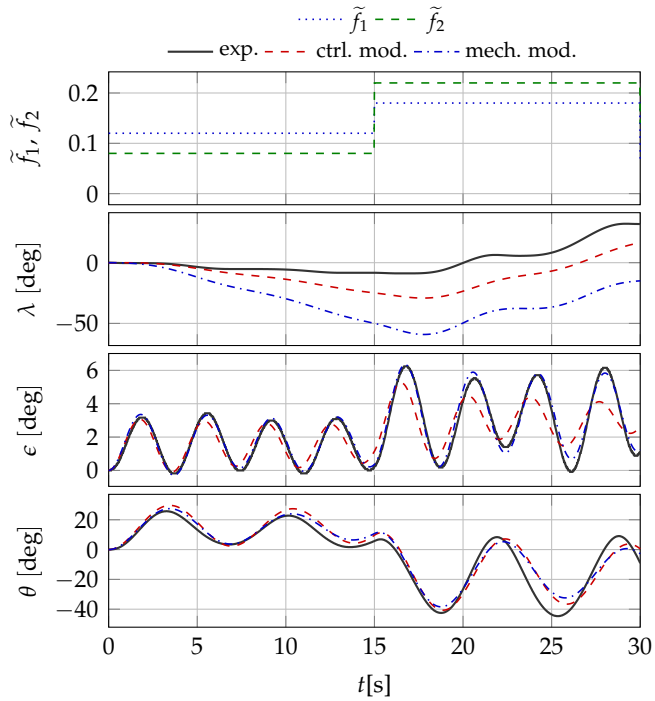

dof	RMS mechanical model	RMS control model
λ	36.723°	14.704°
ϵ	0.268°	0.897°
θ	5.749°	5.947°

Figure 5.5: Validation result of the mechanical and control model identification.

the experimental response, and the other curves follow the color code reported above the figure.

The last column in Table 5.3 reveals that our model is overall the most accurate one, even if there are some models that perform better if focusing only on the ϵ *dof*. This is probably due to the fact that that models are ϵ-focused. The overall better performances of our model may be explained by the clear physical link we followed (explained in Section 5.3.2), taking more fairly into account all *dof*, whereas some of the other models have not been derived with the same spirit. Furthermore, it is worth to point out that the control models "Chriette2016" and "Zheng2011" do not involve terms allowing to represent the oscillation phenomena of the θ-*dof* in the open loop response (see bottom plot of Figure 5.6).

model	λ-*dof*	ε-*dof*	θ-*dof*	mean
this work	14.704°	0.897°	5.947°	7.183°
Liu2014	35.997°	0.525°	9.117°	15.213°
Chriette2016	132.406°	1.648°	36.782°	56.945°
Peaucelle2011	15.272°	0.521°	9.106°	8.300°
Kiefer2010	30.544°	0.652°	7.688°	12.961°
Zheng2011	47.300°	1.543°	36.021°	28.288°

Table 5.3: Literature control models performances comparison, RMS of the difference between the model responses and the experimental data.

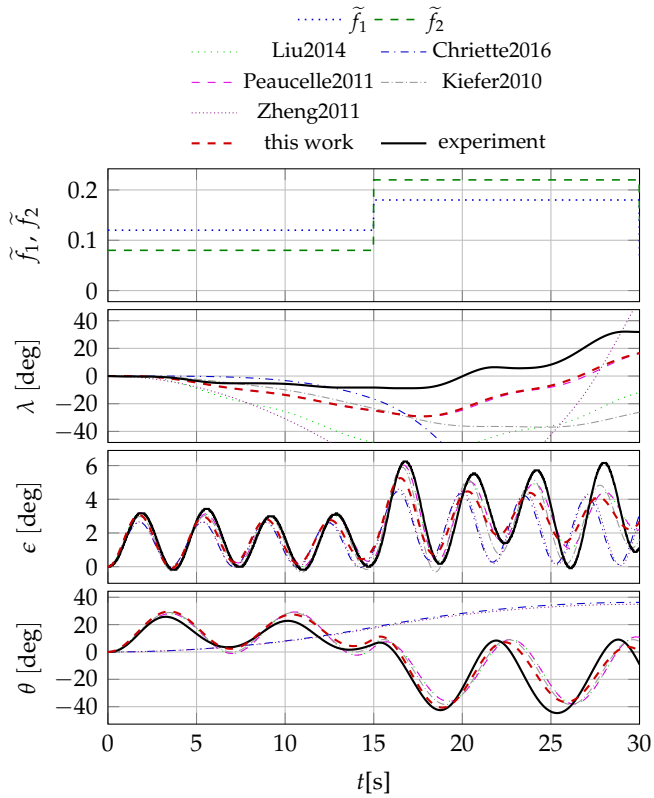

Figure 5.6: Comparison result of the control model here proposed, experimental response (real flight), and former reduced complexity model present in literature.

5.6 FEEDBACK LINEARIZATION CONTROL DESIGN

In this section, a standard feedback linearization based control algorithm will be developed for the Quanser *"3 DOF Helicopter"*. The synthesis of such a control law for the underactuated plant (5.6) is based on a time scale separation paradigm, where the travel λ and the elevation ε are treated as the slow dy-

namics, the pitch θ as faster than the latter two *dof*, and the neglected propeller dynamics between the commanded thrust (requested by the controller) and the exerted control input τ as the fastest quantity.

The controlled *dof* are the travel λ and the elevation ε, to which we will refer as $q_c := (\lambda, \varepsilon)$. The corresponding reference $q_{cr} := (\lambda_r, \varepsilon_r)$ is constant.

Firstly, we derive a feedback linearization control which relies on a virtual input $\nu \in \mathbb{R}^3$. Then, a reference value θ_r for the pitch angle and the input τ are selected in such a way to match the virtual input.

5.6.1 Feedback linearization

Considering q_{cr} as the constant reference for the controlled *dof* $q_c = (\lambda, \varepsilon)$, we define the tracking error as:

$$\widetilde{q} := \begin{bmatrix} q_c - q_{cr} \\ \theta - \theta_r \end{bmatrix} \tag{5.13}$$

Following a feedback linearization paradigm, we would like the dynamics of the mismatch $\widetilde{q}$ to behave like three decentralized damped oscillators, therefore we impose the following dynamics:

$$\dddot{\widetilde{q}} = \dddot{q} = -\Xi\ddot{\widetilde{q}} - \Omega^2\dot{\widetilde{q}} = -\Xi\ddot{q} - \Omega^2\dot{\widetilde{q}} \tag{5.14a}$$

where

$$\Omega := \operatorname{diag}(\omega_\lambda, \omega_\varepsilon, \omega_\theta)\,, \tag{5.14b}$$

$$\Xi := 2\operatorname{diag}(\zeta_\lambda\omega_\lambda, \zeta_\varepsilon\omega_\varepsilon, \zeta_\theta\omega_\theta)\,, \tag{5.14c}$$

and $\zeta_i > 0$, $\omega_i > 0$, $i \in \{\lambda, \varepsilon, \theta\}$ are tuning parameters and represent respectively the damping terms ζ_i and the natural frequency ω_i of the artificial damped oscillator dynamics. We now proceed in substituting equation (5.14a) into the underactuated plant dynamics (5.6a), which for the sake of clarity is here recalled

$$\ddot{q} + \overline{g}(q) + \overline{R}\dot{q} = T(\varepsilon)B(\theta)\tau \tag{5.15}$$

Substituting equation (5.14a) in (5.15) it is possible to compute the virtual control action ν needed in place of $B(\theta)\tau$ in order to make the mismatch dynamics behave as specified in (5.14a):

$$\nu := T^{-1}(\varepsilon)\left(\overline{g}(q) - \Omega^2\widetilde{q} - (\Xi - \overline{R})\dot{q}\right) + \nu_{\text{ff}}\,, \tag{5.16}$$

noting that $T(\varepsilon)$ defined in (5.6d) is diagonal and invertible thanks to the fact that $\cos(\varepsilon) > 0$ due to the constraint on the elevation *dof* in the real experiment: $\varepsilon \in [-15°, 15°]$. In (5.16) we introduced a feedforward term $\nu_{\text{ff}} := (\nu_{\lambda\text{ff}}, 0, 0)$ as a constant steady-state compensation acting on the first component of ν. This term improves the steady state tracking performance of the λ *dof* by compensating for the disturbance produced by the (1,1)-element of matrix

$S_2(q)$ in equation (5.4d). Note that the $\cos(\varepsilon)$ term present in the (1,1)-element of matrix $S_2(q)$ is matches with the same term in the matrix $T(\varepsilon)$ that multiplies the virtual input ν.

With the above equation, we introduced the idea of using ν as a virtual input in order to make the underactuated system behave as a linear system. We now proceed in manipulating the virtual input in order to obtain the real input. We will compute an input τ and a reference value for the pitch dynamics θ_r in such a way that the real applied input produces an effect as close as possible to the desired one.

5.6.2 The virtual input

We would like $B(\theta)\tau$ to be as close as possible to the computed virtual input $\nu = (\nu_\lambda, \nu_\varepsilon, \nu_\theta)$ in equation (5.16). Considering the slow dynamics as constant, we define the mismatch between the desired virtual input and the applied virtual input:

$$\eta := \nu - B(\theta)\tau\,, \tag{5.17}$$

and the following objective function:

$$\begin{aligned} J(\theta,\tau) &:= \|\eta\|^2 = \|\nu - B(\theta)\tau\|^2 \\ &= \nu^\top\nu - 2\nu^\top B(\theta)\tau + \tau^\top\tau \end{aligned} \tag{5.18}$$

where we used that $B^\top(\theta)B(\theta) = I$. Consider therefore the following minimization problem:

$$\underset{\theta,\tau}{\operatorname{argmin}}\, J(\theta,\tau)\,. \tag{5.19}$$

The fact that the two optimization variables θ and τ belong to two different time scales suggests to solve the optimization problem (5.19) in two different steps: first, a desired value for the pitch (the slow quantity) is computed:

$$\theta^* := \underset{\theta}{\operatorname{argmin}}\, J(\theta,\tau) = \arctan\left(\frac{\nu_\lambda}{\nu_\varepsilon}\right)\,, \tag{5.20}$$

then, the optimal value for τ for a general $\theta = \bar\theta$ is derived:

$$\begin{aligned} \tau^* := \underset{\tau}{\operatorname{argmin}}\, J(\bar\theta,\tau) &= B^\top(\bar\theta)\nu = \\ &= \begin{bmatrix} \nu_\lambda \sin(\bar\theta) + \nu_\varepsilon\cos(\bar\theta) \\ \nu_\theta \end{bmatrix}. \end{aligned} \tag{5.21}$$

The resulting τ^* comes from basic computations, being $J(\theta,\tau)$ convex in τ. The result θ^* is as well simply derived and it is unique modulo 2π if $\tau_1 \neq 0$. Otherwise every value of θ zeroes out $J(\theta,\tau)$. We select the reference setpoint θ_r and the input τ as the optimal ones:

$$\theta_r = \theta^*\,,\quad \tau = \tau^*\,. \tag{5.22}$$

As one can notice, θ^* (and thus θ_r) depends on ν_λ and ν_ε. Therefore, the control scheme can be applied as follows. Firstly, the first two component of (5.16) are computed in order to get ν_λ and ν_ε (note that (5.16) represents 3 independent equations). Secondly, θ_r is computed thanks to (5.20), which allows us to compute ν_θ with the third component of (5.16). Finally, τ is computed from (5.21).

5.6.3 State estimation

The feedback linearization control law proposed in equation (5.16) relies on the knowledge of both the *dof* position q and on the *dof* velocity $\dot{q}$. As discussed in Section 5.2, the experimental setup is equipped with an encoder at each one of the three joints, which supplies a quantized measure with a resolution of 0.0015 rad. Therefore only piecewise constant position measurements are available. In this work, we follow an indirect approach where $\dot{q}$ has been estimated using the high-gain observation law proposed in [76] (see also [28] for the use of high-gain observers to estimate time derivatives). In particular, if we denote by x the collection of q and $\dot{q}$

$$x := (q, \dot{q}) \in \mathbb{R}^6 \tag{5.23}$$

and if with $\hat{x}$ we refer to the estimate of x

$$\hat{x} := \left(\hat{q}, \hat{\dot{q}}\right) \in \mathbb{R}^6\,, \tag{5.24}$$

the estimator dynamics is given by

$$\dot{\hat{x}} = \begin{bmatrix} 0 & I \\ 0 & 0 \end{bmatrix} \hat{x} + \begin{bmatrix} k_p E^{-1} \\ k_v E^{-2} \end{bmatrix} (q - \hat{q})\,, \tag{5.25}$$

where matrix $E \in \mathbb{R}^{3\times 3}$ is a positive definite diagonal matrix containing the three decoupled high-gain scaling factors

$$E = \mathrm{diag}(\varepsilon_\lambda, \varepsilon_\varepsilon, \varepsilon_\theta)\,, \tag{5.26}$$

and $k_p\, k_v$ are two positive scalars such that the characteristic equation $s^2 + k_v s + k_p = 0$ has roots with negative real part. The three high-gain scaling factors ε_i, $i \in q$ are design parameters that can be conveniently adjusted in order to obtain a trade-off between smoothening action and reduction of the time lag of the estimator. Moreover, the smoothing action of the proposed approach mitigates the effect of the quantized position measurements. For these reasons, the control loop is in feedback from the estimated state $\hat{x}$.

5.7 CLOSED-LOOP EXPERIMENTS

In this section we discuss and compare the results obtained interconnecting a realization of the control scheme proposed in Section 5.6 to both the simulation platform and the experimental setup. Simulation results are obtained thanks to the mechanical model discussed in Section 5.2.

parameter	ω_λ	ω_ε	ω_θ	ζ_λ	ζ_ε	ζ_θ
value	0.37	1.60	2.80	0.80	0.60	0.90
parameter	ε_λ	ε_ε	ε_θ	$\nu_{\lambda \mathrm{ff}}$		
value	0.10	0.10	0.05	-0.08		

Table 5.4: Controller and state estimator tuning.

A tuning process of the controller parameters has been carried out in order to obtain desirable evolutions. In particular, the natural frequencies in Ω have been chosen in such a way to respect the time scale separation discussed before, and in order to not reach the actuator limits in standard transient, while the damping parameters in Ξ have been chosen in such a way to obtain desirable transients with a slightly overshooting behavior. The presented results have been obtained using the same controller settings in both the experiment and the simulation. The used settings are reported in Table 5.4.

The testing scenarios consist of a reference for the λ *dof* composed by a sequence of steps between $-90°$, $0°$, and $90°$, to be performed at a fixed constant reference for the ε *dof*. In particular, two experiments are presented, the first with $\varepsilon_r = 10°$, and the second one with $\varepsilon_r = 10°$. The results are reported in Figure 5.7.

Let us start discussing the case with $\varepsilon_r = 10°$, depicted in Figure 5.7a. Observing the responses, we can claim that the proposed control algorithm succeeds in the stabilization and set-point regulation of the helicopter, producing a graceful evolution to the desired set-point. The step response of the λ *dof* exhibits the typical response of an over-critically damped oscillator, showing a non-overshooting behavior. A good tracking performance is present in the θ *dof* as well, while ε seems to be the most problematic *dof*. This is probably due to the disturbances produced by the term $S_2(q)$ in equation (5.4d), which has been neglected in the control model.

Moving to the experimental test with $\varepsilon_r = 13°$, depicted in Figure 5.7b, similar considerations can be made. Observing the figure, it is possible to note that due to a larger value of ε_r in the fourth plot, the θ_r evolution in the fifth plots is in general smaller than in the two other cases. This is due to the fact that a larger ν_ε is needed to track a larger ε_r. This turns into having a smaller argument in the arctangent function in equation (5.20). Nevertheless, a larger ν_ε produces a larger $\widetilde{f}_s$, which amplifies the disturbance effect due to the neglected term $S_2(q)$ in equation (5.4d) (in particular due to the (1,2)-element). Indeed a larger tracking error of the ε *dof* is present in this case. Moreover, looking at the two upper plots it is possible to notice that a larger value of $\widetilde{f}_s$ turns into larger mean values of the two forces $\tilde{f}_1$ and $\tilde{f}_2$ than in the other cases, but the smaller θ_r in the fourth plot is such that smaller peaks are present.

As an overall comment, it is possible to see that in general the simulation response matches well the experimental response, confirming that the proposed mechanical model is a good software-in-the-loop platform for testing and synthesizing control algorithms for the Quanser *"3 DOF Helicopter"* experiment. The most problematic degree-of-freedom is the ε-*dof*, where the largest deviations between the experimental and the simulated responses are present.

These deviations are probably caused by aerodynamics disturbances induced by tables and walls nearby the experimental setup, and by the actuators dynamics (DC-motor/propeller assemblies), which have not been included in our model. Still, the proposed mechanical model shows to capture the most important dynamical behavior of the Quanser *"3 DOF Helicopter"*.

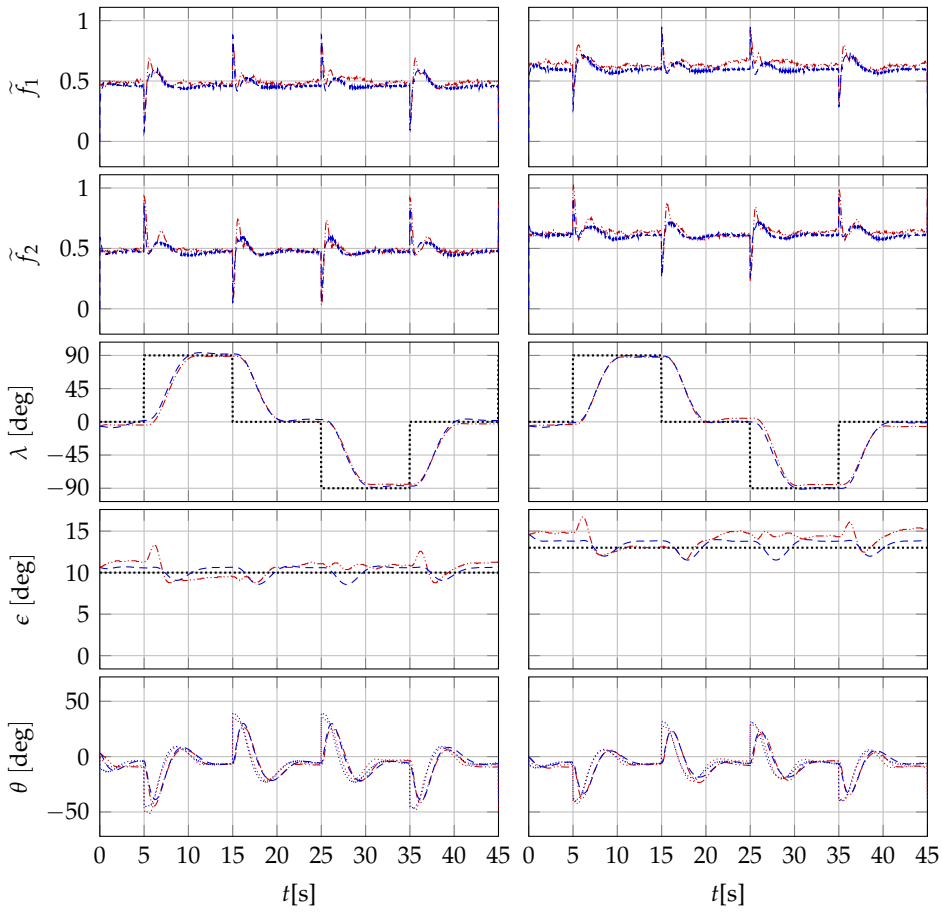

(a) Travel steps at $\varepsilon_r = 10°$. **(b)** Travel steps at $\varepsilon_r = 13°$.

Figure 5.7: Experimental and simulation result in closed loop. Dotted curves: references. Blue dashed curves: simulation with the mechanical model. Red dot-dot-dashed curves: experiment (real flight).

6 VALIDATION OF THE RTSO CONTROLLER: TWO CASE STUDIES

This chapter focuses on validating the RTSO controller developed in Chapter 4 by means of its application to two case studies. Firstly, the RTSO controller will be validated on a real-time implementation on an experimental scenario with a propeller-actuated tilting arm. Secondly, the RTSO controller will be used for controlling the travel degree of freedom of the Quanser's 3 DOF Helicopter by means of the benchmark platform developed in Chapter 5.

6.1 THE ARM EXPERIMENT

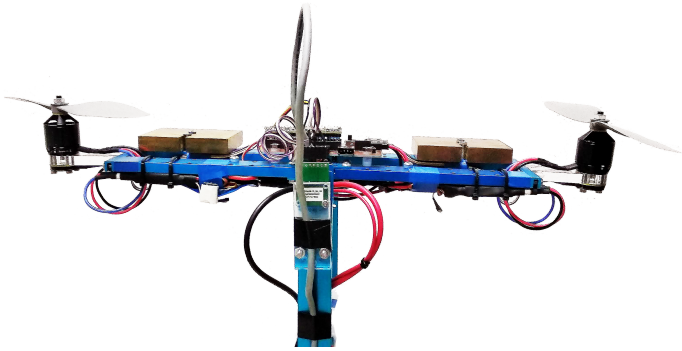

Figure 6.1: Picture of the arm experiment.

The first case study presented in this chapter is dubbed as "the arm experiment" and is depicted in Figure 6.1. It is essentially composed by a tilting arm that carries two motor-actuated propellers, realized with low-cost limited-performances hardware. The arm can tilt around the axis on which its center of gravity lies (even if not perfectly balanced), and the angle of the arm is measured by an AMS AS5048 Hall-effect absolute encoder. The propellers are actuated by a couple of brushless DC motors, which are driven by two Electronic Speed Controllers (ESC) that regulate the rotational speed of each motor shaft. The motors rotate in such a way that the propellers produce only upward thrusts. Two other AMS AS5048 encoders are mounted below each motor to read out the angular position of the motor's shafts. The experimental setup

is controlled via an embedded platform programmed via Target-Simulink, running a Simulink model at the frequency of 200Hz. The arm experiment input corresponds to the propellers rotational velocity reference, while the experiment output is the absolute angle of the arm around its tilting axis and the absolute angle of the motors shaft. Three real time realizations of the observer proposed in Chapter 7 are used in order to estimate the rotational velocity of the arm inclination and the propellers rotational velocities.

6.1.1 Mechanical model of the arm experiment

We now introduce a mathematical model representing the arm experiment. Figure 6.2 shows a schematic representation of the model. Since the arm

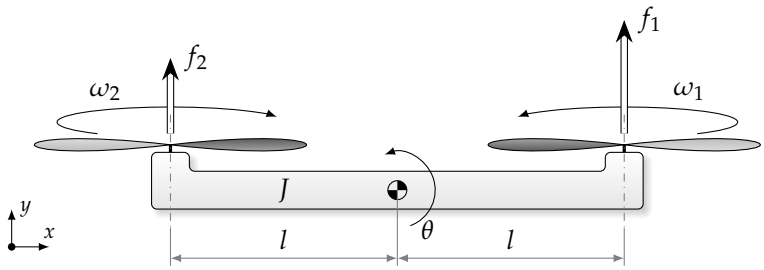

Figure 6.2: Schematic drawing of the arm experiment.

experiment is constrained to the x − y plane, we only consider the motion in this plane. The arm is modeled as a rigid body with inertia J and length $2l$ that can rotate of an angle θ around the axis passing trough its center of mass, therefore assuming perfect balancing. The propellers are modeled as two bodies with no inertia, spinning at $\omega_1 > 0$ and $\omega_2 > 0$ respectively, and exerting on the arm ends two upward forces $f_1 > 0$ and $f_2 > 0$. The thrust forces f_1 and f_2 exerted by the propeller can be modeled with a good level of accuracy as a quantity depending quadratically on the angular speed of the propellers themselves (see for example [26], [39], and Chapter 5), that is,

$$f_i = k_f \omega_i^2 , \quad i \in \{1, 2\} . \tag{6.1}$$

The equation of motion of the arm can therefore be written as

$$\ddot{\theta} = \frac{l}{J}(f_1 - f_2) = \frac{l k_f}{J}(\omega_1^2 - \omega_2^2) . \tag{6.2}$$

We now define a few auxiliary variables, which correspond to the sum and difference of the propeller velocities squared:

$$\begin{aligned} \Omega_s &:= \omega_1^2 + \omega_2^2 , \\ \Omega_d &:= \omega_1^2 - \omega_2^2 , \end{aligned} \tag{6.3}$$

from which the propeller rotational speeds can be retrieved as

$$\begin{aligned}\omega_1 &= \sqrt{\frac{1}{2}(\Omega_s + \Omega_d)}\,,\\ \omega_2 &= \sqrt{\frac{1}{2}(\Omega_s - \Omega_d)}\,.\end{aligned} \tag{6.4}$$

For practical convenience, the ω_i unit of measurement is selected to be kilo-revolutions-per-minute ([krpm]), and the Ω_d unit is consequently [krpm^2]. In order to guarantee that $\omega_i > 0$, Ω_s must always be larger than the absolute value of Ω_d. In light of definitions (6.3), model (6.2) can be rewritten as

$$\ddot{\theta} = \frac{lk_f}{J}\Omega_d =: b\Omega_d \tag{6.5}$$

where Ω_d plays the role of the actuator, being proportional to the torque applied to the arm, and parameter b is defined as the combination of physical parameters. A gray-box identification procedure leads to finding an approximate value of $b \approx 0.9 \frac{\text{rad}}{\text{s}^2\text{krpm}^2}$. It is worth to point out that in this experiment we only have availability of an estimated value of the actuator value Ω_d, since it is a function of the estimated propellers rotational velocity. The role of Ω_s, even if not appearing in the arm dynamics, is to set the average propellers rotational speed.

We now proceed to analyzing the dynamical behavior of the actuator Ω_d.

6.1.2 Actuator modeling

We are interested in developing a simple actuator model. To this end, let γ be the desired value to be exerted by the actuator Ω_d. Figure 6.3 reports some experiments in which the initial Ω_d is zero (solid curve), γ is zero before zero time, and assumes different constant values afterwards (dotted curves). During the experiment, a value of $\Omega_s = 10$ has been used. Observing the dynamical link between γ and Ω_d, we can see that, after a pure time delay, Ω_d converges to γ with a non oscillating, non overshooting transient, and the static gain is approximately one. It is as well clear that, the larger the reference γ, the longer is the rising time of Ω_d. Nevertheless, since we are interested in a simple actuator model, we consider an average rising time of approximately 0.3 s. The proposed model consists then of a single real negative pole with rising time of 0.3 s, that is,

$$\dot{\Omega}_d = a(\gamma - \Omega_d) \tag{6.6a}$$

with

$$a = \frac{5}{0.3} \approx 16.6\,\frac{1}{\text{s}}\,. \tag{6.6b}$$

For the sake of comparison, in Figure 6.3 we reported the simulated actuator response generated by model (6.6) with a dashed line. In the following sections, we will see that, even if the considered actuator model is simplistic, this will be enough to get desirable responses for the interconnection between the RTSO controller and the arm experiment.

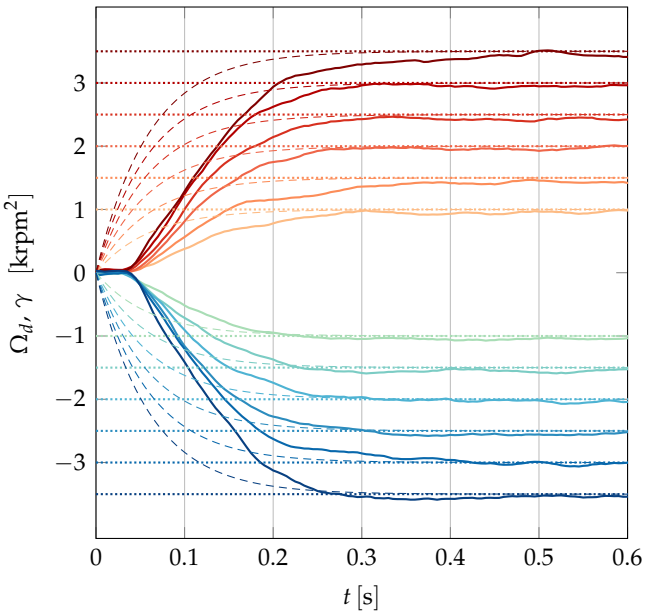

Figure 6.3: Dynamical behavior of the actuator Ω_d. Solid curves: Ω_d, dotted curves: desired value γ, dashed curves: simulated Ω_d response via model (6.6).

6.1.3 The whole dynamics and RTSO controller

We now propose a state space representation of the full arm experiment model, which comprises equation (6.5) together with (6.6). By defining the state z as $z := (\Omega_d, \dot{\theta}, \theta)$, we can rewrite the full arm dynamics by means of the following state space model:

$$\dot{z} = \begin{bmatrix} -a & 0 & 0 \\ b & 0 & 0 \\ 0 & 1 & 0 \end{bmatrix} z + \begin{bmatrix} a \\ 0 \\ 0 \end{bmatrix} \gamma =: \bar{A}z + \bar{B}\gamma\,. \tag{6.7a}$$

Due to safety reasons, we would like that the control input γ is not larger in magnitude than a fixed tunable value $\bar{\gamma}$, that is:

$$\gamma \in [-\bar{\gamma}, \bar{\gamma}]\,. \tag{6.7b}$$

Thanks to the structure of system (6.7), we select a realization of the RTSO controller (4.39) discussed in Chapter 4 for the case of equation (4.1a) with $n = 3$, $a > 0$, to which we will refer as "RTSO3T" controller. To this end, we rely on the auxiliary state x, arising from a similarity transformation, in

order to write system (6.7) as the standard RTSO parametrization for the case $n = 3$, $a > 0$ reported in equation (4.14):

$$x := Qz := \frac{1}{\bar{\gamma}} \begin{bmatrix} 1 & 0 & 0 \\ 1 & \frac{a}{b} & 0 \\ -1 & 0 & \frac{a^2}{b} \end{bmatrix} z\,, \tag{6.8a}$$

which transforms the dynamics to

$$\dot{x} = \begin{bmatrix} -a & 0 & 0 \\ 0 & 0 & 0 \\ 0 & a & 0 \end{bmatrix} x + \begin{bmatrix} a \\ a \\ -a \end{bmatrix} u, \quad u \in [-1,\, 1]\,. \tag{6.8b}$$

State x can now be used to evaluate the time-optimal switching function φ_3 in (4.15). The real input γ is then retrieved from the RTSO controller (4.39) in Chapter 4 by

$$\gamma = \bar{\gamma}((1 - |q|)kx + q), \tag{6.9}$$

where k is a stabilizing gain for the local linear controller working in the proximity of the origin. In particular, it will be selected as

$$k = [0\, k_d\, k_p]Q^{-1}\,, \tag{6.10}$$

where Q is defined in (6.8a).

6.1.4 Closed-loop experiments and comparison

Among all the closed-loop experiments that we carried out to test the RTSO controller, we decide to show here a limited set of them for the sake of clarity. We report experiments in which the goal is to reach the configuration $\theta = 0$, $\dot{\theta} = 0$ starting from an i-th initial condition for θ $\theta_{0i} \in \{-40,\, -20,\, 20,\, 40\}$ together with an initial velocity $\dot{\theta} = 0$. The experiments are carried out with a maximum control magnitude $\bar{\gamma} = 1$ and with a value of $\Omega_s = 10$. The local controller is tuned with $k_d = 8$ and $k_p = 15$, and the RTSO controller parameter ρ is set to $\rho = 0.8$. The RTSO tuning parameter ϵ is set to different values, as discussed below, for comparative purposes. For a better understanding of these parameters, the reader is referred to Chapter 4. For the sake of comparison, two other controllers are implemented and tested in the same scenarios described above:

- a RTSO realization with $n = 2$, $a = 0$ (labeled as "RTSO2") that neglects the actuator dynamics, that is, for a system in the form $\dot{z} = \left[\begin{smallmatrix} 0 & 0 \\ 1 & 0 \end{smallmatrix}\right] z + \left[\begin{smallmatrix} b \\ 0 \end{smallmatrix}\right] \gamma$ via an auxiliary state $x := \frac{1}{b\bar{\gamma}} I_2 z$, with I_2 the 2×2 identity matrix,
- a saturated proportional-derivative controller (labeled ad "PDsat") such as $\gamma = \mathrm{sat}_{\bar{\gamma}}(k_p\theta + k_d\dot{\theta})$.

Let us first analyze the closed-loop responses obtained with the RTSO3T controller. Figure 6.4 reports the results of these experiments. In particular, the time histories of different signals are plotted, that is, in the upper graph the time

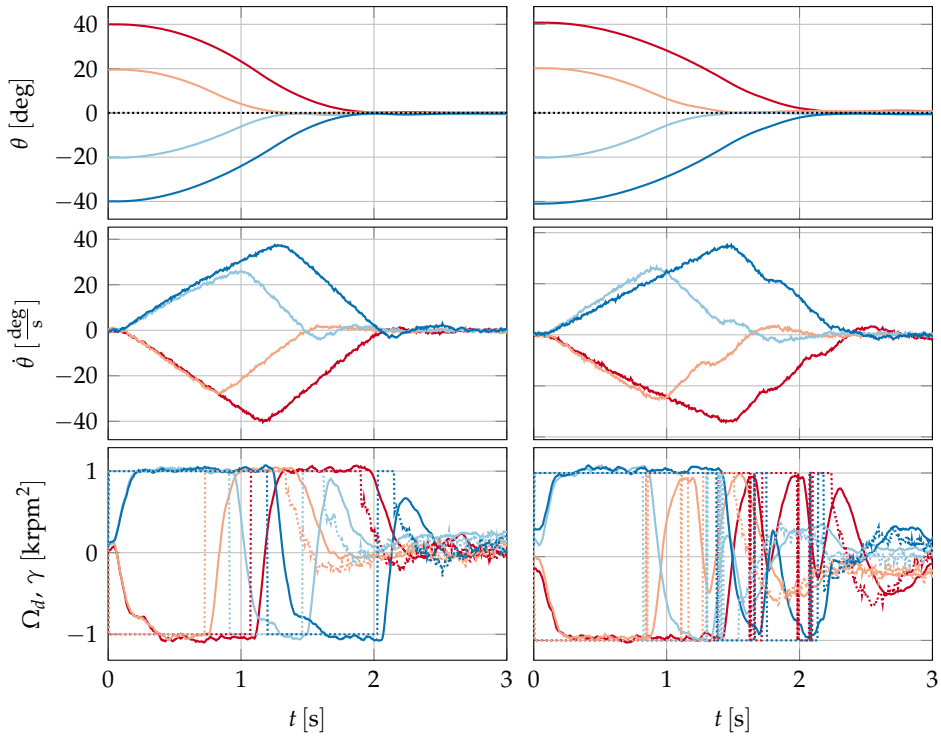

(a) Hysteresis parameter $\epsilon = 2$.

(b) Hysteresis parameter $\epsilon = 0$.

Figure 6.4: Closed-loop experimental response for the arm experiment with the RTSO$_3$T controller. Solid curves: real values, dotted curves: references.

history of θ, in the middle graph the one of $\dot{\theta}$, and in the bottom graph the one of Ω_d (solid curves) and the one of γ (dotted curves). In Figure 6.4a the RTSO hysteresis parameter ϵ is set equal to 2 as previously discussed, while in 6.4b ϵ was set to 0. From Figure 6.4a, we can immediately notice that the RTSO$_3$T controller produces a nice and desirable transient with a non overshooting behavior. Indeed, the θ reference is reached without going past it and without evident oscillations. An indicator of the good performances obtained with this controller are the obtained profiles of velocity $\dot{\theta}$, which essentially correspond to triangular profiles with just a small tail, which indicates a time-optimal like evolution. The control variable γ (and the actuator Ω_d correspondingly) suggests as well a time-optimal kind of transient, exhibiting a bang-bang behavior with at most 2 switches (recall that the order of the considered plant is 3) and a chattering free response. The absence of chattering is due to the selection of an hysteresis parameter $\epsilon > 0$. Indeed, Figure 6.4b shows that removing the hysteresis mechanism in the global stabilizer of the RTSO controller induces undesirable chattering of the control variable γ, which

degrades the controller performance, in addition to potentially damaging the actuators. Indeed, removing the hysteresis makes the RTSO controller fragile to unmodelled dynamics and noisy measurements. Finally, is worth to point out that the slight asymmetry between the evolutions starting from a positive and a negative θ initial condition is probably due to unmodeled dynamics such as a non perfect balance of the inertia in the experimental setup.

As for the comparison, we firstly analyze which performance we would have achieved if we had neglected the actuator dynamics, that is, with the RTSO2 controller. In this case the hysteresis parameter ϵ is set to zero, and the reason why the control γ does still not chatter will be clear when discussing the state trajectories in the phase plane. Figure 6.5 shows the experimental

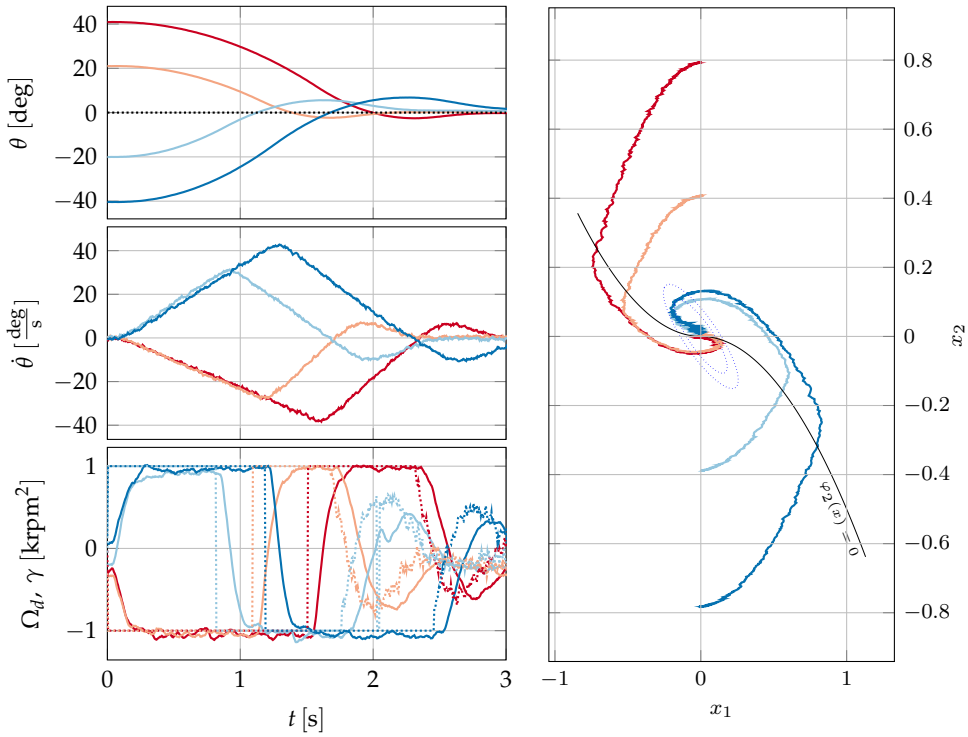

(a) Time history. **(b)** Phase plane.

Figure 6.5: Closed-loop experimental response for the arm experiment with the RTSO2 controller. Solid curves: real values, dotted curves: references.

responses obtained with this controller. It can be seen that disregarding the actuator dynamics leads to performance deterioration, turning into overshooting responses. The reason becomes clear observing the state space trajectories depicted in Figure 6.5b. Indeed, when a switch of the control variable γ occurs, that is when crossing the switching set $\{x|\varphi_2(x) = 0\}$, the trajectory does not

slide along the switching surface due to the finite actuator Ω_d band which does not push the trajectory promptly to follow the time-optimal trajectory. This fact is also responsible of the absence of chatter even if the parameter ϵ was set to zero.

Finally, we compare the RTSO$_3$T performances withe the simple PDsat controller. In Figure 6.6 we depicted a comparison of the θ evolution obtained

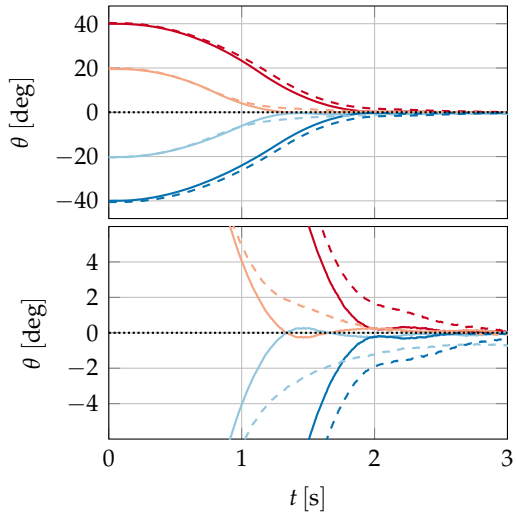

	$\theta_0 = 40°$	$\theta_0 = 20°$	$\theta_0 = -20°$	$\theta_0 = -40°$
RTSO$_3$T	1.830s	1.460s	1.565s	1.835s
PDsat	2.325s	1.965s	1.975s	2.535s

Figure 6.6: Closed-loop comparison: RTSO$_3$T (solid curves) vs. PDsat controller (dashed curves). The table shows the settling times.

with the two controllers, with a zoomed axis in the bottom plot. The PDsat gains k_p and k_d are tuned in such a way to prevent harsh oscillations in the presence of the saturation. We can notice that the RTSO$_3$T controller produces faster responses, as expected, since it globally behaves time-sub-optimally, while the PDsat has to be tuned with gentle gains to prevent oscillations due to the presence of the saturation. This is clear if we look at the settling time in the lower part of Figure 6.6. The settling time is defined as the smallest time such that the condition $|\theta| < 1°$ holds.

These experiments have shown the effectiveness of the RTSO controller designed and discussed in Chapter 4 when implemented in real applications, even in the case of a low-cost setup with limited performance. The RTSO controller is synthesized for a family of dynamical processes, but the case designed for a plant with a real negative pole and two poles in the origin is particularly meaningful for mechatronic applications. The RTSO controller is able to produce non-overshooting, clean and desirable evolutions, taking into account limitations of the actuators with saturations and reduced bandwidth

and preventing chattering of the control variable, thanks to the hysteresis mechanism both around the switching surface and when uniting the global and the local strategies.

6.2 THE HELICOPTER TRAVEL DYNAMICS

In this section, we address the second case study for the validation of the RTSO controller, represented by the travel dynamics of Quanser's 3 DOF Helicopter. This validation relies on the software benchmark tool developed in Chapter 5, which is instrumental to understanding this section.

The proposed RTSO implementation still relies on the virtual input ν and the control strategy developed in Section 5.6, which indeed will be used to compute the virtual input $(\nu_\varepsilon, \nu_\theta)$, while the virtual input ν_λ will be obtained by a realization of the RTSO controller. Then, the algorithm introduced in Section 5.6.2 will be used to derive the real control input starting from the virtual one. Computing ν_λ from the RTSO controller allows us to introduce an artificial saturation on this virtual input and to deal with it in a time-optimal fashion. The introduction of an artificial saturation on ν_λ allows us to limit the maximum magnitude of reference θ_r of the θ-*dof* generated by (5.20) (since typically ν_ε will be quasi-constant due to constant references ε_r) and therefore avoid the situation where a large λ_r reference will bring the experiment to a large and potentially unsafe θ_r. To this end, we constrain the input ν_λ to reside in the following compact set

$$\nu_\lambda \in [-\bar{\nu}_\lambda, \bar{\nu}_\lambda] \tag{6.11}$$

with $\bar{\nu}_\lambda$ representing the maximum admissible magnitude of ν_λ.

From (5.6e), the λ-*dof* dynamical model is

$$\ddot{\lambda} = -c_\lambda \dot{\lambda} - b_\lambda \cos(\varepsilon)\sin(\theta) f_s \,. \tag{6.12}$$

Substituting the term $\sin(\theta) f_s$, coming from the product $B(\theta)\tau$, with the virtual input ν_λ and applying the approximation $\cos(\varepsilon) \approx 1$ (which is reasonable since $\varepsilon \in [-15^\circ, 15^\circ]$, as mentioned in Section 5.6), the λ-*dof* dynamics can be rewritten as:

$$\ddot{\lambda} = -b_\lambda \nu_\lambda \,. \tag{6.13}$$

in which we also neglected the friction coefficient c_λ since its experimental value is very small. Equation (6.13) together with (6.11) represents a chain of two integrators with saturated input and input gain $-b_\lambda$. A straightforward selection would therefore be to use a RTSO controller for the case of equation (4.1a) in Chapter 4 with $n = 2$, $a = 0$. Nevertheless, as discussed in Section 5.6.2, we have to keep in mind that the virtual input ν_λ represents a desired value, while the applied virtual input $B(\theta)\tau$ has its own dynamical behavior depending on the θ-*dof* dynamics. We therefore could extend dynamics (6.13) in order to include a simple actuator model capturing the typical time constant of the real virtual input $\widetilde{\nu}_\lambda := \sin(\theta) f_s$ dynamics (coming from $B(\theta)\tau$) and use a RTSO controller for the case of equation (4.1a) in Chapter 4 with $n = 3$, $a > 0$. We proceed in illustrating both of these possibilities.

6.2.1 RTSO controller neglecting the input dynamics

If the ν_λ actuator dynamic is neglected, we can define the state $z := (\dot{\lambda}, \lambda)$ and write the λ dynamics in (6.13) by the following state space representation:

$$\dot{z} = \begin{bmatrix} 0 & 0 \\ 1 & 0 \end{bmatrix} z + \begin{bmatrix} -b_\lambda \\ 0 \end{bmatrix} \nu_\lambda \,. \tag{6.14}$$

In order to transform systems (6.14) to the standard RTSO parametrization illustrated in Section 4.2.1 for the case $n = 2$, $a = 0$, we rely on an auxiliary state x arising from a similarity transformation. In particular, consider

$$x := Qz := \frac{1}{-b_\lambda \bar{\nu}_\lambda} I_2 z \tag{6.15a}$$

with I_2 representing the 2×2 identity matrix, which transforms the dynamics to

$$\dot{x} = \begin{bmatrix} 0 & 0 \\ 1 & 0 \end{bmatrix} x + \begin{bmatrix} 1 \\ 0 \end{bmatrix} u, \quad u \in [-1, 1] \,. \tag{6.15b}$$

State x can be now used to evaluate the time-optimal switching function φ_2 in equation (4.9) of Chapter 4. The virtual input ν_λ is then retrieved from the RTSO controller (4.39) in Chapter 4 by

$$\nu_\lambda = \bar{\nu}_\lambda((1 - |q|)kx + q), \tag{6.16}$$

where k is a stabilizing gain for the local linear controller and q is the logic state of the RTSO controller. The stabilizing gain k is selected in such a way to have the same local behavior as the controller developed in Section 5.6, that is,

$$k = [2\zeta_\lambda \omega_\lambda \; \omega_\lambda^2] Q^{-1} \,. \tag{6.17}$$

6.2.2 RTSO controller considering the input dynamics

As mentioned above, a better choice for applying the RTSO controller to the helicopter's λ dynamics, would be to take into account a simple dynamical model representing the real virtual input $\widetilde{\nu}_\lambda$ dynamics. To this end, we now proceed to extending dynamics (6.13) by means of state $z := (\widetilde{\nu}_\lambda, \dot{\lambda}, \lambda)$, where the real virtual input $\widetilde{\nu}_\lambda$ has been promoted to a new state component. The proposed extended state-space model is

$$\dot{z} = \begin{bmatrix} -a & 0 & 0 \\ -b_\lambda & 0 & 0 \\ 0 & 1 & 0 \end{bmatrix} z + \begin{bmatrix} a \\ 0 \\ 0 \end{bmatrix} \nu_\lambda \tag{6.18}$$

where $1/a > 0$ represents the typical time constant of the $\widetilde{\nu}_\lambda = \sin(\theta) f_s$ dynamics. As in the previous case, we rely on an auxiliary state x in order to transform system (6.18) to the standard RTSO parametrization illustrated in Section 4.2.2 for the case $n = 3$, $a > 0$:

$$x := Qz := \frac{1}{\bar{\nu}_\lambda} \begin{bmatrix} 1 & 0 & 0 \\ 1 & \dfrac{a}{-b_\lambda} & 0 \\ -1 & 0 & \dfrac{a^2}{-b_\lambda} \end{bmatrix} z \,, \tag{6.19a}$$

which transforms the dynamics to

$$\dot{x} = \begin{bmatrix} -a & 0 & 0 \\ 0 & 0 & 0 \\ 0 & a & 0 \end{bmatrix} x + \begin{bmatrix} a \\ a \\ -a \end{bmatrix} u, \quad u \in [-1, 1]. \tag{6.19b}$$

State x can be now used to evaluate the time-optimal switching function φ_3 in equation (4.15) of Chapter 4. The virtual input reference value ν_λ is then retrieved form the RTSO controller (4.39) in Chapter 4 by

$$\nu_\lambda = \bar{\nu}_\lambda((1 - |q|)kx + q), \tag{6.20}$$

where k is a stabilizing gain for the local linear controller and q is again the logical state of the RTSO controller. The stabilizing gain k is selected in such a way that a similar local behavior to the controller developed in Section 5.6 is obtained, that is

$$k = (k_{\nu_\lambda}, 2\zeta_\lambda\omega_\lambda, \omega_\lambda^2)Q^{-1}. \tag{6.21}$$

6.2.3 Simulative comparison

In this section, we illustrate some comparative results between the two different realization of the RTSO controller discussed in Section 6.2.1 (to which we will refer with RTSO2) and 6.2.2 (to which we will refer with RTSO3T), and a saturated version of the λ component of (5.16) developed in 5.6 (to which we will refer with λ-(5.16)). The simulations will be carried out using the software benchmark tool developed in Chapter 5. The parameter b_λ was identified in Section 5.4.2, while $a = 1.26$ is selected in such a way to capture the θ-*dof* rising time. The same maximum value for the virtual input $\bar{\nu}_\lambda = 0.5$ is used for each one of the three controllers. The illustrated simulations start from an initial condition λ_0 taking value in $\lambda_{0i} := \{180°, 270°, 360°\}$, together with an initial velocity $\dot{\lambda}$ equal to zero. A constant reference position $\lambda_r = 0°$ has to be reached while tracking a constant elevation reference $\varepsilon_r = 10°$. The RTSO controller parameters are set to $\epsilon = 0.1$, $\rho = 0.5$. For a better understanding of these parameters, please refer to Chapter 4.

In the following figures we show the evolution of the λ-*dof* (solid curves) and the reference λ_r (black dotted curve) in the upper plot, the virtual input ν_λ (dotted curves) and the real virtual input $\widetilde{\nu}_\lambda$ (solid curves) in the lower plot. We start by analyzing the case of the RTSO2 controller. It is possible to notice from the response of the λ-*dof* depicted in Figure 6.7a, that neglecting the input dynamics turns into a significant performance degradation. To have a better insight of this behavior, let us look at the state space of system (6.14) depicted in Figure 6.7b. From here, it is possible to notice that, when a switch of the control occurs, the trajectories deviate from the switching set due to the unmodeled dynamics. This behavior is increasingly pronounced as the actuator and the plant have similar dynamic band. On the contrary, the RTSO3T controller, whose responses are depicted in Figure 6.8, produces a nice and non overshooting behavior with a time-optimal like type of convergence. This confirms that considering even a simple first order model for the actuator, and

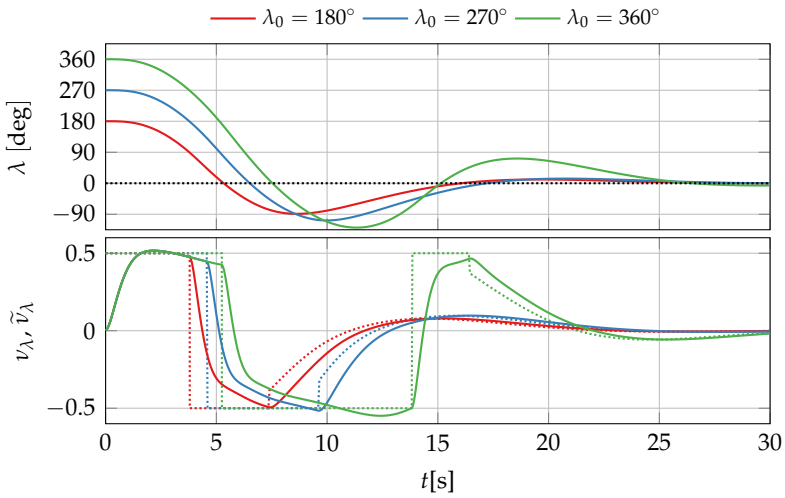

(a) Time history.

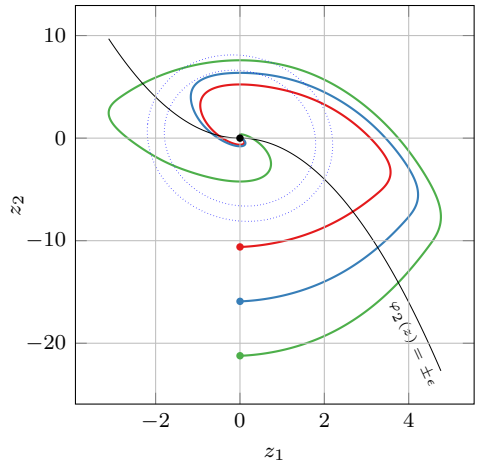

(b) Phase space.

Figure 6.7: Response of the λ-*dof* with the RTSO2 controller. Dotted curves: references, solid curves: actual signals.

taking it into account during the controller design, permits to represent well the plant dynamics and obtain desirable responses. Moreover, the hysteresis mechanism of the RTSO controller allows obtaining chattering free responses, even if the considered dynamics is a simplified version of the real one. In the third plot of Figure 6.8, we report the reference θ_r produced by the algorithm Section 5.6.2 and the evolution of the θ-*dof*, to illustrate how a bang-bang virtual input ν_λ essentially turns to a bang-bang reference θ_r.

Finally, in Figure 6.9, we compare the responses obtained with the RTSO3T (solid curves) and the λ-(5.16) controller (dashed curves). It is possible to notice

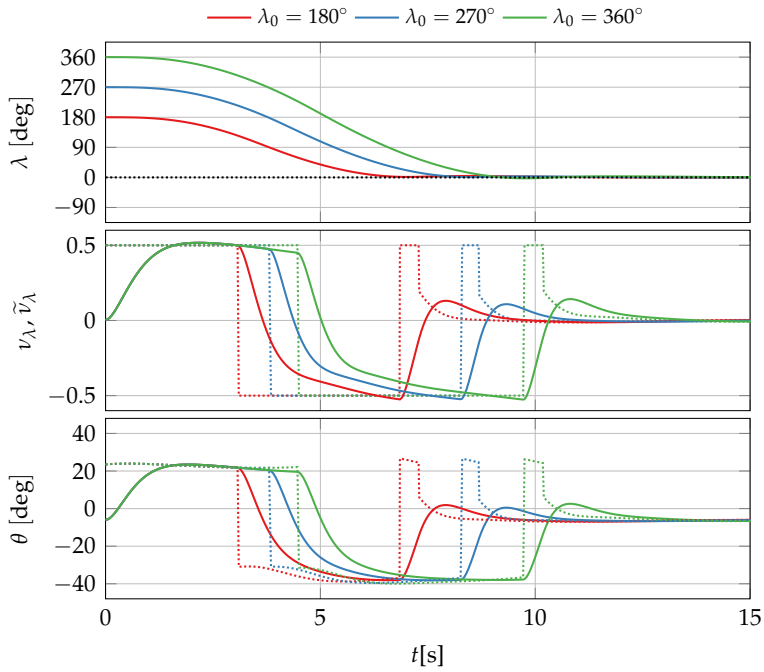

Figure 6.8: Response of the λ-*dof* with the RTSO3T controller. Dotted curves: references, solid curves: actual signals.

that the RTSO3T controller produces a faster transient and a more aggressive virtual input ν_λ. In the table at the bottom of Figure 6.9, we report the settling time for both controllers and for the three different initial conditions, intended as the minimum time such that the condition $|\lambda| < 1°$ holds. The RTSO3T controller is confirmed to produce faster convergence to the desired reference.

The RTSO controller therefore results to be well suited in situations where input saturation, whether it be real or artificial and introduced for safety reasons, is at stake, and convergence time plays an important role. The RTSO controller then allows us to take into account different technological aspects, such as actuators with limited bandwidth.

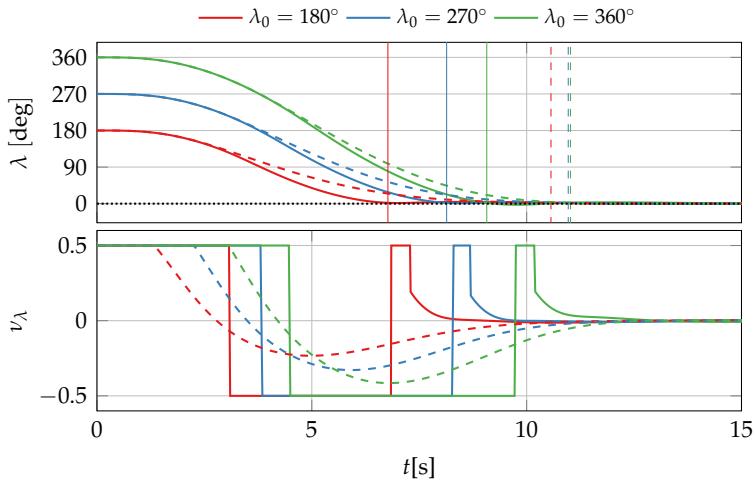

	180°	270°	360°
RTSO3T	6.7s	8.1s	9.0s
λ-(5.16)	10.6s	11.0s	11.1s

Figure 6.9: Comparison between the RTSO3T and the λ-(5.16) controller. Dotted curves: references, solid curves: actual signals.

Part III

SPEED ESTIMATOR

7 A CLASS OF HYBRID VELOCITY OBSERVERS FOR ANGULAR MEASUREMENTS WITH JUMPS

In this chapter we propose a hybrid nonlinear high-gain observer to estimate the speed of rotary systems equipped with potentiometer-based, capacitive or Hall-effect rotary sensors or providing angular measurements evolving in $\mathbb{S}_1$*, exhibiting unpredictable jumps of* 2π*. These sensors comprise rotary displacement potentiometer sensors, rotary displacement capacitive sensors, and Hall-effect based encoders. A hybrid measurement model is proposed, based on which a hybrid high-gain observer is synthesized, which does not require the knowledge of the jump times. Asymptotic tracking of the proposed observer is proven. A sampled-data approximation of the proposed observer is developed as well, based on which an experimental validation shows suitability for real-time applications. The proposed observer has been exploited in the experimental setup of Chapter 6. This chapter is based on the published work [23].*

7.1 INTRODUCTION

Observers are fundamental building blocks in control when facing output feedback problems. Many strategies have been proposed in order to estimate the plant state starting from its output, such as Luenberger observers [7], passivity-based observers [2], and high-gain observers [55]. Among these, high-gain observers are a well established tool when the process to be observed contains some unmodelled dynamics. They are also used in order to estimate the time derivative of the plant's output, making use of the high-gain scaling parameter as a tuning parameter allowing one to trade off between responsiveness and noise sensitivity of the observer [76], [28]. Recently, the hybrid dynamical system framework of [45] has been exploited in order to enhance the performance or extend the use of classical continuous-time observers, both in the high-gain scheme [8], [32], and in cases where hybrid dynamical systems are at stake (see [17] and references therein).

Systems that evolve on the unit circle are well studied under different filtering and synchronization points of view. See the filtering problem analyzed in [31], [105], and [48], the consensus problem studied in [91], the optimization problem faced in [98], or the filtering problem on the more general special orthogonal group $\mathrm{SO}(3)$ considered in [68].

In this chapter, we address state estimation for a rotational displacement process whose position evolves on $\mathbb{S}_1$ starting from angular measurements that evolve in the compact set $[0°, 360°]$, whose model is developed in Section 7.2. In technological applications, many rotary displacement sensors exist exhibiting this feature, such as potentiometric, capacitive, or Hall-effect based rotational sensors. For example, [70] proposes the use of a low cost Hall-effect rotary displacement sensor for controlling a synchronous reluctance machine, while [6] develops a new capacitive sensor capable of measuring both translational and rotational displacements, the latter one evolving on $\mathbb{S}_1$. In [1], [36], and [97], Hall-effect sensors are exploited for either estimating or controlling the rotor position of permanent-magnet motors, while in [100], a capacitive angular speed sensor is proposed, along with a technological approach for estimating the rotational velocity from measurements affected by unpredictable 2π jumps.

Our solution adopts the hybrid formalism of [45] in order to synthesize a class of hybrid high-gain observers with nonlinear injection, that estimates the speed (and a filtered version of the angular position) of a rotational displacement system evolving on the unit circle. An important feature of the proposed approach is that it is independent of the jump times. Both a hybrid continuous-discrete solution (developed in Section 7.3) and a sampled-data solution (presented in Section 7.5) are presented, each of them with stability guarantees. Simulation and experimental results using a Hall-effect-based sensor validate the proposed designs.

7.2 HYBRID MEASUREMENTS MODEL

Consider a rotational system, with angular position x_1 and angular velocity x_2, following the hybrid dynamics

$$\begin{cases} \dot{x} = Ax + d, & |y| \in [0,\, \hat{\pi}] \\ x^+ = h_1(x), & y \in \mathcal{J}_1 \\ y = Cx + w = x_1 + w\,, \end{cases} \tag{7.1a}$$

where $x = (x_1,\, x_2) \in \mathcal{X} := \left[-\frac{3}{2}\pi,\, \frac{3}{2}\pi\right] \times \mathbb{R}$ is the plant state and $y = x_1 + w$ is the plant output. Moreover,

$$A := \begin{bmatrix} 0 & 1 \\ 0 & 0 \end{bmatrix}, \quad C := \begin{bmatrix} 1 & 0 \end{bmatrix} \tag{7.1b}$$

$$h_1(x) := \begin{bmatrix} x_1 - 2\pi \mathrm{sign}\,(x_1) \\ x_2 \end{bmatrix}, \tag{7.1c}$$

$$\mathcal{J}_1 := [-\tfrac{3}{2}\pi,\, -\hat{\pi}] \cup [\hat{\pi},\, \tfrac{3}{2}\pi]\,, \tag{7.1d}$$

$w \in [-\rho, \rho]$ represents bounded measurement noise, $\hat{\pi} := \pi + \delta_\pi$ with $\delta_\pi > 0$, and $d \in \mathbb{R}^2$ is an unknown process disturbance, which may arise from unmodelled dynamics. In particular, the data of the hybrid measurement model encodes the integrating structure of the rotational system and the 2π jump mechanism affecting the measurement. The (typically small) positive scalar δ_π prevents persistent ineffective jumps of 2π (Zeno solutions) and the

specific selection of $\delta_\pi > 0$ does not affect the velocity estimation because it simply produces 2π shifts of the angular estimate. Similarly, selecting $\mathcal{X} = \left[-\frac{3}{2}\pi, \frac{3}{2}\pi\right]$ enables measurement jumps in a larger set than just $[-\pi, \pi]$ so that measurement noise cannot push the state outside flow and jump sets thereby prematurely terminating solutions.

We assume that in the nominal case, i.e., $w = 0$ and $d = 0$, the hybrid measurement model in (7.1) is such that its state x evolves in a compact set $\mathcal{K} \subset \mathcal{X}$, that is at constant velocity x_2 ranging in a compact set $\mathcal{K}_2$ as follows:

$$x \in \mathcal{K} := [-\tfrac{3}{2}\pi, \tfrac{3}{2}\pi] \times \mathcal{K}_2 \subset \mathcal{X}. \tag{7.2}$$

In the next section we propose an observer estimating x_2 without knowledge of the measurement jump times.

7.3 A FAMILY OF HIGH GAIN HYBRID OBSERVERS

7.3.1 Observer Dynamics

Consider the following hybrid high-gain observer with state $\hat{x} := (\hat{x}_1, \hat{x}_2) \in \mathcal{X}$, input φ and output $\hat{y}$:

$$\mathcal{H}_\varphi := \begin{cases} \dot{\hat{x}} = A\hat{x} + L\varphi(e_y), & (\hat{y}, y) \in \widehat{\mathcal{C}} \\ \hat{x}^+ = h_1(\hat{x}), & \hat{y} \in \mathcal{J}_1 \\ \hat{x}^+ = h_2(\hat{x}, y) & y - \hat{y} \in \mathcal{J}_2 \\ \hat{y} = C\hat{x} = \hat{x}_1 \end{cases} \tag{7.3a}$$

$$\begin{aligned} &h_2(\hat{x}, y) := (y, \hat{x}_2) \\ &\mathcal{J}_2 := [-\pi - \delta_\pi, -\pi + \delta_\pi] \cup [\pi - \delta_\pi, \pi + \delta_\pi] \\ &\widehat{\mathcal{C}} := \{(\hat{y}, y) \mid \hat{y} \in \overline{[-\tfrac{3}{2}\pi, \tfrac{3}{2}\pi] \setminus \mathcal{J}_1}, \\ &\qquad y - \hat{y} \in \overline{[-3\pi, 3\pi] \setminus \mathcal{J}_2}\} \end{aligned} \tag{7.3b}$$

where matrix A, the jump dynamics h_1, and the jump set $\mathcal{J}_1$ are defined in (7.1), $\varphi : \mathbb{R} \mapsto \mathbb{R}$ is a nonlinear output injection function depending on the output estimate error $e_y := y - \hat{y}$, L is a matrix of positive gains, and h_2 together with $\mathcal{J}_2$ provides faster transients when the output error is very large.

Assumption 7.1. *The nonlinear output injection function $e_y \mapsto \varphi(e_y)$ is such that:*

1. *φ is continuous in $\mathbb{B}_{\pi - \delta_\pi}(0)$,*
2. *$e_y \varphi(e_y) > 0$ for all $e_y \in (-\pi, \pi) \setminus \{0\}$,*
3. *$\varphi(e_y) = \varphi(e_y + 2k\pi)$ for all $k \in \{-1, 0, 1\}$ and all $e_y \in \mathbb{B}_{\pi - \delta_\pi}(0)$,*
4. *$\frac{d\varphi(e_y)}{de_y}\Big|_{e_y = 0} = 1$.*

In Assumption 7.1, item 1 ensures continuity of the right hand side during flow; item 2 represents a sector condition needed for a stabilizing output

injection, and ensures $\varphi(e_y) = 0$ if and only if $e_y = 0$; item 3 represents a periodicity condition so that the same output injection term is applied across jumps of $\pm 2\pi$ of e_y. Without loss of generality, item 4 implies that locally the high gain observer (7.3) behaves as a classical linear high-gain observer with gain L for every selection of φ. This assumption is nonrestrictive but it is useful for the tuning of gain L, and it simplifies the analysis and the generalization of Section 7.5.

Remark 7.1. *Items 1, 2, and 3 of Assumption 7.1 imply that $\varphi(e_1) = 0$ if and only if $e_1 \in \{2k\pi,\, k \in \{-1, 0, 1\}\}$.* ⌟

Matrix L in (7.3a) is designed based on a pair of positive scalar gains k_1 and k_2 and a positive high-gain scaling factor ϵ as follows: $L := (\ell_1,\, \ell_2) := \left(k_1/\epsilon,\, k_2/\epsilon^2\right)$. The selection of k_1 and k_2 has to be such that the characteristic equation $s^2 + k_v s + k_p = 0$ has roots with negative real part, and the high-gain scaling factor ϵ represents a design parameter that can be conveniently adjusted in order to obtain a trade-off between smoothing action (larger ϵ) and reduction of the time lag of the estimator (smaller ϵ) [76]. The high-gain structure also allows rejecting process noise when ϵ is small enough.

In this work, we are interested in studying the stability properties of the interconnection between the measurement model (7.1) and the observer (7.3) with respect to the compact attractor $\mathcal{A} \subset \mathcal{K} \times \mathcal{X}$ defined as:

$$\mathcal{A} := \left\{(x, \hat{x}) \,|\, x \in \mathcal{K},\, \hat{x} = x + \left[\begin{smallmatrix} 2k\pi \\ 0 \end{smallmatrix}\right],\, k \in \{-1, 0, 1\}\right\} \tag{7.4}$$

based on Assumption 7.1. The particular selection of $\mathcal{A}$ encodes the fact that we are interested in having an estimate of the position modulo 2π rotations. The following is our main result, whose proof is reported in Section 7.3.4.

Theorem 7.1. *Under Assumption 7.1, attractor $\mathcal{A}$ in (7.4) is uniformly globally asymptotically stable (UGAS) for the interconnection dynamics between system (7.1) and (7.3).*

7.3.2 The interconnected system

To the end of proving Theorem 7.1, we start the analysis of the interconnection between the measurement model (7.1) and the observer (7.3) by defining the estimation error e as the mismatch between the measurement model state x and the estimated state $\hat{x}$:

$$e := (e_1,\, e_2) := x - \hat{x} \in \mathcal{E} := [-3\pi,\, 3\pi] \times \mathbb{R}\,. \tag{7.5}$$

Since an autonomous representation of the tracking error dynamics e cannot be written, we study the stability of $\mathcal{A}$ in (7.4) by writing the interconnection between plant (7.1) with zero inputs and observer (7.3) in their original coordinates $(x, \hat{x}) \in \mathcal{K} \times \mathcal{X}$, corresponding to:

$$\begin{cases} (\dot{x}, \dot{\hat{x}}) = \left[\begin{smallmatrix} A & 0 \\ 0 & A \end{smallmatrix}\right](x, \hat{x}) + \left[\begin{smallmatrix} 0 \\ L \end{smallmatrix}\right]\varphi(e_1) & (x, \hat{x}) \in \mathcal{C} \\ (x^+, \hat{x}^+) \in G(x, \hat{x}) & (x, \hat{x}) \in \mathcal{D} \end{cases} \tag{7.6a}$$

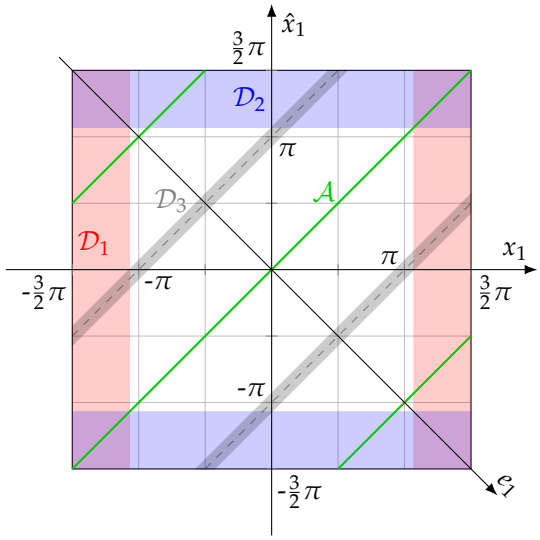

Figure 7.1: Projection of the jump sets and the attractor on the $(x_1, \hat{x}_1)$ plane.

where

$$\mathcal{D} := \bigcup_{j\in\{1,2,3\}} \mathcal{D}_j, \quad \mathcal{C} := \overline{\mathcal{K}\times\mathcal{X}\setminus\mathcal{D}} \tag{7.6b}$$

$$\begin{aligned} &\mathcal{D}_1 := \mathcal{J}_1 \times \mathcal{K}_2 \times \mathcal{X}, \quad \mathcal{D}_2 := \mathcal{K} \times \mathcal{J}_1 \times \mathbb{R} \\ &\mathcal{D}_3 := \{(x,\hat{x}) | x_1 - \hat{x}_1 \in \mathcal{J}_2\} \end{aligned} \tag{7.6c}$$

$$G(x,\hat{x}) := \bigcup_{j\in\{1,2,3\}|(x,\hat{x})\in\mathcal{D}_j} g_j(x,\hat{x}) \tag{7.6d}$$

$$\begin{aligned} &g_1(x,\hat{x}) := (h_1(x),\hat{x}), \quad g_2(x,\hat{x}) := (x, h_1(\hat{x})) \\ &g_3(x,\hat{x}) := (x, h_2(\hat{x}, x_1)). \end{aligned} \tag{7.6e}$$

In (7.6), by construction, G is a set-valued mapping (multiple jumping conditions may be active at the same time) that possesses the useful property of having a closed graph because its graph is the union of the (closed) graphs of g_i. Since the elements of the jump set $\mathcal{D}$ impose jump conditions only based on x_1 and $\hat{x}_1$, in Figure 7.1 we have projected these elements on the $(x_1, \hat{x}_1)$ plane, in order to provide a graphical representation and intuition of the shape of these sets, together with the attractor $\mathcal{A}$.

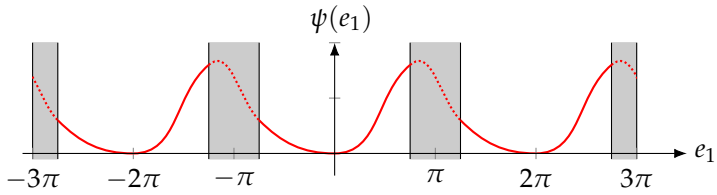

Figure 7.2: Prototype of the potential function $\psi(e_1)$.

7.3.3 Lyapunov function and its properties

Consider the following differentiable function:

$$\psi(e_1) := \begin{cases} \int_{-2\pi}^{e_1} \varphi(v)dv, & \text{if } e_1 \in \mathbb{B}_{\pi-\delta_\pi}(-2\pi) \\ \int_{0}^{e_1} \varphi(v)dv, & \text{if } e_1 \in \mathbb{B}_{\pi-\delta_\pi}(0) \\ \int_{2\pi}^{e_1} \varphi(v)dv, & \text{if } e_1 \in \mathbb{B}_{\pi-\delta_\pi}(2\pi) \\ \psi_p(e_1), & \text{otherwise}, \end{cases} \tag{7.7}$$

where $\psi_p : [-3\pi, 3\pi] \setminus \{\mathbb{B}_{\pi-\delta_\pi}(-2\pi) \cup \mathbb{B}_{\pi-\delta_\pi}(0) \cup \mathbb{B}_{\pi-\delta_\pi}(2\pi)\} \mapsto \mathbb{R}_{>0}$ represents a positive smooth continuation [11, Lem. 1.4.2] of the three selections of ψ in the complement of the three disjoint sets at the right of (7.7). A prototype of ψ is depicted in Figure 7.2. Note that from items 2 and 3 of Assumption 7.1, ψ is positive definite with respect to the set $\{-2\pi, 0, 2\pi\}$.

To study the stability properties of the compact attractor $\mathcal{A}$ in (7.4) for the interconnected system (7.6), we construct a Lyapunov function $V : \mathcal{K} \times \mathcal{X} \mapsto \mathbb{R}$ composed by a "potential" term represented by the function ψ in equation (7.7) depending on the position error e_1, and a "kinetic" term proportional to the square of the speed error e_2 as per (7.5):

$$V(x, \hat{x}) := \psi(x_1 - \hat{x}_1) + \frac{(x_2 - \hat{x}_2)^2}{2\ell_2} = \psi(e_1) + \frac{e_2^2}{2\ell_2}, \tag{7.8}$$

Lemma 7.1. *Under Assumption 7.1, given V in (7.8) and considering the interconnected system (7.6), it holds that:*

$$\begin{aligned} &\dot{V}(x, \hat{x}) = -\ell_1 \varphi^2(e_1) \leq 0 \quad && \forall\, (x, \hat{x}) \in \mathcal{C}\,, \\ &\Delta V(x, \hat{x}) \leq 0 && \forall\, (x, \hat{x}) \in \mathcal{D}\,. \end{aligned} \tag{7.9}$$

Proof. *The gradient of V with respect to $(x, \hat{x})$ is*

$$\nabla V(x, \hat{x}) = \left(\varphi(x_1 - \hat{x}_1),\, \tfrac{x_2 - \hat{x}_2}{\ell_2},\, -\varphi(x_1 - \hat{x}_1),\, -\tfrac{x_2 - \hat{x}_2}{\ell_2}\right)$$

and then, after scalar product with the flow dynamics (7.6),

$$\begin{aligned} \dot{V}(x, \hat{x}) &= \langle \nabla V(x, \hat{x}), (\dot{x}, \dot{\hat{x}}) \rangle = -\ell_1 \varphi^2(x_1 - \hat{x}_1) \\ &= -\ell_1 \varphi^2(e_1) \leq 0\,, \end{aligned} \tag{7.10}$$

which is zero if $e \in \left\{ \left[\frac{2k\pi}{s} \right] \mid k \in \{-1, 0, 1\}, s \in \mathbb{R} \right\}$ *and negative otherwise (thanks to the observation in Remark 7.1).*

With regard to $\Delta V(x, \hat{x})$*, the jump map* G *in (7.6d) is such that either* e_1 *experiences jumps of* $\pm 2\pi$ *due to its elements* g_1 *and* g_2 *in (7.6e), leading to* $V(x^+, \hat{x}^+) = V(x, \hat{x})$ *(thanks to the* 2π *periodicity of the potential term* $\psi(e_1)$ *in (7.7)), or* $|e_1| > |e_1^+| = 0$ *due to its element* g_3 *in (7.6e), resulting in zeroing out the potential term of* V*, thus giving* $V(x^+, \hat{x}^+) < V(x, \hat{x})$ *because* $(x, \hat{x}) \in \mathcal{D}_3 \Rightarrow \psi(e_1) > 0$. □

7.3.4 Proof of Theorem 7.1

To the end of proving Theorem 7.1, we will rely on the smooth candidate Lyapunov function in (7.8) toghether with Corollary 1.1 in Chapter 1. It holds that $V(x, \hat{x}) = 0, \ \forall \ (x, \hat{x}) \in \mathcal{A}$. Indeed, both the potential and the kinetic term zero out when $(x, \hat{x}) \in \mathcal{A}$, that is when $e_1 = 2k\pi$, $k \in \{-1, 0, 1\}$ and $e_2 = 0$. Moreover, from item 2 of Assumption 7.1 it is immediate to see that $V(x, \hat{x}) > 0, \ \forall \ (x, \hat{x}) \in (\mathcal{K} \times \mathcal{X}) \setminus \mathcal{A}$. Furthermore, V is radially unbounded. Indeed, the kinetic term tends to infinity as the distance from the attractor tends to infinity (recall that $x_2 \in \mathcal{K}_2$, which is bounded), whereas the potential term has an argument evolving on a compact set, because both x_1 and $\hat{x}_1$ evolve in a compact set. From Lemma 7.1, $\dot{V}(x, \hat{x}) = -\ell_1 \varphi^2(e_1) \leq 0$ and $\Delta V(x, \hat{x}) \leq 0$ for (7.6) under Assumption 7.1. Since we do not have strict decrease of the Lyapunov function in equation (7.8), we conclude the proof by recalling the invariance argument of Corollary 1.1. Consider any solution ζ to (7.6) such that $V(\zeta(0,0)) \neq 0$. If $\zeta(0,0) \in \mathcal{C}$, either $\varphi(e_1(0,0)) \neq 0$, and then $\dot{V}(\zeta(0,0)) < 0$ thanks to Lemma 7.1, or $\varphi(e_1(0,0)) = 0$. In the latter case, the flow dynamics of interconnection (7.6) leads to $\dot{e}_1 = e_2$, which implies that there exists an arbitrary small time τ such that $\varphi(e_1(\tau, 0)) \neq 0$, leading to decreasing of the Lyapunov function. Consider now the case of $\zeta(0,0) \in \mathcal{D}$. Jumps due to g_3 in (7.6e) lead to decreasing of V, as discussed in the proof of Lemma 7.1. If $\zeta(0,0) \in \mathcal{D}_1 \setminus \mathcal{D}_2$, either $\zeta(0,1) \in \mathcal{C}$ or $\zeta(0,1) \in \mathcal{D}_3$, leading in both cases to a decrease of V. A similar reasoning holds if $\zeta(0,0) \in \mathcal{D}_2 \setminus \mathcal{D}_1$. If $\zeta(0,0) \in \mathcal{D}_1 \cap \mathcal{D}_2$, a jump forces the solution to evolve in one of the above analyzed cases. Therefore, there is no complete solution ζ of (7.6) such that $V(\zeta(t,j)) = V(\zeta(0,0)) \neq 0, \ \forall (t,j) \in \mathrm{dom}(\zeta)$, that is V cannot be constant (and nonzero), completing the proof. ■

7.4 SIMULATIONS

In this section we illustrate the performance of the proposed hybrid observer with four different selections of the output injection nonlinearity φ, all satisfying Assumption 7.1. In particular, the following case studies are analyzed:

1. $\varphi(e_y) = \sin(e_y)$ [blue curves]
2. $\varphi(e_y) = 2\tan(\frac{e_y}{2})$ [red curves]
3. $\varphi(e_y) = \mathrm{saw}(e_y)$ [green curves]
4. $\varphi(e_y) = \mathrm{sat}_M(\mathrm{saw}(e_y))$ [purple curves]

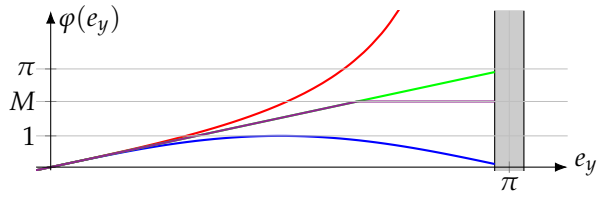

Figure 7.3: The four selections of φ proposed in Section 7.4.

where with saw : $\mathbb{R} \mapsto \mathbb{R}$ we refer to the following piecewise linear function (a sawtooth selection) $\text{saw}(s) := \mod(s + \pi, 2\pi) - \pi$, and with $\text{sat}_M : \mathbb{R} \mapsto \mathbb{R}$ to the classical saturation function $\text{sat}_M(s) := \max(-M, \min(s, M))$. The shape of the function is reported in Figure 7.3, which reveals similar small signal behaviors but different behaviors with larger errors. It easy to check that all the four case studies respect the four items of Assumption 7.1. In the following simulations, the same gains $k_p = 5$, $k_v = 6$, the same high-gain scaling factor ϵ, and the same initial state $\hat{x}_0 = (0, 0)$ are used on all of the case studies. Scalar δ_π is set to 5°.

The first simulation, depicted in Figure 7.4, is a noise free simulation ($w = 0$), where the measurement model's initial condition is $x = (0, 10)$. The initial angular velocity of $x_2 = 10 \frac{\text{rad}}{\text{sec.}}$ is sustained for the first 2 sec.. Then the process disturbance d quickly pushes it to $x_2 = -20 \frac{\text{rad}}{\text{sec.}}$. In this simulation $\epsilon = 0.7$ and parameter M of function sat_M is 1. It is possible to notice from the first 2 sec. of simulation that when the output tracking error e_y is small with respect to the current selection of ϵ, all the considered output-injection functions φ produce similar responses. This is expected, since they share the same local behavior thanks to item 4 of Assumption 7.1 (see also Figure 7.3). In the second part of the simulation, the sudden variation of the angular speed x_2 produces a larger tracking error, resulting in different responses for the different selections. In particular, the best performances are the ones produced by the "tan" and "saw" output injection functions, with a slight advantage for the "tan" selection. This can be explained by the fact that the "tan" selection represents a barrier-like function with respect to the jump set $\mathcal{D}_3$, that is, this selection prevents the output error e_y to become larger than $\pi - \delta_\pi$ in magnitude. It is not surprising that the worst response is the one produced by the "sin" and "sat" output injection functions, due to their limited action for large output errors e_y. Moreover, looking at the bottom plot of Figure 7.4, it is possible to observe the decrease of the Lyapunov function after jumps from $\mathcal{D}_3$, i.e., when e_1 approaches $\pm\pi$.

The second simulation, depicted in Figure 7.5, takes into account a noise signal $w \in [-15°, 15°]$, a scaling factor $\epsilon = 0.1$ and the saturation level of function sat_M selected as $M = 0.03$. Conclusions similar to those of the first simulation can be drawn.

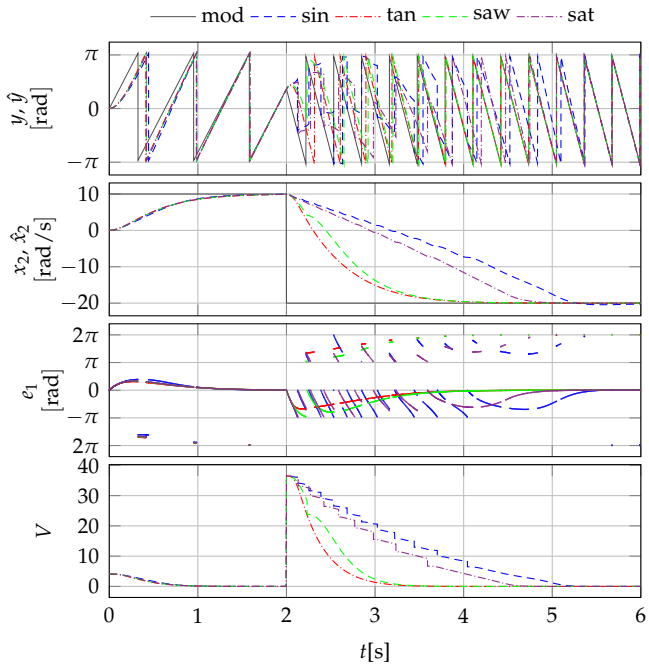

Figure 7.4: Continuous-time simulation without measurement noise using the four injection functions of Section 7.4 and $\epsilon = 0.7$.

7.5 SAMPLED-DATA APPROXIMATION AND EXPERIMENTAL RESULTS

For real-time implementation, in this section we propose a discretized version of the observer introduced in equation (7.3) with periodic sampling time $T > 0$.

7.5.1 An equivalent sampled-data system

Introduce a timer τ triggering the T-periodic sampling, and sampled versions $\bar{x}$ and $\bar{\hat{x}}$ of the measurement state x and the observer state $\hat{x}$, resulting in the following extended version of dynamics (7.6), where we denote $\xi := (x, \hat{x}, \bar{x}, \bar{\hat{x}}, \tau)$, and where trivial jumps (namely jumps leaving the corresponding states unchanged) are omitted for conciseness:

$$\begin{aligned} (\dot{x}, \dot{\hat{x}}) &= \left[\begin{smallmatrix} A & 0 \\ 0 & A \end{smallmatrix}\right](x, \hat{x}) + \left[\begin{smallmatrix} 0 \\ L \end{smallmatrix}\right]\varphi(e_1) && \xi \in \mathcal{C}^\xi \\ (\dot{\bar{x}}, \dot{\bar{\hat{x}}}, \dot{\tau}) &= (0, 0, 1) \\ \xi^+ &\in G^\xi(\xi) && \xi \in \mathcal{D}^\xi. \end{aligned} \tag{7.11a}$$

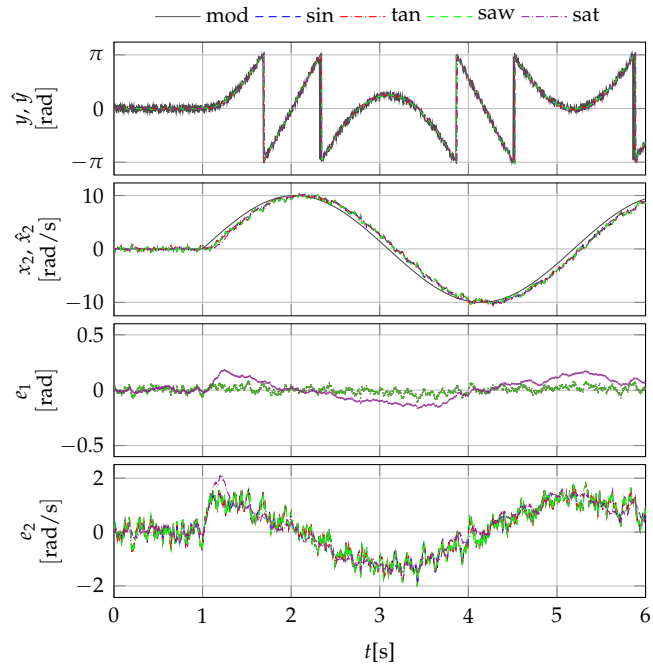

Figure 7.5: Continuous-time simulation with measurement noise using the four injection functions of Section 7.4 and $\epsilon = 0.1$.

Above, the jump set is the union $\mathcal{D}^\xi := \mathcal{D}_1^\xi \cup \mathcal{D}_T^\xi$, and the jump map G^ξ is selected, similarly to (7.6d), as the outer semicontinuous hull $G^\xi(\xi) := \bigcup_{j\in\{1,T\}|\xi\in\mathcal{D}_j^\xi} g_j^\xi(\xi)$ of the measurement jump rule [1] inherited from (7.6c),

$$x^+ = h_1(x), \qquad \xi \in \mathcal{D}_1^\xi := \{\xi : \ x \in \mathcal{D}_1\}, \tag{7.11b}$$

and the sampling-related jump, resetting the timer to zero, implementing the jumps of $\hat{x}$ from (7.6c), and updating the sampled states $(\bar{x}, \bar{\hat{x}})$,

$$\begin{aligned} &\bar{\hat{x}}^+ = \hat{x}^+ \in \bar{h}_1(\bar{h}_2(\hat{x}, y)), \\ &(\bar{x}, \tau)^+ = (x, 0), \end{aligned} \quad \xi \in \mathcal{D}_T^\xi := \{\xi : \ \tau = T\}. \tag{7.11c}$$

where $\bar{h}_1$ and $\bar{h}_2$ are the following outer semicontinuous extensions of function h_1 and h_2 in (7.1c) and (7.3b):

$$\bar{h}_1(x) := \begin{cases} h_1(x), & \text{if } x_1 \in \mathcal{J}_1 \setminus \partial\mathcal{J}_1 \\ x, & \text{if } x_1 \notin \mathcal{J}_1 \\ \{x\} \cup \{h_1(x)\}, & \text{if } x_1 \in \partial\mathcal{J}_1. \end{cases} \tag{7.11d}$$

1 For compact notation, we don't define explicitly maps $g_j^\xi(\xi)$, $j = 1, T$, we only report in (7.11b)-(7.11c) the quantities that perform nontrivial jumps.

$$\bar{h}_2(\hat{x}, y) := \begin{cases} h_2(\hat{x}, y), & \text{if } y - \hat{x}_1 \in \mathcal{J}_2 \setminus \partial\mathcal{J}_2 \\ \hat{x}, & \text{if } y - \hat{x}_1 \notin \mathcal{J}_2 \\ \{\hat{x}\} \cup \{h_2(\hat{x}, y)\}, & \text{if } y - \hat{x}_1 \in \partial\mathcal{J}_2. \end{cases} \tag{7.11e}$$

The model is completed by the selection of the flow set:

$$\mathcal{C}^\xi := \{\xi : (x, \hat{x}) \in \overline{(\mathcal{K} \times \mathcal{X}) \setminus \mathcal{D}_1}, \tau \in [0, T]\}, \tag{7.11f}$$

which enforces flowing in the interior of the sampling interval $\tau \in (0, T)$ unless the measurement model jumps (from $\mathcal{D}_1^\xi$). The following proposition is a key step towards our sampled-data implementation of the next section.

Proposition 7.1. *There exists a small enough T^* such that for any $T \in (0, T^*]$, the following compact set*

$$\mathcal{A}^\xi := \{\xi : \tau \in [0, T], x - \hat{x} \in \mathcal{P}, \bar{x} - \bar{\hat{x}} \in \mathcal{P}, \\ x - (I + A\tau)\bar{x} \in \mathcal{P}\}, \tag{7.12}$$

(where $\mathcal{P} := \{\left[\begin{smallmatrix} 2k\pi \\ 0 \end{smallmatrix}\right] \mid k \in \{-1, 0, 1\}\}$ represents the 2π shifted origin) is UGAS for system (7.11).

Proof. *First note that after at most T ordinary time instants, any solution jumps from $\mathcal{D}_T^\xi$ and then evolves forever in the forward invariant manifold $\mathcal{M} := \{\xi : x - (I + A\tau)\bar{x} \in \mathcal{P}\}$. From this manifold, since the flow dynamics of (7.11) coincide with those of (7.6) the Lyapunov flow condition established in the proof of Theorem 7.1 still holds. Similar to the proof of Theorem 7.1, jumps from both $\mathcal{D}_1^\xi$ and $\mathcal{D}_T^\xi$ cause no increase of the Lyapunov function and the result is implied by persistent flowing and the invariance principle.* □

7.5.2 Approximated sampled-data system

Let us consider a solution of the sampled-data model (7.11) and denote by $(t_j, j-1)$ any jump time such that $\tau(t_j, j-1) = T$ and $\tau(t_j, j) = 0$. Exploiting the specific structure of matrix A, we have for all t before the next jump,

$$x(t, j) = (I + A\tau(t, j))\bar{x}(t, j) = (I + A\tau(t, j))\bar{x}(t_j, j). \tag{7.13}$$

Then we may write an autonomous version of the dynamics of $\bar{x}$ and of a sampled version $\bar{y}$ of output $y = Cx$, by replacing the update of $\bar{x}$ in (7.11c) by

$$\bar{x}^+ = (I + AT)\bar{x}, \quad \bar{y} := C\bar{x}^+ = C(I + AT)\bar{x}, \tag{7.14}$$

where we emphasize that output y at sampling times depends on the current continuous state x, which is the future sample $\bar{x}^+$ of the sampled state $\bar{x}$. Inspired by (7.14) we propose the following sampled-data approximation of the jumps of $\bar{\hat{x}}$ in (7.11c)

$$\begin{aligned} \bar{\hat{x}}^+ &= h_1\Big(\bar{h}_2\big((I + AT)\bar{\hat{x}} + TL\varphi(\bar{y} - \bar{\hat{y}}), \bar{y}\big)\Big) \\ \bar{\hat{y}} &:= C(I + AT)\bar{\hat{x}}, \end{aligned} \tag{7.15}$$

which enjoys the property in the next theorem.

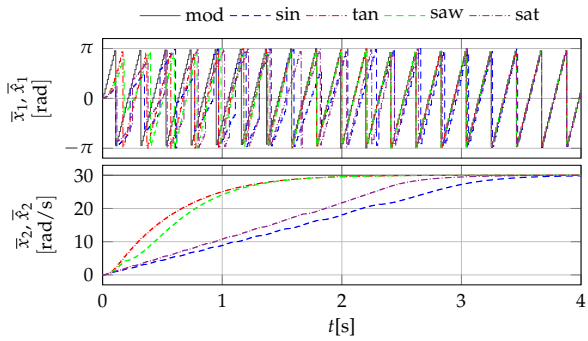

Figure 7.6: Sampled-data simulation using the four injection functions. $\epsilon = 0.7$.

Theorem 7.2. *For any Lipschitz function φ satisfying Assumption 7.1 and some bounded set of initial conditions $\bar{\xi}(0,0)$, the sampled-data observer (7.15), (7.14) guarantees practical estimation of the sampled version $\bar{x}$ of state x with respect to parameter T.*

Proof. *The UGAS of (7.12) established in Proposition 7.1 is semiglobally practically robust in the sense of [45, Lemma 7.20]. We may then consider a perturbed version of dynamics (7.11) where the upper equation in (7.11a) is replaced by*

$$(\dot{x}, \dot{\hat{x}}) = \left[\begin{smallmatrix} A & 0 \\ 0 & A \end{smallmatrix}\right](x, \hat{x}) + \left[\begin{smallmatrix} 0 \\ L \end{smallmatrix}\right] \varphi(C(I + AT)(\bar{x} - \bar{\hat{x}})), \tag{7.16}$$

which we denote by ((7.11)←(7.16)) for simplicity of notation. We may well interpret ((7.11)←(7.16))) as a perturbed version of (7.11) where the right hand side of (7.11a) is affected by disturbance

$$Ld := L(\varphi(C(I + AT)(\bar{x} - \bar{\hat{x}})) - \varphi(C(x - \hat{x}))). \tag{7.17}$$

For the ensuing system, intersecting the flow and jump sets with any arbitrarily large set $\{\hat{x}_2 \in [-\hat{x}_{2M}, \hat{x}_{2M}]\}$, we obtain the uniform bound (where L_φ represents a Lipschitz bound and φ_M represents a global bound for $\varphi(\cdot)$):

$$\begin{aligned} |d| &\leq |\varphi(C(I + AT)(\bar{x} - \bar{\hat{x}})) - \varphi(C(\bar{x} - \bar{\hat{x}}))| \\ &\quad + |\varphi(C(\bar{x} - \bar{\hat{x}})) - \varphi(C(x - \hat{x}))| \\ &\leq L_\varphi(T(x_{2M} + \hat{x}_{2M}) + T|x_1 - \bar{x}_1| + T|\hat{x}_1 - \bar{\hat{x}}_1|), \end{aligned}$$

which shrinks to zero as T is reduced because $|\dot{\hat{x}}_1| \leq \hat{x}_{2M} + \ell_1 \varphi_M$ and $|\dot{x}_1| \leq x_2$, which belongs to compact set $\mathcal{K}_2$. The possibility of shrinking d to zero by reducing T enables applying [45, Lemma 7.20] and establishing semiglobal practical UGAS of $\mathcal{A}^{\bar{\xi}}$ in (7.12).

The proof is then completed by noticing that the term $\varphi(C(I + AT)(\bar{x} - \bar{\hat{x}}))$ forcing the right hand side of (7.16) is constant and equal to $\varphi(\bar{y} - \bar{\hat{y}})$. Therefore the value of $\bar{\hat{x}}^+$ in (7.15) coincides with that of $\bar{\hat{x}}^+$ in (7.11c). Practical convergence of $\bar{\hat{x}}$ to $\bar{x}$ then follows from practical UGAS of $\mathcal{A}^{\bar{\xi}}$ in (7.12) and the fact that $\bar{\hat{x}} = \bar{x}$ in $\mathcal{A}^{\bar{\xi}}$. □

In Figure 7.6, we illustrate a 100 Hz sampled-data simulation of the proposed law, showing similar behavior to the continuous-time counterpart.

7.5.3 Real-time implementation and experiments

Algorithme 1 : Real-time implementation of (7.15).

Input : $\overline{y}$ ▷ sampled angle measurement

Parameters : ℓ_1, ℓ_2, δ_π, T

while true **do**
  $\overline{y} = y$ ▷ update the angular measurement
  $\bar{\hat{x}} \leftarrow (I + AT)\bar{\hat{x}} + TL\varphi(\overline{y} - (\bar{\hat{x}}_1 + T\bar{\hat{x}}_2))$ ▷ (7.15) to $\bar{\hat{x}}$
  if $||\overline{y} - \bar{\hat{x}}_1| - \pi| \leq \delta_\pi$ **then** ▷ check if $\overline{y} - \bar{\hat{x}}_1 \in \mathcal{J}_2$
    $\bar{\hat{x}}_1 \leftarrow \overline{y}$ ▷ apply jump map $\bar{h}_2(\bar{\hat{x}}, \overline{y})$
  end
  if $|\bar{\hat{x}}_1| \geq \pi + \delta_\pi$ **then** ▷ check if $\bar{\hat{x}} \in \mathcal{J}_1$
    $\bar{\hat{x}}_1 \leftarrow \bar{\hat{x}}_1 - 2\pi \text{sign}\,(\bar{\hat{x}}_1)$ ▷ apply jump map $\bar{h}_1(\bar{\hat{x}})$
  end
end

A ready-to-code algorithm implementing the sampled-data observer (7.15) can be found in Algorithm 1. Four realizations of Algorithm 1 have been coded in C++ in a 32 bit 120 MHz ARM Cortex-M4 microprocessor. Each one of the four realization represents one of the case studies of output injection function φ presented in Section 7.4. The microprocessor reads out the angular measurements via an I2C bus from an Hall-effect AMS AS5048 encoder, which is an easy-to-use 14 bit resolution absolute angular sensor for industrial applications. In our experiments the encoder measures the angular displacement of the shaft of a small DC brushed motor that is open-loop voltage controlled. The algorithms run in real time at 100 Hz and the observer parameters k_p and k_v are set as in the simulations to respectively 5 and 6, while $\delta_\pi = 0.0873$ rad, and $M = 1$. The results of one of the experiments are depicted in Figure 7.7. In the plots relative to the angular velocity estimation we added in light gray a dirty derivative of a rectified version of the sampled measurement $\overline{y}$, which was computed off-line. The DC motor is supplied with a voltage inducing a rotation with approximate speed of 150 $\frac{\text{rad}}{\text{s}}$. In the acceleration phase the motor reaches the steady state in about 2s, and the high-gain scaling factor ϵ is such that all the case studies behave similarly, confirming the simulation results. Similar behaviors are produced at the steady state as well, where the dirty derivative curve confirms that the angular velocity estimated by the real-time observer implementation is correct and well filtered. In the deceleration phase the motor slows down more promptly, making the differences among the four considered case studies more evident. The experimental results confirm that the increased aggressiveness of the "tan" and "saw" output injection functions produce a faster transient, while the limited forcing actions of the "sin" and "sat" selections produce a slower transient.

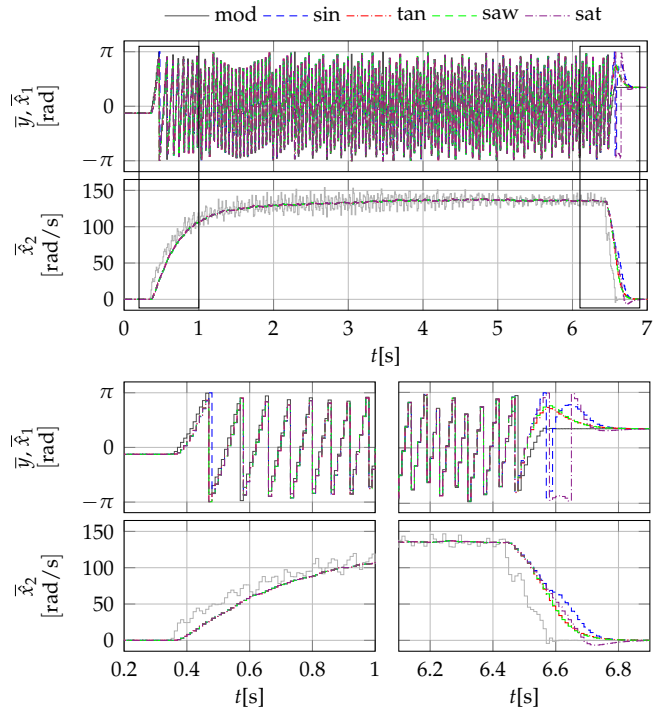

Figure 7.7: Experimental results using the four injection functions. $\epsilon = 0.1$.

8 CONCLUSIONS AND FUTURE PERSPECTIVES

In this manuscript, we faced different problems of technological interest in aerospace, for which we proposed innovative solutions that take advantage of hybrid dynamical systems and, in particular, of the comprehensive hybrid dynamical system framework [45]. For the proposed algorithms, we gave formal stability certificates proving desirable properties thanks to the tools made available in [45] and some recent extensions.

In particular, each part of the thesis leads to its own conclusion and future perspectives.

PART I In this part of the thesis, a new model of the relative dynamics between two spacecrafts in elliptic orbit is developed based on Floquet-Lyapunov theory in order to obtain a linear time-invariant free motion representation of the rendezvous problem. This problem is then recast as a stabilization problem for a periodic trajectory in a hybrid dynamical systems framework. Two new control laws have been proposed and compared to a control scheme given in [33], which is re-interpreted in this hybrid context. The new controllers take advantage from steering the satellite motion along periodic (therefore bounded) transient relative orbits. The use of the hybrid formalism has allowed us to prove asymptotic stability of the desired motion, in addition to robustness to perturbations. Such a robustness is confirmed by suitable simulation results showing desirable responses also in the presence of unmodeled nonlinear phenomena and external disturbances affecting the satellite motion.

Future perspective may lead to synthesizing hybrid impulsive control strategy making use of the framework developed here but taking into account saturation limits of the thrusters and minimization the fuel consumption.

PART II In this part, we proposed a robust hybrid time-sub-optimal controller for a class of linear SISO plants with saturated input with up to three poles at the origin. Input saturation can be both a technological limit of the actuators, or an artificial constraint introduced for safety reasons. First, an analysis of the switching sets for the time-optimal control of the considered dynamics has been carried out by means of suitable switching functions. Based on this description, an implicit hybrid framework for robust time-sub-optimal control has been introduced. A hybrid blend with a local linear feedback has been then developed, which ensures global asymptotic stability of the origin. Then, its effectiveness has been illustrated both in a simulated and real implementation scenario. In particular, the benchmark model of Quanser's 3 DOF Helicopter developed in Chap-

ter 5 has been used as a simulative tool, while a propeller-actuated arm experiment served as a real experimental benchmark. Both these validation tools have shown the effectiveness of the proposed scheme, in the presence of unmodelled dynamics, measurement noise and limited performance hardware. In particular, the hysteresis mechanism in the global controller and in the uniting global and local strategy has been shown to prevent chattering effects, producing clean and desirable evolutions.

Future interesting research directions may consider the extension of the scheme to reject constant disturbances, and further illustrating the technological advantages of the proposed stabilizers.

PART III In this last part, we proposed a nonlinear hybrid speed observer structure for angular measurements evolving on S_1 and affected by jumps. Stability properties of the proposed observer have been established with a Lyapunov-based argument under some natural assumptions on the nonlinear injection function representing the external innovation forcing action. After showing some continuous-time simulations, a sampled-data approximated version of the proposed observer was developed for real time implementation. Experimental results of the discretized observer have been reported, showing that the proposed algorithm is suitable for mechatronic applications. Indeed, this algorithm has been successfully exploited with real-time implementations in order to estimate the propeller rotational velocities of the experimental setup used to validate the RTSO controller of Chapter 4, as discussed in Chapter 6.

Future advancements may be in the direction of studying the input-to-state stability properties of the proposed scheme. Motivated by the approach in [3], further investigations may be towards embedding an adaption mechanism of the saturation level when using a saturation function in the output injection, in order to bring together both the advantage of having a limited control effort when the estimation error is small, and the fast convergence of the saw function when the estimation error is large.

Broadly speaking, this manuscript confirmed the effectiveness of the recent trend of exploiting hybrid dynamics for designing innovative estimation and control algorithm with enhanced performance. Moreover, in the wake of the technological experience carried out while performing the activities illustrated in this manuscript, the author believes that the hybrid dynamical systems framework could bring benefit to many industrial applications as well, especially in situations where complex dynamical behaviors are needed. Nevertheless, the author feels that there is still lack of a hybrid counterpart of some useful classical analysis tools. For example, an extension to the hybrid context of the linear approximation method for studying stability properties of equilibria of non-linear systems would be useful, as much as the possibility of studying the stability of the interconnection between many different hybrid systems, through input-output properties, without the need of writing a single hybrid system.

BIBLIOGRAPHY

[1] H.J. Ahn and D.M. Lee. "A new bumpless rotor-flux position estimation scheme for vector-controlled washing machine." In: *IEEE Transactions on Industrial Informatics* 12.2 (2016), pp. 466–473.

[2] A. Ailon and R. Ortega. "An observer-based set-point controller for robot manipulators with flexible joints." In: *Systems & Control Letters* 21.4 (1993), pp. 329–335.

[3] A. Alessandri and L. Zaccarian. "Stubborn state observers for linear time-invariant systems." In: *Automatica* 88 (2018), pp. 1–9.

[4] K.T. Alfriend and H. Schaub. "Dynamics and control of spacecraft formations: Challenges and some solutions." In: *Journal of the Astronautical Sciences* 48.2 (2000), pp. 249–267.

[5] K.T. Alfriend, S.R. Vadali, P. Gurfil, J.P. How, and L.S. Breger. *Spacecraft Formation Flying*. Burlington, MA, USA: Elsevier, 2010.

[6] N. Anandan and B. George. "A wide-range capacitive sensor for linear and angular displacement measurement." In: *IEEE Transactions on Industrial Electronics* 64.7 (2017), pp. 5728–5737.

[7] V. Andrieu and L. Praly. "On the Existence of a Kazantzis–Kravaris/Luenberger Observer." In: *SIAM Journal on Control and Optimization* 45.2 (2006), pp. 432–456.

[8] V. Andrieu, C. Prieur, S. Tarbouriech, and L. Zaccarian. "A hybrid scheme for reducing peaking in high-gain observers for a class of nonlinear systems." In: *Automatica* 72 (2016), pp. 138–146.

[9] P.R. Arantes Gilz, M.M. Joldes, C. Louembet, and F. Camps. "Model predictive control for rendezvous hovering phases based on a novel description of constrained trajectories." In: *IFAC-PapersOnLine* 50.1 (2017). 20th IFAC World Congress. ISSN: 2405-8963.

[10] M. Athans and P.L. Falb. *Optimal control. An introduction to the theory and its applications*. McGraw-Hill Book Co., New York-Toronto, Ont.-London, 1966, pp. xiv+879.

[11] D. Barden and C. Thomas. *An introduction to differential manifolds*. Imperial College Press, 2003.

[12] A. Ben-Israel and T. NE Greville. *Generalized inverses: theory and applications*. Vol. 15. Springer Science & Business Media, 2003.

[13] S. Berkane, A. Abdessameud, and A. Tayebi. "Global hybrid attitude estimation on the Special Orthogonal group SO(3)." In: *American Control Conference (ACC)*. 2016, pp. 113–118.

[14] S. Berkane and A. Tayebi. "Construction of Synergistic Potential Functions on SO(3) With Application to Velocity-Free Hybrid Attitude Stabilization." In: *IEEE Transactions on Automatic Control* 62.1 (2017), pp. 495–501.

[15] S.P. Bhat and D.S. Bernstein. "A topological obstruction to continuous global stabilization of rotational motion and the unwinding phenomenon." In: *Systems & Control Letters* 39.1 (2000), pp. 63–70.

[16] S.P. Bhat and D.S. Bernstein. "Finite-time stability of continuous autonomous systems." In: *SIAM Journal on Control and Optimization* 38.3 (2000), pp. 751–766.

[17] A. Bisoffi, L. Zaccarian, M. Da Lio, D. Carnevale, and JET Contributors. "Hybrid cancellation of ripple disturbances arising in AC/DC converters." In: *Automatica* 77 (2017), pp. 344–352.

[18] S. Bittanti and P. Colaneri. *Periodic Systems: Filtering and Control*. Communications and Control Engineering. Springer, 2008. ISBN: 9781848009103.

[19] P. Bodin, R. Larsson, F. Nilsson, C. Chasset, R. Noteborn, and M. Nylund. "PRISMA: an in-orbit test bed for guidance, navigation, and control experiments." In: *Journal of Spacecraft and Rockets* 46.3 (2009), pp. 615–623.

[20] M. Brentari, D. Arzelier, C. Louembet, L.S. Urbina, and L. Zaccarian. "A hybrid control framework for impulsive control of satellite rendezvous." In: *American Control Conference (ACC)*. Boston (MA), USA, 2016.

[21] M. Brentari, P. Bosetti, R. Goebel, and L. Zaccarian. "Robust time-sub-optimal control of the saturated double integrator applied to attitude stabilization." In: *IEEE Conference on Decision and Control (CDC)*. Melbourne (Australia), 2017, pp. 5487–5492.

[22] M. Brentari, P. Bosetti, I. Queinnec, and L. Zaccarian. "Benchmark model of Quanser's 3 DOF Helicopter." Under review in the IEEE/ASME Transactions on Mechatronics. 2018. URL: https://hal.laas.fr/hal-01711135.

[23] M. Brentari, P. Bosetti, and L. Zaccarian. "A class of hybrid velocity observers for angular measurements with jumps." In: *IEEE Control Systems Letters* 2.4 (2018), pp. 617–622.

[24] M. Brentari, S. Urbina, D. Arzelier, C. Louembet, and L. Zaccarian. "A hybrid control framework for impulsive control of satellite rendezvous." In: *IEEE Transactions on Control Systems Technology* 99 (2018), pp. 1–15.

[25] M. Brentari, A. Zambotti, L. Zaccarian, P. Bosetti, and F. Biral. "Position and speed control of a low-cost two-wheeled, self-balancing inverted pendulum vehicle." In: *IEEE International Conference on Mechatronics (ICM)*. IEEE. 2015, pp. 347–352.

[26] P.J. Bristeau, P. Martin, E. Salaün, and N. Petit. "The role of propeller aerodynamics in the model of a quadrotor UAV." In: *European Control Conference (ECC)*. 2009, pp. 683–688.

[27] H. Castañeda, F. Plestan, A. Chriette, and J. de León-Morales. "Continuous Differentiator Based on Adaptive Second-Order Sliding-Mode Control for a 3-DOF Helicopter." In: *IEEE Transactions on Industrial Electronics* 63.9 (2016), pp. 5786–5793. ISSN: 0278-0046.

[28] Y. Chitour. "Time-varying high-gain observers for numerical differentiation." In: *IEEE Transactions on Automatic Control* 47.9 (2002), pp. 1565–1569.

[29] A. Chriette, F. Plestan, H. Castañeda, M. Pal, M. Guillo, M. Odelga, S. Rajappa, and R. Chandra. "Adaptive robust attitude control for UAVs–Design and experimental validation." In: *International Journal of Adaptive Control and Signal Processing* 30.8-10 (2016), pp. 1478–1493.

[30] F.H. Clarke. *Optimization and nonsmooth analysis*. Vol. 5. Siam, 1990.

[31] P. Coote, J. Trumpf, R. Mahony, and J.C. Willems. "Near-optimal deterministic filtering on the unit circle." In: *IEEE Conference on Decision and Control (CDC)*. 2009, pp. 5490–5495.

[32] N. Cox, L. Marconi, and A.R. Teel. "High-gain observers and linear output regulation for hybrid exosystems." In: *International Journal of Robust and Nonlinear Control* 24.6 (2014), pp. 1043–1063.

[33] G. Deaconu, C. Louembet, and A. Theron. "A two-impulse method for stabilizing the spacecraft relative motion with respect to a periodic trajectory." In: *IEEE Conference on Decision and Control (CDC)*. 2012.

[34] G. Deaconu, C. Louembet, and A. Theron. "Constrained periodic spacecraft relative motion using non-negative polynomials." In: *American Control Conference (ACC)*. 2012.

[35] G. Deaconu, C. Louembet, and A. Théron. "Designing continuously constrained spacecraft relative trajectories for proximity operations." In: *Journal of Guidance, Control, and Dynamics* 38.7 (2015), pp. 1208–1217.

[36] D. Diaz, D. Fernandez, C. Gonzales, S.B. Lee, and F. Briz. "Permanent Magnet Synchronous Machine Drive Control Using Analog Hall-Effect Sensors." In: *IEEE Transactions on Industry Applications* (2018).

[37] F. Dinuzzo and A. Ferrara. "Higher order sliding mode controllers with optimal reaching." In: *IEEE Transactions on Automatic Control* 54.9 (2009), pp. 2126–2136.

[38] W. Fehse, ed. *Automated rendezvous and docking of spacecraft*. Cambridge Aerospace Series. Cambridge, UK: Cambridge University Press, 2003.

[39] S. Formentin and M. Lovera. "Flatness-based control of a quadrotor helicopter via feedforward linearization." In: *IEEE Conference on Decision and Control (CDC) and European Control Conference (ECC)*. 2011, pp. 6171–6176.

[40] F. Forni, S. Galeani, and L. Zaccarian. "A family of global stabilizers for quasi-optimal control of planar linear saturated systems." In: *IEEE Transactions Automatic Control* 55.5 (2010), pp. 1175–1180.

[41] A.L. Fradkov, B. Andrievsky, and D. Peaucelle. "Adaptive control design and experiments for LAAS "Helicopter" benchmark." In: *European Journal of Control* 14.4 (2008), pp. 329–339.

[42] A.T. Fuller. "In-the-large stability of relay and saturating control systems with linear controllers." In: *International Journal of Control* 10.4 (1969), pp. 457–480.

[43] W. Gao and Z.P. Jiang. "Data-driven adaptive optimal output-feedback control of a 2-DOF helicopter." In: *American Control Conference (ACC)*. 2016, pp. 2512–2517.

[44] R. Goebel, R.G. Sanfelice, and A.R. Teel. "Hybrid dynamical systems." In: *IEEE Control Systems* 29.2 (2009), pp. 28–93.

[45] R. Goebel, R.G. Sanfelice, and A.R. Teel. *Hybrid Dynamical Systems: modeling, stability, and robustness*. Princeton University Press, 2012.

[46] P. Gurfil. "Relative Motion between Elliptic Orbits: Generalized Boundedness Conditions and Optimal Formationkeeping." In: *Journal of Guidance, Control and Dynamics* 28.4 (2005), pp. 761–767.

[47] A. Hassibi, S.P. Boyd, and J.P. How. "A class of Lyapunov functionals for analyzing hybrid dynamical systems." In: *American Control Conference (ACC)*. 1999, pp. 2455–2460.

[48] M. F. Haydar and M. Lovera. "H_∞ filtering on the unit circle." In: *IEEE Conference on Decision and Control (CDC)*. 2017, pp. 2422–2427.

[49] M.D. Hua, T. Hamel, P. Morin, and C. Samson. "Introduction to feedback control of underactuated VTOLvehicles: A review of basic control design ideas and principles." In: *IEEE Control Systems* 33.1 (2013), pp. 61–75.

[50] G. Inalhan, M. Tillerson, and J.P. How. "Relative dynamics and control of spacecraft formations in eccentric orbits." In: *Journal of Guidance, Control and Dynamics* 25.1 (2002), pp. 48–59.

[51] M. Ishitobi, M. Nishi, and K. Nakasaki. "Nonlinear adaptive model following control for a 3-DOF tandem-rotor model helicopter." In: *Control Engineering Practice* 18.8 (2010), pp. 936–943.

[52] A. Isidori, L. Marconi, and A. Serrani. "Robust nonlinear motion control of a helicopter." In: *IEEE Transactions on Automatic Control* 48.3 (2003), pp. 413–426.

[53] C. Jewison and R.S. Erwin. "A spacecraft benchmark problem for hybrid control and estimation." In: *IEEE Conference on Decision and Control (CDC)*. Las Vegas, Nevada, USA, 2012.

[54] H.K. Khalil. *Nonlinear Systems*. 2001, p. 767. ISBN: 0130673897.

[55] H.K. Khalil and L. Praly. "High-gain observers in nonlinear feedback control." In: *International Journal of Robust and Nonlinear Control* 24.6 (2014), pp. 993–1015.

[56] T. Kiefer, K. Graichen, and A. Kugi. "Trajectory tracking of a 3DOF laboratory helicopter under input and state constraints." In: *IEEE Transactions on Control Systems Technology* 18.4 (2010), pp. 944–952.

[57] H.S. Kim, S. Lim, C.C. Iuraşcu, F.C. Park, and Y.M. Cho. "A robust, discrete, near time-optimal controller for hard disk drives." In: *Precision engineering* 28.4 (2004), pp. 459–468.

[58] D.E. Kirk. *Optimal control theory: an introduction*. Courier Corporation, 2012.

[59] A.T. Kutay, A.J. Calise, M. Idan, and N. Hovakimyan. "Experimental results on adaptive output feedback control using a laboratory model helicopter." In: *IEEE Transactions on Control Systems Technology* 13.2 (2005), pp. 196–202.

[60] D.F. Lawden. *Optimal trajectories for space navigation*. London, England: Butterworth, 1963.

[61] S. Le Gac, D. Peaucelle, and B. Andrievsky. "Adaptive Parameter Identification for Simplified 3D-Motion Model of 'LAAS Helicopter Benchmark'." In: *IFAC Proceedings Volumes* 40.13 (2007), pp. 244–249.

[62] T. Lee. "Optimal hybrid controls for global exponential tracking on the two-sphere." In: *IEEE Conference on Decision and Control (CDC)*. 2016, pp. 3331–3337.

[63] Z. Li, H.H.T. Liu, B. Zhu, and H. Gao. "Robust Second-Order Consensus Tracking of Multiple 3-DOF Laboratory Helicopters via Output Feedback." In: *IEEE/ASME Transactions on Mechatronics* 20.5 (2015), pp. 2538–2549. ISSN: 1083-4435.

[64] H. Liu, J. Xi, and Y. Zhong. "Robust hierarchical control of a laboratory helicopter." In: *Journal of The Franklin Institute* 351.1 (2014), pp. 259–276.

[65] S.J.L.M. van Loon, B.G.B. Hunnekens, W.P.M.H. Heemels, N. van de Wouw, and H. Nijmeijer. "Split-path nonlinear integral control for transient performance improvement." In: *Automatica* 66 (2016), pp. 262–270.

[66] C. Louembet, D. Arzelier, and G. Deaconu. "Robust Rendezvous Planning Under Maneuver Execution Errors." In: *Journal of Guidance, Control, and Dynamics* (2015).

[67] B. Luo, H. N. Wu, and T. Huang. "Optimal Output Regulation for Model-Free Quanser Helicopter With Multistep Q-Learning." In: *IEEE Transactions on Industrial Electronics* 65.6 (2018), pp. 4953–4961. ISSN: 0278-0046.

[68] R. Mahony, T. Hamel, and J.M. Pflimlin. "Nonlinear complementary filters on the special orthogonal group." In: *IEEE Transactions on Automatic Control* 53.5 (2008), pp. 1203–1218.

[69] B.P. Malladi, R.G. Sanfelice, E. Butcher, and J. Wang. "Robust hybrid supervisory control for rendezvous and docking of a spacecraft." In: *IEEE Conference on Decision and Control (CDC)*. Las Vegas, Nevada, USA, 2012.

[70] L. Masisi and P. Pillay. "High-resolution low-cost rotor position sensor for traction applications." In: *IEEE IECON*. 2017, pp. 1971–1976.

[71] C.G. Mayhew, R.G. Sanfelice, and A.R. Teel. "Quaternion-based hybrid control for robust global attitude tracking." In: *IEEE Transactions on Automatic control* 56.11 (2011), pp. 2555–2566.

[72] R. Naldi, M. Furci, R.G. Sanfelice, and L. Marconi. "Global trajectory tracking for underactuated VTOL aerial vehicles using a cascade control paradigm." In: *IEEE Conference on Decision and Control (CDC)*. 2013, pp. 4212–4217.

[73] R. Naldi, M. Furci, R.G. Sanfelice, and L. Marconi. "Robust global trajectory tracking for underactuated VTOL aerial vehicles using inner-outer loop control paradigms." In: *IEEE Transactions on Automatic Control* 62.1 (2017), pp. 97–112.

[74] D. Nešić, L. Zaccarian, and A.R. Teel. "Stability properties of reset systems." In: *Automatica* 44.8 (2008), pp. 2019–2026.

[75] W.S. Newman. "Robust near time-optimal control." In: *IEEE Transactions Automatic Control* 35.7 (1990), pp. 841–844.

[76] S. Nicosia, A. Tornambè, and P. Valigi. "Experimental results in state estimation of industrial robots." In: *IEEE Conference on Decision and Control (CDC)*. 1990, pp. 360–365.

[77] L. Y. Pao and G. F. Franklin. "Proximate time-optimal control of third-order servomechanisms." In: *IEEE Transactions Automatic Control* 38.4 (1993), pp. 560–580. ISSN: 0018-9286.

[78] L.Y. Pao and G.F. Franklin. "The robustness of a proximate time-optional controller." In: *IEEE Transactions Automatic Control* 39.9 (1994), pp. 1963–1966. ISSN: 0018-9286.

[79] D.U. Patil and D. Chakraborty. "Computation of time optimal feedback control using Groebner basis." In: *IEEE Transactions Automatic Control* 59.8 (2014), pp. 2271–2276. ISSN: 0018-9286.

[80] D. Peaucelle, B. Andrievsky, V. Mahout, and A. Fradkov. "Robust simple adaptive control with relaxed passivity and PID control of a helicopter benchmark." In: *IFAC Proceedings Volumes* 44.1 (2011), pp. 2315–2320.

[81] J.M. Pflimlin, P. Soueres, and T. Hamel. "Hovering flight stabilization in wind gusts for ducted fan UAV." In: *IEEE Conference on Decision and Control (CDC)*. Vol. 4. Atlantis (BA), USA, 2004, pp. 3491–3496.

[82] C. Prieur and A.R. Teel. "Uniting local and global output feedback controllers." In: *IEEE Transactions Automatic Control* 56.7 (2011), pp. 1636–1649. ISSN: 0018-9286.

[83] Quanser. *3DOF Helicopter Manual*. URL: http://www.lehigh.edu/~inconsy/lab/frames/experiments/QUANSER-3DOFHelicopter_Reference_Manual.pdf.

[84] Quanser. *Quanser website*. https://www.quanser.com/.

[85] S. Rajappa, A. Chriette, R. Chandra, and W. Khalil. "Modelling and dynamic identification of 3 DOF Quanser helicopter." In: *International Conference on Advanced Robotics (ICAR)*. 2013, pp. 1–6.

[86] V. G Rao and D.S. Bernstein. "Naive control of the double integrator." In: *IEEE Control Systems* 21.5 (2001), pp. 86–97.

[87] Venkatesh G. Rao and Dennis S. Bernstein. "Setpoint tracking with actuator offset and sensor bias: probing the limits of integral control." In: *IEEE Control Syst. Mag.* 21.5 (2001), pp. 86–97. ISSN: 1066-033X.

[88] H. Ríos, A. Rosales, A. Ferreira, and A. Dávilay. "Robust regulation for a 3-DOF helicopter via sliding-modes control and observation techniques." In: *American Control Conference (ACC)*. Baltimore (MD), USA, 2010, pp. 4427–4432.

[89] I.M. Ross. "6 Space trajectory optimization and L 1-optimal control problems." In: *Elsevier Astrodynamics Series* 1 (2007), pp. 155–VIII.

[90] E.P. Ryan. "Time-optimal feedback control laws for certain third-order relay control systems." In: *International Journal of Control* 20.6 (1974), pp. 881–911.

[91] A. Sarlette, S.E. Tuna, V.D. Blondel, and R. Sepulchre. "Global synchronization on the circle." In: *IFAC Proceedings Volumes* 41.2 (2008), pp. 9045–9050.

[92] H. Schaub. "Relative orbit geometry through classical orbit element differences." In: *Journal of Guidance, Control, and Dynamics* (2004).

[93] P. Sengupta and S.R. Vadali. "Relative motion and the geometry of formations in keplerian elliptic orbits." In: *Journal of Guidance, Control, and Dynamics* (2007).

[94] A. Seuret, C. Prieur, S. Tarbouriech, A. R. Teel, and L. Zaccarian. "A nonsmooth hybrid invariance principle applied to robust event-triggered design." In: *IEEE Transactions on Automatic Control* (2018), pp. 1–1. ISSN: 0018-9286.

[95] R.E. Sherill, A.J. Sinclair, T.A. Lovell, and S.C. Sinha. "Lyapunov-Floquet Transformation of satellite relative motion in elliptic orbits." In: *Celestial Mechanics and Dynamical Astronomy* 119 (2014), pp. 55–73.

[96] B Siciliano, L. Sciavicco, L. Villani, and G. Oriolo. "Robotics: modelling, planning and control, ser. Advanced Textbooks in Control and Signal Processing." In: *Springer* 26 (2009), p. 29.

[97] P. Stewart and V. Kadirkamanathan. "Commutation of permanent-magnet synchronous AC motors for military and traction applications." In: *IEEE Transactions on Industrial Electronics* 50.3 (2003), pp. 629–630.

[98] T. Strizic, J. I. Poveda, and A.R. Teel. "Hybrid gradient descent for robust global optimization on the circle." In: *IEEE Conference on Decision and Control (CDC)*. 2017, pp. 2985–2990.

[99] A.R. Teel. "Global stabilization and restricted tracking for multiple integrators with bounded controls." In: *Systems & control Lett.* 18.3 (1992), pp. 165–171.

[100] F. Tibor and G. Brasseur. "A robust capacitive angular speed sensor." In: *IEEE Transactions on Instrumentation and Measurement* 47.1 (1998), pp. 280–284.

[101] J. Tschauner. "The elliptic orbit rendezvous." In: *AIAA 4th Aerospace Sciences Meeting*. Los Angeles, Californie, USA, 1966.

[102] U. Walther, T.T. Georgiou, and A. Tannenbaum. "On the computation of switching surfaces in optimal control: a Gröbner basis approach." In: *IEEE Transactions Automatic Control* 46.4 (2001), pp. 534–540. ISSN: 0018-9286.

[103] J. Witt, S. Boonto, and H. Werner. "Approximate model predictive control of a 3-DOF helicopter." In: *IEEE Conference on Decision and Control (CDC)*. 2007, pp. 4501–4506.

[104] K. Yamanaka and F. Ankersen. "New State Transition Matrix for Relative Motion on an Arbitrary Elliptical Orbit." In: *Journal of Guidance, Control, and Dynamics* 25.1 (2002), pp. 60–66. ISSN: 0731-5090.

[105] M. Zamani, J. Trumpf, and R. Mahony. "Minimum-energy filtering on the unit circle." In: *Australian Control Conf.* 2011, pp. 236–241.

[106] B. Zheng and Y. Zhong. "Robust attitude regulation of a 3-DOF helicopter benchmark: theory and experiments." In: *IEEE Transactions on Industrial Electronics* 58.2 (2011), pp. 660–670.